A STUDY INTO THE ROLES OF CU/TIO2 PHOTOCATALYSTS IN THE OF METHYLENE BLUE PHOTODECOMPOSITION AND WATER PHOTO-SPLITTING

CHONG SOO KEE

Thesis submitted in partial fulfilment of the requirements
for the award of the degree of
Bachelor of Chemical Engineering

Faculty of Chemical & Natural Resources Engineering
UNIVERSITI MALAYSIA PAHANG

JANUARY 2014

ABSTRACT

Several papers have addressed the production of H_2 from water using catalyst. One of the most innovative ways is via photocatalysis. In this study, titania act as the base catalyst on which copper dopant varies the physicochemical properties. Ultimately, this work was aimed to synthesized and investigated the physicochemical properties of titania supported copper, (Cu/TiO_2) photocatalyst for photoreaction of glycerol solution. The photocatalyst, Cu/TiO_2 was prepared via wet impregnation method with doped 2, 5, 10, 15, 20 and 25 wt% of Cu. X-ray fluorescence (XRF) showed that the composition of Cu followed the doped weight percentage on TiO_2 and liquid-nitrogen physisorption showed that the BET specific surface area decreased with the increment of Cu loading. Thermogravimetric analysis (TGA) showed that Cu decomposed around 450 to 550 K while X-ray diffraction (XRD) proved the Cu/TiO_2 was anatase with a new peak 2θ = 13° found as the appearance peak of CuO species. The measured densities were differed from the theoretical calculated densities. The photoreactivity of Cu/TiO_2 was tested with methylene blue decomposition and the results have indicated that Cu/TiO2 possessed photoreactivity. The conversions for all the photocatalysts with Cu loading were higher than the pristine TiO_2. This has confirmed that Cu loading has effectively increased the photoreaction of methylene blue solution. The 15 wt% Cu/TiO_2 photocatalyst showed the highest conversion at 44%. For loadings lower than 15wt%Cu, the photocatalytic activity increased with Cu deposition on TiO_2. The concentration profiles were fitted to the first order reaction rate law, the rate constant for each Cu/TiO_2 was calculated and 15 wt% Cu/TiO_2 has the highest rate constant (9.70×10^{-3} min^{-1}). The photocatalyst loading and concentration loading were conducted. In photocatalyst loading study, 1.0 g/L of 15 wt% Cu/TiO_2 can be concluded as the optimum weight loading for 300 mL of MB solution. In the concentration study, the amount of photocatalyst (0.25g) considered not optimum to yield the maximum conversion. The photocatalytic performance of Cu/TiO_2 photocatalyst in various copper loadings has revealed that hydrogen generation activity was disadvantageous of high copper loading as it displayed an inferior activity.

ABSTRAK

Beberapa jurnal teleah mengemukakan tentang penghasilan H_2 dari air dengan mengguna pemangkin, salah satu cara yang inovatif ialah menggunakan photo-pemangkin. Dalam kajian ini, titania (Ti) menjadi sebagai tapak pemangkin dan copper (Cu) sebagai pendopan. Kajian ini bertujuan menghasil dan mentakrifkan sifat-sifat copper-titania (Cu/TiO_2) untuk photoreaksi larutan gliserin. Cu/TiO_2 dihasilkan dengan cara menperdopankan 2, 5, 10, 15, 20 dan 25 wt% Cu atas Ti. X-ray fluorescence (XRF) menunjukkan komposisi Cu mengikut peratusan pendopan atas Ti. Di samping itu, BET specific surface area menunjuk pengurangan dengan penambahan Cu. Thermogravimetric analysis (TGA) menunjukkan Cu mengurai dekat 450 hingga 550 K. X-ray diffraction (XRD) membuktikan Cu/TiO_2 ialah anatase, puncak 2θ = 13° ditemui dan puncak ini dipercayai sebagai kemunculan spesies CuO. Kepadatan Cu/TiO_2 mengukur dengan gas pycnometer menunjukkan perbezaan dengan kepadatan teori. Photoreaksi Cu/TiO_2 dicubakan dengan mengguna methylene blue, reaksi methylene blue membuktikan pemangkin kajian ini berfungsi. 15 wt% Cu/TiO_2 mempunyai reaksi yang paling tinggi dengan bacaan 44%. Untuk beban yang lebih rendah daripada 15wt% Cu, aktiviti meningkat dengan Cu penimbunan pada TiO_2.Kadar pemalar setiap pemangkin dikirakan, 2 wt% Cu/TiO_2 mempunyai kadar pemalar yang tertinggi, 9.70×10^{-3} min^{-1}. Kajian ini diteruskan dengan tambahan berat pemangkin dan kepekatan larutan metilena biru. Dalam kajian penambahan berat pemangkin, 1.0g/L 2 wt% Cu/TiO_2 mempunyai reaksi yang tertinggi. Dalam kajian penambahan kepekatan larutan metilena biru , 25ppm larutan gliserin mempunyai reaksi yang terbaik. Prestasi photocatalytic daripada Cu/TiO_2 fotomangkin dalam pelbagai bebanan tembaga telah mendedahkan bahawa aktiviti penjanaan hidrogen adalah merugikan muatan tembaga yang tinggi kerana ia menunjukkan satu aktiviti rendah.

TABLE OF CONTENTS

LIST OF FIGURES

LIST OF TABLES

LIST OF NOMECLATURES

Notation	Description
a	BET effective cross-sectional area
C	BET dimensionless constant
C	Concentration
d	Inter plane distance of crystal
D	Crystalline size (Å)
e^-	Negative-electron
h^+	Positive-hole
k	Rate constant (min-1)
k_{Sch}	Scherrer constant
m	BET mass of solid catalyst
n	Order (interger)
N	Avogrado constant (6.022×10^{23} mol^{-1})
P	BET partial vapor pressure
P_a	BET ambient pressure
P_o	BET saturated pressure
ppm	part per million (mg/L)
r	BET correlation coefficient
R	BET gas constant (8.314 E7 ergs/K.mol)
$-r_A$	Photoreaction rate (mg/L.min)
r_k	BET Kelvin radius of pore
r_p	BET actual pore radius
S	BET specific surface area
T	BET ambient temperature
t	time
V_a	BET volume of gas adsorbed at STP
V_{ads}	BET volume of N2 adsorbed
V_{liq}	BET volume of liquid
V_m	BET volume of gas absorbed at STP to monolayer coverage
w	Weight fraction
wt%	Weight percent
X	Conversion
β_d	Angular width of half-maximum intensity (degree/°)
γ	BET surface tension of N2 (8.85 ergs.cm2 at 77.4 K)
θ	Angle (degree/°)
λ	Wavelength (nm)
ρ	Density

LIST OF ABBREVIATIONS

BET	Brunauer-Emmett-Teller
BJH	Barrett, Joyner and Halenda
BOD	Chemical oxygen demand
COD	Biochemical oxygen demand
DH	Dollimore and heal
ED	Energy-dispersive
MB	Methylene blue
STP	Standard temperature and pressure
TGA	Thermogravimetric analysis
UMP	Universiti Malaysia Pahang
UV	Ultraviolet
UV-Vis	Ultraviolet-visible spectrometer
WD	Wavelength-dispersive
XRD	X-ray diffraction
XRF	X-ray fluorescence

CHAPTER 1

INTRODUCTION

1. 1 Introduction

Recently, the issue of energy security has continuously hogged the limelight in lieu of scarcity of hydrocarbon reserves and stagnation in technology breakthrough (Yang et al., 2010). Furthermore, there is a consistent shift towards green energy policy in the face of growing environmental awareness among the literate society.

According to Liu et al. (2008), in order to mitigate this and promoting further the context of clean energy production via harnessing the abundantly available renewable resources, hydrogen generation from water photo-splitting clearly presents itself as one of the most viable technology. The significance of this area can be seen from the voluminous publications in particular pertaining to the selection of cheaper yet effective materials that are responsive towards water photosplitting. By breaking the hydrogen bond in water molecule, hydrogen (H_2) and oxygen gases could be simultaneously extracted from photocatalysis reaction.

In 1972, Fujishima and Honda demonstrated that overall water splitting can be achieved over pristine titanium dioxide (TiO_2) electrode under ultraviolet (UV) irradiation. Ever since, application of various metal oxide semi-conductors as candidate for water splitting photocatalysts has attracted much attention. During photoreaction, a pair of electrons and holes will be produced inside the photocatalyst matrix upon absorption of UV radiation either from sunlight or illuminated light source such as fluorescent lamps. When the electron in the valence band of TiO_2 becomes excited, it promotes the electron to the conduction band, creating the negative-electron (e-) and positive-hole (h+) pair. This stage is known as the

semiconductor's 'photo-excitation' state. The energy difference between the valence band and the conduction band is known as the 'Band Gap'.

Millions of various coloured chemical substances have been created within the last century or so, 10,000 of which are industrially produced (Zollinger., 1991). Over 0.7 million tons of organic synthetic dyes are manufactured each year mainly use in the textile, leather goods, industrial painting, food, plastics, cosmetics, and consumer electronic sectors. A sizable fraction of this is lost during the dying process and is released in the effluent water streams from the above industries. Hence, decolorization and detoxification of organic dye effluents have taken an increasingly important environmental significance in recent years (Brown et al., 1993 and Rajeshwar & Ibanez., 1997)

1. 2 Problem Statement

Photo-splitting of water to yield hydrogen can potentially address two greatest global issues, *viz*. global warming and nonrenewable fossil fuel consumption. Hydrogen is a clean energy carrier since the chemical energy stored is easily released when it combines with oxygen. Therefore, it yielded water as a by-product. The added advantages of hydrogen are the ease of transportation and storaged for extended time (Ho et al., 2011).

The presence of dyes in wastewaters has been recognized as one of the most important environmental hazardous substances, and the discharge of dyes in the waste waters is a matter of concern from both toxicological and esthetical reasons (Hu et al., 2011). Many new approaches have been investigated and chief among these, photocatalytic reaction has attracted great attention as emerging successful technology (Chen et al., 2007).

The potential of TiO_2 as a photocatalyst has been widely studied, as highlighted by Dholam et al. (2011). Significantly, the advantages of using TiO_2 as photocatalyst are numerous such as cheap and easily available, energy band edges which are well matched with the redox level of water, high resistance to corrosion and photo-corrosion in aqueous media as well as electronic properties that can be varied by just changing the lattice defects chemistry or the oxygen stoichiometry

In addition, the positive-hole of the TiO_2 breaks the water molecule, and forming hydrogen gas and hydroxyl radical. In a simultaneous reaction, the negative-electron reacts

with oxygen molecule to form oxide anion. This repeated reaction cycle is continued as long as the light is available.

1. 3 Objectives

Two main objectives are envisaged to be achieved from the current work:

i. To synthesize composite of photocatalyst from different metals loading
ii. To investigate the yield of hydrogen gas produced via water photo-splitting
iii. To investigate the photodecomposition of Methylene Blue via photocatalysts

1. 4 Scopes of Study

To achieve the outlined objectives, the following scopes will be covered for the entire duration of this study:

i. To synthesize Cu/TiO_2 photocatalyst using wet impregnation method with the dopant metal loading of :
    a. 2 wt%
    b. 5 wt%
    c. 10 wt%
    d. 15 wt%
    e. 20 wt%
    f. 25 wt%

ii. To characterize the physicochemical properties of Cu/TiO_2 photocatalyst using spectroscopic analyses such as:
    a) X-ray fluorescence (XRF)
    b) Liquid-nitrogen physisorption (Brunauer-Emmett-Teller, BET)
    c) X-ray diffraction (XRD)
    d) Thermogravimetric analysis (TGA)
    e) Gas pycnometer

iii. To study the effect of different loading of Cu/TiO_2 photocatalyst on the photo-splitting of water to yield hydrogen under UV-light and photodecomposition of methylene blue.

CHAPTER 2

LITERATURE REVIEW

2. 1 Photocatalytic of Water-Splitting

Titania (TiO_2) is a strong oxidizing agent that can lower the activation energy for both organic and inorganic compounds decomposition (Castellote & Bengtsson, 2011). Figure 2.1 illustrates the water-splitting process via a pair of TiO_2 n-type semiconductor photoelectrode (oxidizing regions) and platinum, Pt counter electrode (reducing regions) in a ground-breaking work by Fujishima and Honda back in 1972.

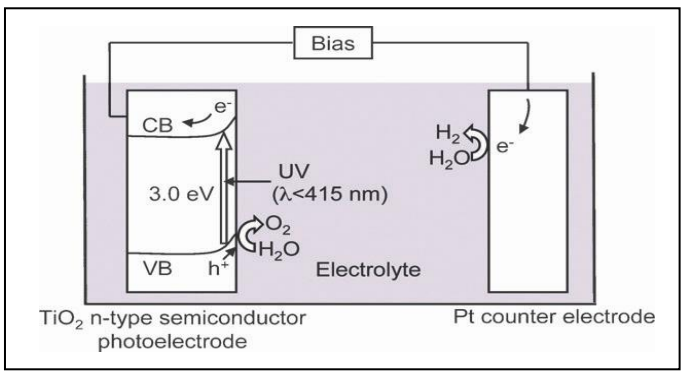

Figure 2-1 Honda-Fujishima effect water-splitting using a titanium dioxide (TiO_2) photo-electrode (Fujishima & Honda, 1972).

Similar to characteristic of other semiconductors, Titania possesses a conduction band independent of the valence band by a band gap with certain width. When the incident light

energy is larger than the band gap, electrons (e^-) and holes (h^+) are generated. The photo generated electrons and holes will induce redox reactions, i.e. water molecules are reduced by the electrons to form hydrogen (H_2) and oxidized by the holes to form oxygen (O_2) for the overall water splitting. The general chemical reactions are shown as (Fujishima & Honda, 1972):

Separation of carriers: $TiO_2 + h\nu \rightarrow h^+ + e^-$ (1)

Oxidation of water: $H_2O + h^+ \rightarrow \cdot OH + H^+$ (2)

Reduction of oxygen: $O_2 + e^- \rightarrow \cdot O^-_2$ (3)

Overall equation: $H_2O + h\nu \rightarrow H_2 + \frac{1}{2} O_2$ (4)

2.2 Photocatalysts for Aqueous Solution

In photocatalysis of water-splitting, the oxide photocatalyst consisting of d^0 metal cations, which can be classified into Groups 4, 5 and 6. Due to constrain such as light sources, reaction cells, and the difference of reaction scale, it will lead to the different in photocatalyst activities (Kudo & Miseki, 2008). The types of common oxide photocatalysts for water splitting under UV irradiation are summarized in Table 2.1 below.

On the other hand, the chemical reactions as shown in Equations (1) to (4) had shown that photocatalytic water-splitting is a promising technology in producing “clean” hydrogen (Liao et al., 2012). As can be seen in Table 2.1, TiO_2 is an ideal photocatalyst due to its stable, non-corrosive, environmentally friendly, abundant, and cost-effective characteristics compared to other photocatalysts.

Table 2-1 Oxide photocatalysts based on d0 metal ions for water splitting under UV irradiation (Kudo & Miseki, 2008)

Photocatalyst	Crystal Structure	BG/eV	Co-catalyst	Light Source	Reactant Solution	Activity/ μmol h^{-1}		QY (%)	Ref. (Year)
						H_2	O_2		
Ti Photocatalyst									
TiO_2	Anatase	3.2	Rh	Hg-Q	Water vapor	449		29	Yamaguti (1985)
$Rb_2La_2Ti_3O_{10}$	Layered Perovskite	3.4 – 3.5	NiO_x	Hg-Q	0.1M RbOH	869	430	5 (at 330nm)	Takata et al. (1997)
$La_2Ti_2O_7$	Layered Perovskite	3.8	NiO_x	Hg-Q	Pure Water	441		12 (< 360nm)	Kim et al. (2005)
$La_2Ti_2O_7$:Ba	Layered Perovskite		NiO_x	Hg-Q	Pure Water	5000		50	Kim et al. (2005)
$KaLaZr_{0.3}Ti_{0.7}O_4$	Layered Perovskite	3.91	NiO_x	Hg-Q	Pure Water	230	116	12.5	Reddy et al. (2003)
$La_4CaTi_5O_{17}$	Layered Perovskite	3.8	NiO_x	Hg-Q	Pure Water	499		20 (< 320nm)	Kim et al. (1999)
$Y_2Ti_2O_7$	Cubic Structure	3.5	NiO_x	Hg-Q	Pure Water	850	420	6 (at 313nm)	Abe et al. (2006)
Nb Photocatalysts									
$K_4Nb_6O_{17}$	Layered Structure	3.4	NiO_x	Hg-Q	Pure Water	1837	850	5 (at 330nm)	Domen et al. (1986)
$Rb_4Nb_6O_{17}$	Layered Structure	3.4	NiO_x	Hg-Q	Pure Water	936	451	10 (at 330nm)	Sayama et al. (1996)
$Ca_2Nb_2O_7$	Layered Perovskite	4.3	NiO_x	Hg-Q	Pure Water	101		7 (< 288nm)	Kim et al. (1999)
$Ba_5Nb_4O_{15}$	Layered Perovskite	3.85	NiO_x	Hg-Q	Pure Water	2366	1139	7 (at 270nm)	Miseki et al. (2006)
$Cs_2Nb_4O_{11}$	Pyrochlore Like	3.7	NiO_x	Hg-Q	Pure Water	1700	800	3 (at 270nm)	Miseki et al. (2005)
Ta Photocatalysts									
$K_3Ta_3Si_2O_{13}$	Tungsten Bronze	4.1	NiO	Hg-Q	Pure Water	2390	1210	6.5 (at 254nm)	Kurihara et al. (2006)
$LiTaO_3$	Ilumenite	4.7	None	Hg-Q	Pure Water	2180	1100	20 (at 270nm)	Kato & Kudo (2004)
$KTaO_3$:Zr	Perovskite	3.6	NiO_x	Xe-Q	Pure Water	19800	9700	56 (at 270nm)	Kato et al. (2003)
$SrTa_2O_6$	$CaTa_2O_6$ (orth.)	4.4	NiO	Hg-Q	Pure Water	960	490	7 (at 270nm)	Kato & Kudo (1996)
$Sr_2Ta_2O_7$	Layered Perovskite	4.6	NiO	Hg-Q	Pure Water	1000	480	12 (at 270nm)	Kudo et al. (2000)
$K_2Sr_{1.5}Ta_3O_{10}$	Layered Perovskite	4.1	RuO_2	Hg-Q	Pure Water	100	39.4	2 (at 252.5nm)	Yao & Ye (2007)
$KBa_2Ta_3O_{10}$	Layered Perovskite	3.5	NiO_x	Hg-Q	Pure Water	170		8 (< 350nm)	Kim et al. (1999)

2.3 Titanium Dioxide as Photocatalyst

Titanium is the world's fourth most abundant metal after aluminium, iron and magnesium; and the ninth most abundant element which constituting about 0.63% of the earth crust. It was discovered by Reverend William Gregor in 1791 in England. According to Carp et al. (2004), titanium metal is not found unbound to other elements but occurs primarily in minerals like rutile, ilmenite, leucoxene, anatase, brookite, perovskite, sphene and also found in titanates and many iron ores.

Titanium dioxide or titania (TiO_2) is the transition metal oxides. TiO_2 started replacing toxic lead oxides as pigments for white paint industrial since the beginning of the 20^{th} century and the annual production of TiO_2 exceeds 4 million tons (Greenwood et al., 1997; Natara et al., 1998). Overall, approximately 51% of TiO_2 production is used as a white pigment in paints, 19% in plastic, 17% in paper and others in minor sector.

2.3.1 Properties of Titanium Dioxide

As compared with other semiconductors (cf. Fig. 2.2), TiO_2 is considered as a good photocatalyst for hydrogen generation because of its stability. TiO_2 can only absorb photon near UV-range which 380 nm or less due to its large band gap of 3.2eV, and the e^- can only be excited in this UV-range (Tang et al., 2012).

According to Yoong et al. (2009), the use of UV radiation alone for photocatalytic reaction is not an economically option, it is a must to shift the edge of adsorption of Hence, many efforts have been made to extend the optical response of TiO_2 from UV-range to visible light range (400 – 750 nm). Unfortunately, there is limit in the research associated with visible light range. Melo and Silva (2011) have mentioned that many efforts have been commenced to extend the optical response of TiO_2 towards the visible region in order to fully harvest solar energy, since it accounts for approximately 43% of the incoming solar energy spectrum.

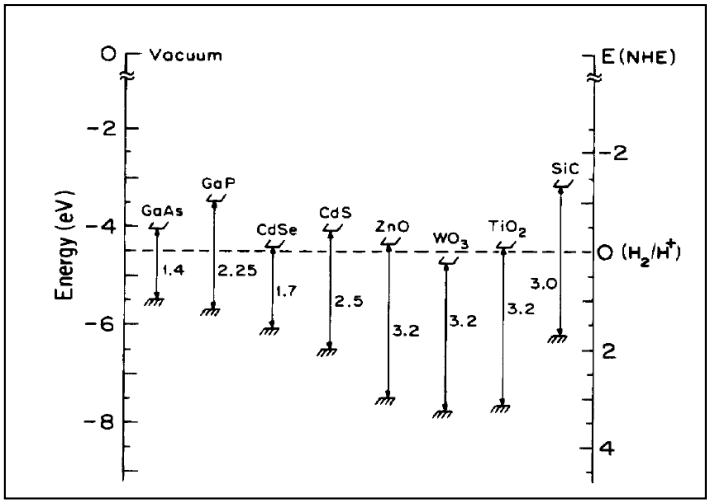

Figure 2-2 Energy band gap of various semiconductors in aqueous electrolyte at pH = 1 (Yoong et al. 2009)

Table 2.2 shows the physical and mechanical properties of TiO_2 researched by CREAM Research Ltd. during year 2002.

Table 2-2 Typical physical and mechanical properties of TiO2

Property	**Value**
Density	4 g/cm^3
Porosity	0 %
Modulus of Rupture	140 MPa
Compressive Strength	680 MPa
Poisson's Ratio	0.27
Fracture Toughness	3.2 Mpa/m$^{-1/2}$
Shear Modulus	90 GPa
Modulus of Elasticity	230 GPa
Microhardness (HV0.5)	880
Resistivity (25ºC)	10^{12}ohm.cm
Resistivity (700 ºC)	2.5x10^4 ohm.cm
Dielectric Constant (1MHz)	85
Dissipation factor (1MHz)	5x10^{-4}
Dielectric strength	4 kV/mm
Thermal expansion (RT-1000 ºC)	9x10^{-6}
Thermal Conductivity (25 ºC)	11.7 W/mk

2. 4 Hydrogen as an Alternative Energy

In recent application, most of the energy used is derived from fossil fuels (petroleum and coal). The combustion of these fuels will release carbon dioxide (CO_2) to the environment. The increases of greenhouse gases will contribute to the climate changes whilst these resources are consistently depleting (Solomon et al., 2009). Several alternatives have been developed such as wind, hydropower, solar, and geothermal-based renewable energy to fulfil the worldwide energy demand. However, several drawbacks emerged such as energy storage, high installation cost, and intermittent nature. In order to overcome these challenges, hydrogen is proposed which is also ideal energy storage medium or carrier due to the advantages such as (Liao et al., 2012):

i. The most abundant element that exists in both water and biomass
ii. Has higher energy yield (122 kJ/g) compared to conventional fuels such as gasoline (40 kJ/g)
iii. Environmentally friendly since it would not produce pollutants, greenhouse gases, or causes any harmful effect to environment
iv. Can be stored in gaseous, liquid or metal hydride form
v. Can be distributed over large distances through pipelines or via tankers.

According to Midilli et al. (2005), there are some limitations in hydrogen energy application technologies such as:

i. Advanced compression process is needed in minimize hydrogen storage volume
ii. Costly storage process for hydrogen hydride, since metal hydrides are expensive, heavy and have a limited lifetime
iii. Inadequate hydrogen fueling infrastructure and high production cost caused the difficulties in introduction of hydrogen vehicles into commercial market.

However, breakthrough was achieved through a promising technology, *viz*. photocatalytic water-splitting where “clean” hydrogen can be produced with the advantages as follow (Liao et al., 2012):

i. Reasonable solar-to-hydrogen efficiency
ii. Low processes cost

iii. The ability to achieve separate hydrogen and oxygen evolution during reaction

iv. Small reactor systems suitable for household application

2. 5 Mechanism of Photocatalytic Water-Splitting

The main processes of photocatalytic water-splitting can be categorized as below (Kudo & Miseki, 2008):

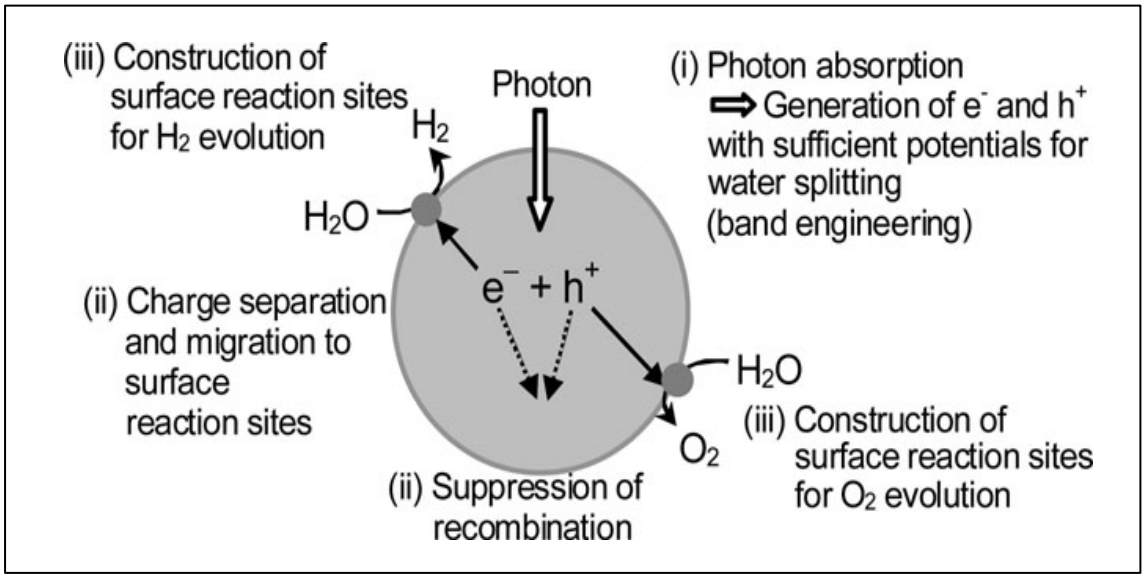

Figure 2-3 Main process in photocatalytic water splitting (Kudo & Miseki, 2008)

i. Absorption of photons to form electron-hole pairs

Most of the heterogeneous photocatalysts have semiconductor properties. Semiconductors have a conduction band, which is separated from the valence band by a band gap with certain band width. When the incident light energy is larger than the band gap, electrons and holes are generated. The photgenerated electrons and holes will induce redox reactions, which are water molecules are reduced by the electrons to form hydrogen (H_2) and oxidized by the holes to form oxygen (O_2) for overall water splitting. In this reaction, the semiconductor materials are determined by the band gap width and levels of the conduction and valance bands. At bottom level of conduction band, the energy is more negative than the redox potential of H^+/H_2 (0V vs. NHE), while the valance band top level has a more positive potential than the redox potential of O_2/H_2O (1.23V). Hence, the theoretical minimum band gap energy for water splitting is 1.23 eV or corresponding to light with 1100 nm.

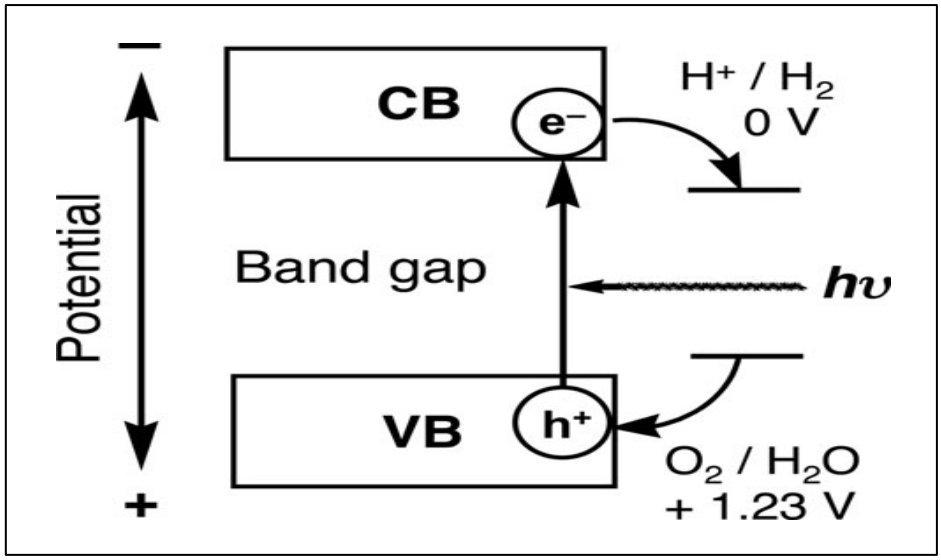

Figure 2-4 Principle of water splitting via semiconductor photo catalysis

ii. Charge separation and migration of photo generated carriers

Crystal structure, crystallinity and particle size are the major concern of water splitting. The higher the crystallinity, the smaller the defects detected. The defects operate acted as a trapping and recombination centres between photo generated electrons and holes, which will caused a decrease in photocatlytic activity. With a smaller particle size, the distance of the photo generated electrons and holes to migrate to surface reaction site will be shortening.

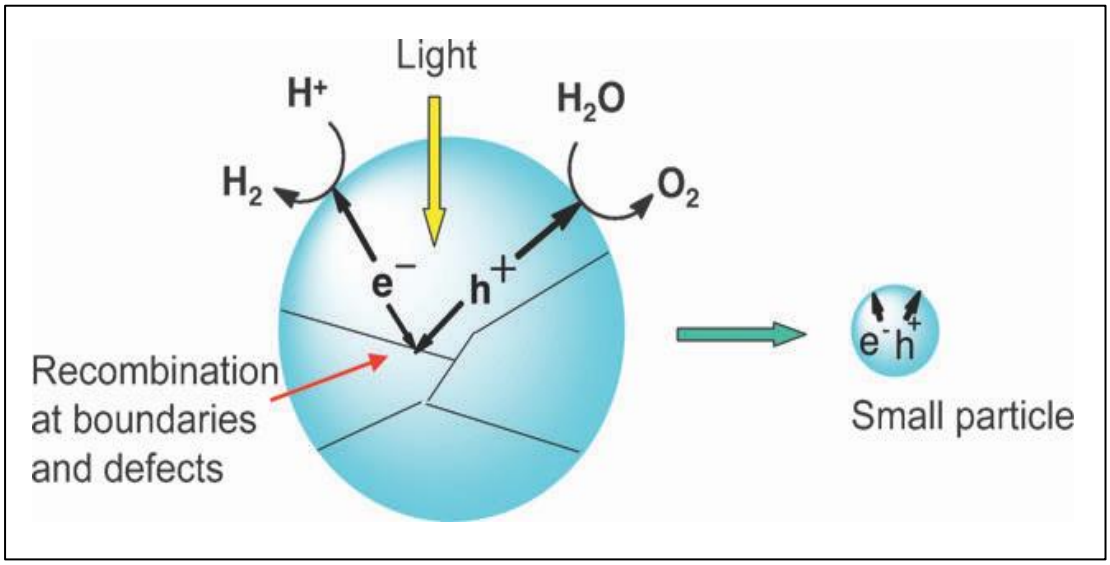

Figure 2-5 Effects of particle size and boundary on photocatalytic activity

iii. Surface chemical reactions

The major concerns of surface chemical reactions are the surface character (activities sites) and quantity (surface area). Although the photogenerated electrons and holes are possess thermodynamically suitable for water splitting. Usually, co-catalyst such as platinum (Pt), Nitrogen Oxide (NiO) and RuO_2 are loaded to introduce active site for hydrogen (H_2) production without catalytic assistance.

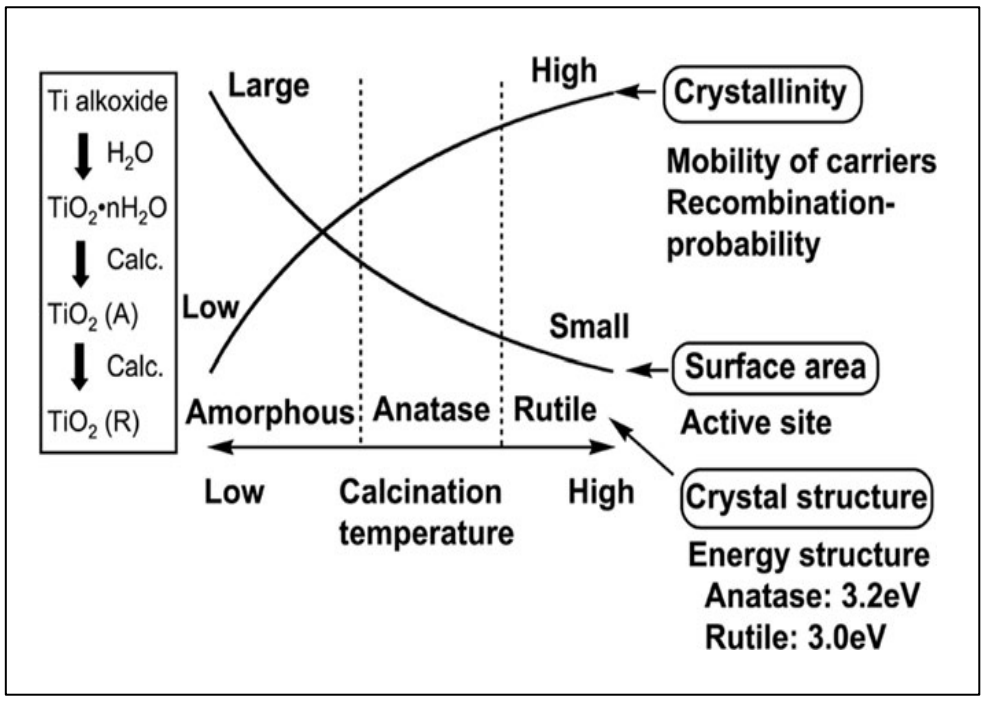

Figure 2-6 Conditions that will affect photocatalytic activity of TiO_2

2. 6 Characterization of Photocatalysis

Lattice structure of TiO_2 can be categorized into rutile and anatase, which have a higher photocatalytic activity (Augustynski, 1993). The unit cell structures of the rutile and anatase structure are shown in Figure 2.1 below:

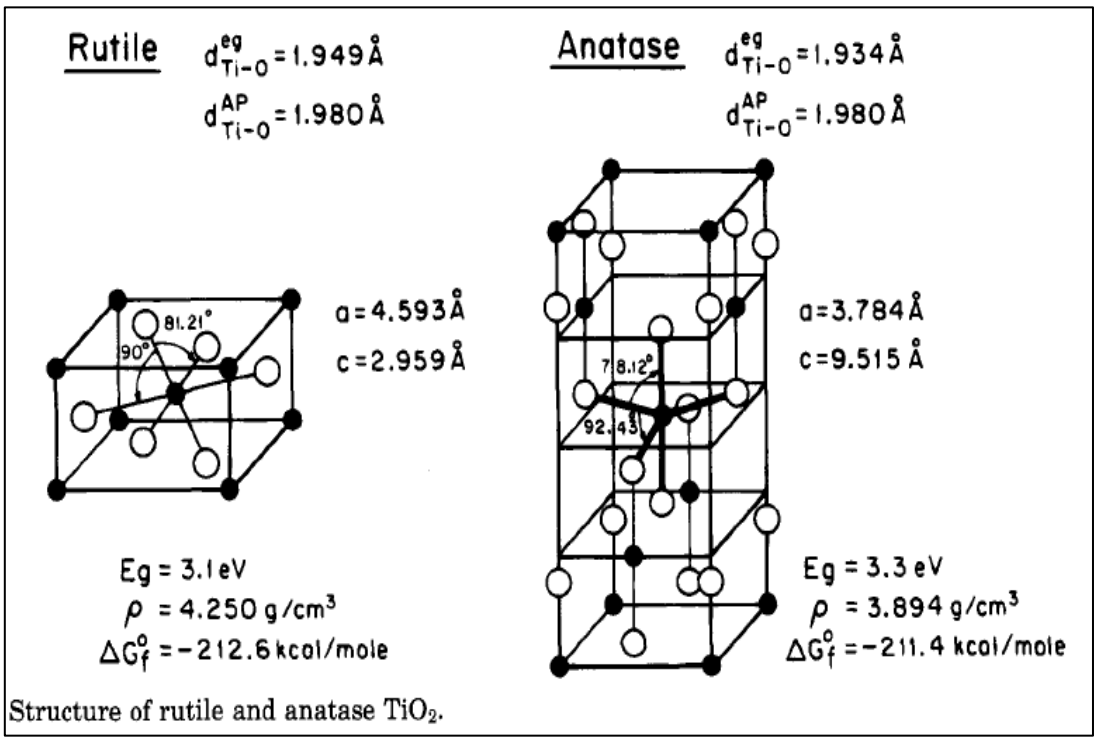

Figure 2-7 Structure of rutile and anatse TiO_2

These structures can be illustrated via a chain of TiO_6 octahedra, which are differ by distortion of each octahedron and octahedral chains assembly pattern. Each Ti^{4+} ions is surrounded by an octahedron with six O^{2-} ions, and causing rutile showing a slight orthorhombic distortion. As refer to Figure 2.1, its shows that a rutile structure is contact with 10 neighbour octahedrons (two sharing edge oxygen pairs and eight sharing corner oxygen atoms) while for anatase structure, each octahedron is in contact with eight neigbours (four sharing an edge and four sharing a corner). All these had indicate the different in mass densities and electronic ban structures for these two types of TiO_2 lattice structure.

Figure 2.8 below shows the geometric model structures for rutile single crystals – TiO_2 (110) surface, which is the most thermodynamically stable. According to Zschack (1991), this structure has three types of oxygen vacancy sites, besides

others faces will reconstruct as the structure is heating to high temperature. At this moment, this structure will produce (110) facets.

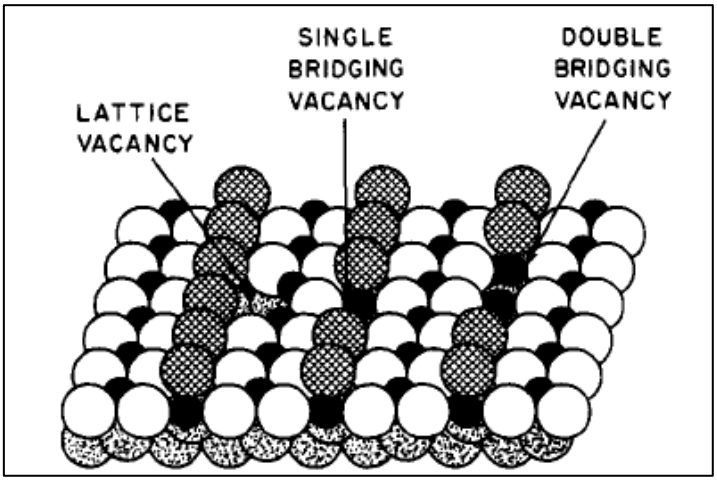

Figure 2-8 Defect sites of TiO_2 (110)

2. 7 Photochemistry of Water on TiO_2

H_2O cannot be photodecomposed on clean TiO_2 surfaces, even though TiO_2 can be easily photoexcited under band-gap irradiation. As refer to research done by Jaeger and Bard (1979), the band-edge positions of TiO_2 relative to electrochemical potentials of H_2/H_2O redox couple and O_2/H_2O redox couple had been illustrated in below Figure 2.3. It was shown that water photolysis is energetically favourable.

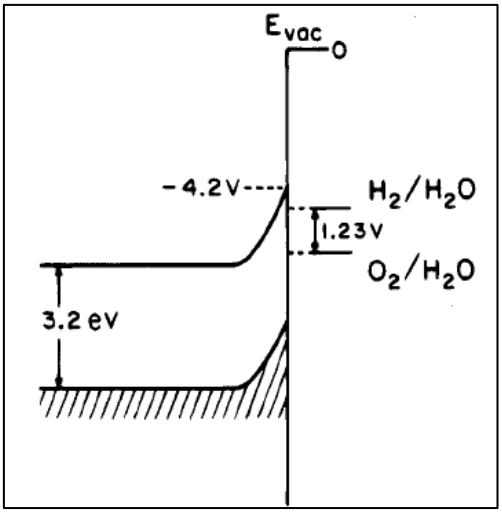

Figure 2-9 Potential energy diagram for the H_2/H_2O and O_2/H_2O redox couples relative to the band-edge positions for TiO_2.

Due to large overpotential for the evolution of H_2 amd O_2 on TiO_2 surface, TiO_2 will be inactive. This will induce photoassisted oxidation of oxygen vacancy sites on reduced TiO_2, for hydrogen evolution from wet TiO_2.

From past research experiment by Duonghong (1981), the experiment configuration is designed to separate the photogenerated electrons and holes for maximum photoreaction yield. From Figure 2.4 below, it shows that TiO_2 powders with deposited metal particles, e.g. Pt for H_2 evolution and metal oxide particles, e.g. RuO_2 for O_2 evolution. This is a short-circuited micro photoelectrochemical cell, which Pt is cathode and RuO_2 is anode. Band-gap excitation in the TiO_2 substrate injects negatively charged electrons into Pt particles, while holes with positive charge into RuO_2. Trapped electrons will reduce water to hydrogen and trapped holes in RuO_2 oxidized water to oxygen. Therefore, the presence of Pt and RuO_2 can reduce overpotential for H_2 and O_2 production.

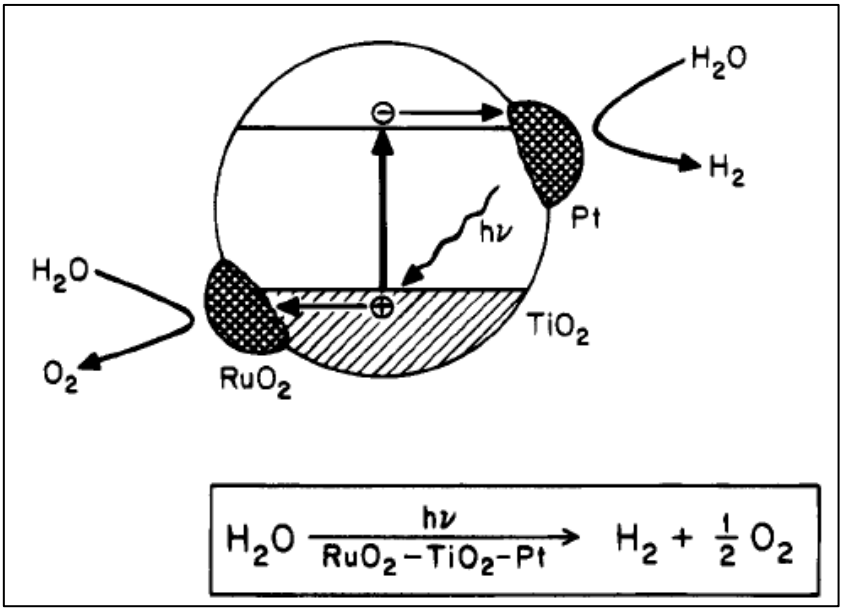

Figure 2-10 Photosplitting of water on composite catalyst

2.8 Chemisorption surface on TiO_2

2.8.1 Water Adsorption

The interaction between water and TiO_2 surfaces was stimulated by the photocatalytic splitting of water on TiO_2 electrodes, in which the surface hydroxyl groups present after H_2O adsorption at 300K on a slightly defective TiO_2(110) surface with photoemission (UPS) (Henrich et al). According to Madey group's research on synchrotron photoemission study, the amount of water dissociatively adsorbed at 300K was below one monolayer. Besides that, the coverage of OH(a) was found to be independent of the coverage of surface oxygen vacancy defeat sites, which would cause a slightly increase during H_2O adsorption on surface defeat coverage. Based on the results, it believed that an adsorbed H_2O molecule reacts with a bridging-oxygen atom to form OH groups at a temperature below 160K. Hydroxyl groups were produced by water dissociation upon heating the physisorbed layer to above 200K, where the hydroxyls were not completely removed from the surface until 350-400K.

According to Hunenschmidt et al. study on XPS and TPD on four different adsorption states for H_2O on TiO_2 (110). From the experiment result, it was found that a 500K TPD peak occurred due to surface hydroxyls bound to oxygen vancancies, a 375K peak due to dissociated H_2O adsorbed at Ti^{4+} sites, a 170K desorption feature due to molecular H_2O bound to bridging-oxygen anion sites, and lastly a 160K multilayer state. In addition to the molecular and dissociative adsorption, water molecules can be reduced at the Ti^{3+} sites on TiO_2 (110) surface to produce hydrogen gas (Lu et al.). The oxygen atom in the water molecule is preferentially extracted by the substrate to fill the surface oxygen vacancies. This selective reduction process can be used to infer the relative coverage of oxygen vacancy defeat sites.

The interaction of water with other single-crystal TiO_2 surfaces and powdered TiO_2 has been investigated by Bustillo et al. and Lo et al. According their study on the thermal desorption of water from the TiO_2 (100) surface, it was reported that there is a dissociative adsorption of water. On powdered TiO_2, three TPD peaks can be observed, where a poorly resolved doublet at 211K was attributed to multilayer and monolayer adsorption, a 311K desorption peak was assigned to a different form of molecularly adsorbed H_2O, and lastly a 568K desorption was thought to arise from dissociatively adsorbed H_2O. The production of hydrogen gas was also detected for

H_2O adsorption on reduced TiO_2 powder, indicating that the reduction property is characteristic of the Ti^{3+} defeat sites.

2.8.2 H_2 Adsorption

The adsorption of hydrogen on the $TiO_z(110)$ surface using temperature programmed desorption (TPD), electron paramagnetic resonance (ESR), and measurements of surface conductivity (Ao) and work function (Acp) had been studied by Gopel et al. The surface defect sites (oxygen vacancies) were found to act as electron donors, besides role as the specific sites for H_2 adsorption. After Hz dissociative adsorption at the defect sites, chemisorption of hydrogen at 300 K forms ionic titanium hydride bonds Ti^{4+}-H^-, in which it involves the transfer of two electrons before adsorption. They were attributed to one oxygen vacancy site (with two Ti^{3+} present), which caused two hydrogen atoms can easily recombine during subsequent thermal desorption measurements and exhibiting first-order desorption kinetics. The adsorbed hydrogen atoms also diffuse into the bulk at 300 K, causing a nearly linear increase in conductivity (Ao) when the $Ti0_2$ (110) crystal is exposed to a continuous flow of molecular hydrogen. An initial sticking coefficient of 1 x was reported for H_2 adsorption on TiO_2 (110) at 300 K. In the absence of surface defects, the activation energy to dissociate the H_2 molecule is too high, and no adsorption was observed.

A very low sticking probability for H_2 adsorption on TiO_{2-} (110) was studied by Pan et al. (1992), in which the hydrogen adsorotion was enhanced by low-energy H_2^+ ion bombardment. In addition, the surface Ti^{3+} coverage was found to increase with increasing hydrogen exposures, together with surface hydroxyl groups were generated upon hydrogen ion exposures.

On powdered TiO_2 surfaces, Beck et al. reported TPD spectra typical of weakly adsorbed molecular hydrogen, while different adsorption behavior for hydrogen on anatase and on rutile TiO_2 was observed by Iwaki. On both types of TiO_2 powders, chemisorption of hydrogen took place only when hydrogen was introduced above 623K.

2. 9 Photodecomposition of Organic Dyes

As an environmental application, photocatalysis process is a relatively novel subject with tremendous potential in the future (Al-Rasheed, 2005). A lot of organic matters can be decomposed into inorganic and low-toxicity smaller compound through photocatalysis process (Meng & Juan, 2008). Photocatalysis reaction needs only light, catalyst as well as air, and the processing cost is lower; hence becoming a new promising method for liquid waste processing. However, different types of catalysts will significantly affect the efficiency. A wide range of semiconductors may be used for photocatalysis, viz. TiO_2, CdS, SnO_2, WO_3, SiO_2, ZrO_2, ZnO, Nb_2O_3, Fe_2O_3, $SrTiO_3$, CeO_2, Sb_2O_4, V_2O_5 etc. (de_Richter & Caillol, 2011).

Significantly, voluminuous publications of past photocatalysis research works can be found in the open literature. Some of the signifantly important past research works are summarized in the Table 2.3.

Table 2-3 The summary of past researches on photocatalysis process.

Photocatalyst	Activator	Substrate	Results	Reference
Manganese oxides	UV-light	Phenol	92% of the substrate decomposed.	Zhang et al. ,2011
TiO_2	UV-light	Methyl orange	71.9% of methyl orange degraded.	Liao et al., 2004
Cu–Cr layered double hydroxide (LDH)	Visible light	2,4,6-Trichlorophenol	Less than 10% of 2,4,6-Trichlorophenol present after 200 minutes	Tian et al., 2012
Fe_2O_3–TiO_2/ACF	Visible light	Methyl orange	$[C/C_o]$ ratio of methyl orange dropped to 0.32 after exposing under sun for 4 hours.	Zhang & Lei, 2008
Fe_2O_3 and ZrO_2/Al_2O_3 (9.1, 31.5, 54.1 wt% respectively)	UV-light	Phenol	93% phenol removed after 120 minutes.	Liu et al., 2012
Fe_2O_3/SnO_2	Visible light	Acid blue 62	98.0% acid blue 62 can be degraded in 60 min under illumination of the visible light	Xia et al., 2008
CeO_2	UV-light	Methylene blue	Almost 100% methylene blue is converted over 100 minutes.	Qian et al., 2010
CeO_2	UV-light	Toluene	Deactivation of catalyst doesn't occurs.	Hernández-Alonso, 2004

CHAPTER 3

MATERIALS AND METHODS

3. 1 Introduction

This chapter details the preparation method for the Cu/TiO_2 photocatalyst. Besides that, description of the method and characterization technique will also be provided. The characterization techniques including X-ray fluorescence (XRF) for elemental compositions, liquid-nitrogen physisorption for BET specific surface area and pore size distribution, thermo gravimetric analysis (TGA) for thermo physical change, gas pycnometer for density determination and X-ray diffraction (XRD) for crystalline structure scanning. Moreover, the operational procedures for the photoreaction of glycerol solution will also be discussed in this chapter.

3. 2 Chemicals

Table 3.1 shows the chemicals employed in the catalyst preparation, photocatalytic reaction and photocatalyst characterization. These chemicals were get from Sigma-Aldrich. The distilled water was readily availabled from the water purification system in the laboratory of Universiti Malaysia Pahang (UMP).

Table 3-1 Lists of chemicals

Chemical	Purity	Application
Degussa P25 TiO_2	80% anatase, 20% rutile, BET surface area	Catalyst preparation
$Cu(NO_3)_2.3H_2O$	>98%	Catalyst preparation
Glycerol solution	95%	Photocatalytic reactant

The gases required in the study were listed in Table 3.2. All gases used in this project were supplied by MOX. Table 3.2 also listed the purity of the gases and their application in this study.

Table 3-2 Lists of gases

Chemical	Purity	Application
Degussa P25 TiO_2	80% anatase, 20% rutile, BET surface area	Catalyst preparation
$Cu(NO_3)_2.3H_2O$	>98%	Catalyst preparation
Glycerol solution	95%	Photocatalytic reactant

3. 3 Photocatalyst Preparation

The Cu content in the photocatalyst will affect the physicochemical properties, activity of photocatalyst and also affect the photoreaction of glycerol solution. Since catalyst design was a major part of this work, careful attention was devoted to the preparation of all catalysts including monitoring and controlling related variables especially the concentration of the copper precursor solution as it will decide the loading percentage of the catalyst. Besides the concentration of the precursor, the drying temperature and the calcination temperature of the catalysts were also strictly controlled throughout the catalyst preparation. Furthermore, the time of stirring after the solutions mixed must be long enough to allow the mixing process accomplished. An analytical balance (4-decimal accuracy) was used for weighing chemicals in all preparations.

The photocatalyst used in the present study is Cu/TiO_2. According to Yoong et al. (2009), the advantage of copper doping onto TiO_2 semiconductor photocatalyst was the enhancement of photocatalytic activity. Hence, the preparation procedure used in this study was followed the wet impregnation method described by Yoong et al. (2009). Wet impregnation is a widely used catalyst preparation technique where the precursor material was dissolved in a solvent and mixed with the solid support.

Degussa P25-TiO_2 photocatalyst containing predominantly anatase phase and having a specific surface area of 50 m^2/g was sourced from Sigma-Aldrich. The mass ratio of metal dopant precursor, copper nitrate trihydrate, $Cu(NO_3)_2.3H_2O$ (Sigma-Aldrich, >98% purity), and TiO_2 was calculated and weighed accurately and mixed in a 250 mL beaker. 100 mL of deionized water was added to the solid mixture to

dissolve the copper precursor. The solution was magnetic-stirred for 3 hour. Subsequently, the slurry-containing beaker evaporated at 393 K using an oven for overnight to allow the precursor deposition onto the base material. Finally, the solid left-over was air-claimed at 573 K for 30 min. Preparation of different metal loadings was followed the same outlined procedures but different weight ratio of $Cu(NO_3)_2.3H_2O$ and TiO_2.

3. 4 Photocatalyst Characterization

Catalyst characterization provided useful information on the physicochemical properties of the catalyst. The information from various characterization techniques enabled to improve the understanding of the physicochemical attributes in relation to the photocatalytic performance. The following subsection described the fundamental theory and concepts of these characterization techniques used in this work.

3.4.1 X-ray Fluorescence (XRF)

X-Ray Fluorescence (XRF) functions via the emission of characteristic "secondary" (or fluorescent) X-rays from a material that had been excited by high-energy X-rays or gamma rays bombardment. XRF analysis is one of the most common non-destructive methods for qualitative or quantitative determination of elemental composition of solids, liquids as well as powders (Arezki, n.d.). According to Shackley (2011), when a substance was irradiated with high energy X-rays, electron ejected ion from the atom then produced ion, the shells of an atom were called and read by the software as K through orbital (cf. Figure 3.1). The K line transition was where the K electron moved out of the atom entirely and was replaced by an L line electron and these K and L lines were technically measured with XRF.

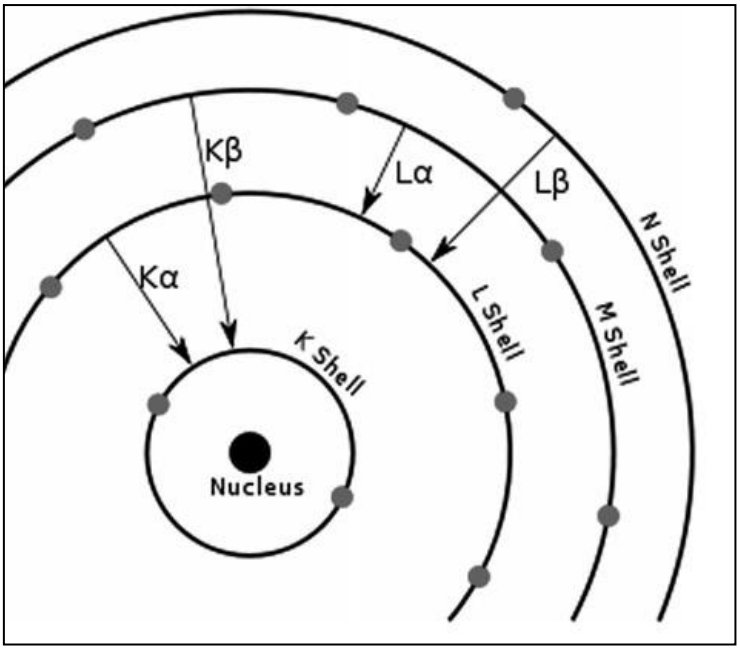

Figure 3-1 Schematic view of orbital transitions due to XRF

According to James (2012), modern XRF instruments in use today can be classified into energy-dispersive (ED) or wavelength-dispersive (WD). In the current work, the wavelength-dispersive XRF (brand S8 Tiger, Bruker) was employed. Figure 3.2 shows the diagram of WD system. The instrument operates based on the principle of Bragg diffraction of a collimated X-ray beam. The beam emanating from the sample, then the detector was angularly scanned relative to the analyzing crystal, registering the spectrum (Jenkis, 1995).

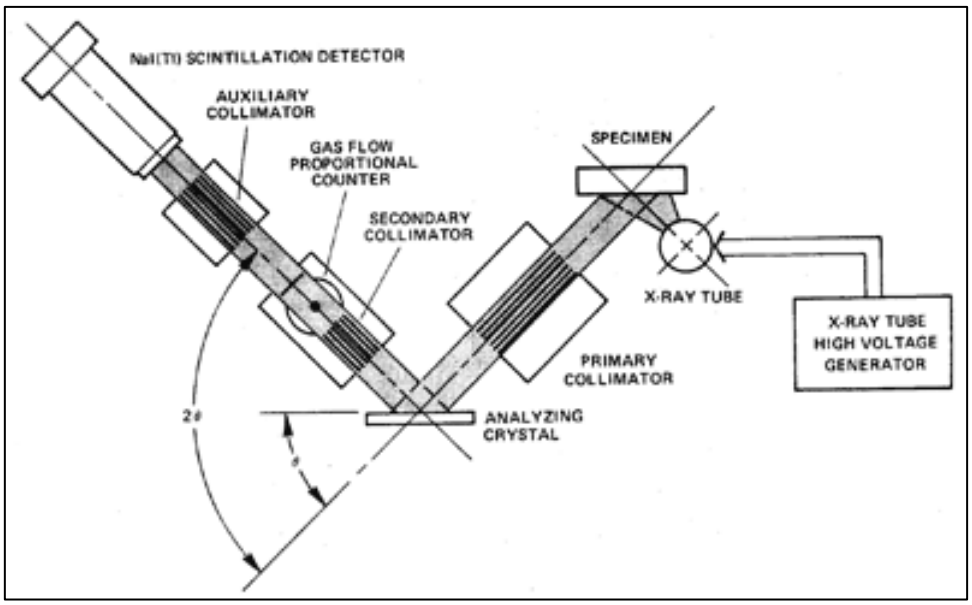

Figure 3-2 Diagram of a wavelength dispersive spectrometer (Jenkis, 1995)

Usually collimators were made from a series of closely spaced parallel metal plates, these metal plates needed to direct to beam in order to closely control the diffraction angle of all detected photons. The analyzing crystal angularly dispersed incident radiation of wavelength according to Bragg's Law:

$$n\lambda = 2d\sin\theta \qquad (3.1)$$

where

n = the order of reflection (integer)

λ = wavelength of x-ray beam (nm)

d = inter plane distance of crystal (d-spacing)

θ = angle of incidence (degree)

The analyzing crystal may be rotated with the detector assembly simultaneously revolving around it to scan through the possible wavelengths. Crystals with large spacing was used to resolve the wavelengths in all regions (James, 2012).

3.4.2 X-ray Diffraction (XRD)

X-ray diffractometer (XRD) is an instrumental techniques used for phase identification, qualitative and quantitative analysis and quality control of raw materials and products. According to Barbara and Christine (2012), XRD was based on the constructive interference of monochromatic X-rays and a crystalline sample. The X-rays were generated by a cathode ray tube, filtered to produce monochromatic radiation, collimated to concentrate and directed towards the sample. The interaction of the incident rays with the sample produced constructive interference when conditions satisfy Bragg's Law as in Equation (3.1).

This law relates the wavelength of electromagnetic radiation to the diffraction angle and the lattice spacing in a crystalline sample. These diffracted X-rays were then detected, processed and counted. By scanning the sample through a range of 2θ angles, all possible diffraction directions of the lattice were attained due to the random orientation of the powdered material.

The mean crystallite size may be obtained by the Scherrer equation:

$$D = \frac{k_{Sch}\lambda}{\beta_d \cos\theta} \tag{3.2}$$

where

D = crystalline size (Å)

k_{Sch} = Scherrer constant

β_d = angular width of half-maximum intensity (degree)

λ = X-ray wavelength

θ = Bragg's angle (degree)

In current work, XRD analysis was carried out in Rigaku Miniflex II, which is a desktop powder diffractometer capable of measuring powder diffraction patterns from 3 to 145^o in *2θ* scanning range and equipped with a six sample holders for maximum automation of sample measurements. The X-ray radiation of the CuKα radiation filtered by a Ni filter has a wavelength of 1.54 Å. Figure 3.3 shows the schematic of XRD.

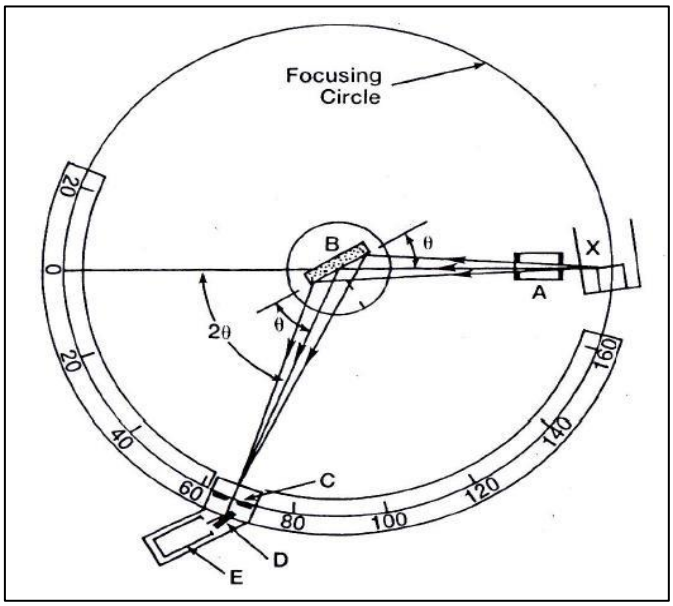

Figure 3-3 A schematic diagram of XRD (A) Collimation (B) Sample (C) Slit (D) Exit Beam Monochromator (E) Detector (X) Source of X-Rays (Cullity, 1978)

3.4.3 Liquid N_2 Physisorption (Brunauer-Emmett-Teller, BET)

Brunauer-Emmett-Teller (BET) method (Brunauer et al., 1938), which is an extension of the Langmuir's pioneer work (Langmuir, 1916) for monomolecular adsorption is widely used. The specific surface area of a powder was determined by physical adsorption of a gas on the surface of the solid by calculating the amount if adsorbate gas corresponding to a monomolecular layer on the surface. The most commonly used adsorbate is N_2, which had cross-sectional area of 16.2 $Å^2$. Therefore, the adsorption of N_2 was carried out at the N_2 boiling point of about 77.4 K. The determination method was carried out at the temperature of the liquid nitrogen. BET equation is shown as:

$$\frac{1}{[V_a(\frac{P_o}{P}-1)]} = \frac{C-1}{V_m C} \times \frac{P}{P_o} + \frac{1}{V_m C} \tag{3.3}$$

where

P = partial vapor pressure of absorbate gas in equilibrium with the surface at 77.4K

P_o = saturated pressure of adsorbate gas

V_a= volume of gas adsorbed at standard temperature and pressure (STP)

V_m = Volume of gas absorbed at STP to monolayer coverage

C = dimensionless constant of adsorbate

V_a was measured at each of not less than three values of P/P_o. The BET value was plotted against P/P_o according to equation (3.3). The plot was yield a straight line usually in the approximate relative pressure range 0.05 to 0.3, the data was considered acceptable if the correlation coefficient, r, of the linear regression was not less than 0.9975. From the resulting linear plot, we can get:

$$\text{Slope} = \frac{(C-1)}{V_m C} \tag{3.4}$$

$$\text{Intercept} = \frac{1}{V_m C} \tag{3.5}$$

$$V_m = \frac{1}{(\text{Slope} + \text{Intercept})} \tag{3.6}$$

$$C = \left(\frac{\text{Slope}}{\text{Intercept}}\right) + 1 \tag{3.7}$$

Then, the specific surface area can be calculated from Equation (3.8):

$$S = \frac{V_m N a}{m \times 22400} \tag{3.8}$$

where

N = Avogadro constant (6.022×10^{23} mol^{-1})

a = effective cross-sectional area of one adsorbate molecule

m = mass of solid catalyst

The total pore volume was derived from the amount of vapour adsorbed at a relative pressure close to unity, by assuming that the pores are then filled with liquid N_2. If the solid material contains no macropores (pore width > 50 nm), the isotherm will remain nearly horizontal over a range of P/P_o near the unity (cf. Figure 3.4) and the pore volume was well defined.

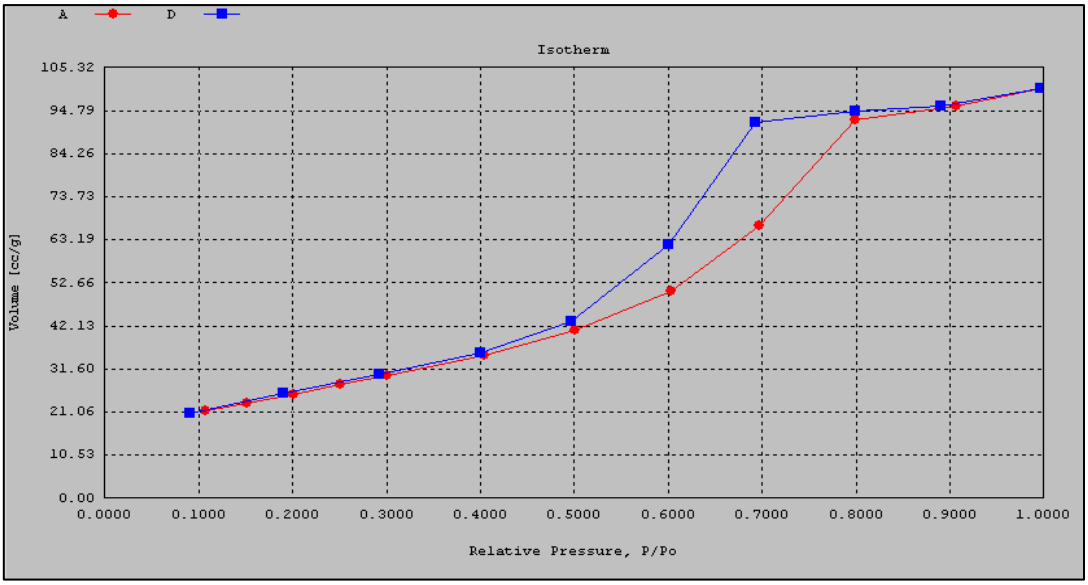

Figure 3-4 Typical N_2 adsorption-desorption isotherms of mesoporous materials

Nevertheless, the isotherm rose rapidly near P/P_o close to 1 for macropores, and in this case it may exhibit an essentially vertical rise (cf. Figure 3.5). Thus, the limiting adsorption may be identified with the total pore volume. The volume of nitrogen adsorbed (V_{ads}) can be converted to the volume of liquid N_2 (V_{liq}) contained in the pores using Equation (3.9):

$$V_{liq} = \frac{P_a V_{ads} V_m}{RT} \tag{3.9}$$

where

P_a = Ambient pressure

T = Ambient temperature

V_m = Molar volume of the liquid N_2 (34.7 $cm^3.mol^{-1}$)

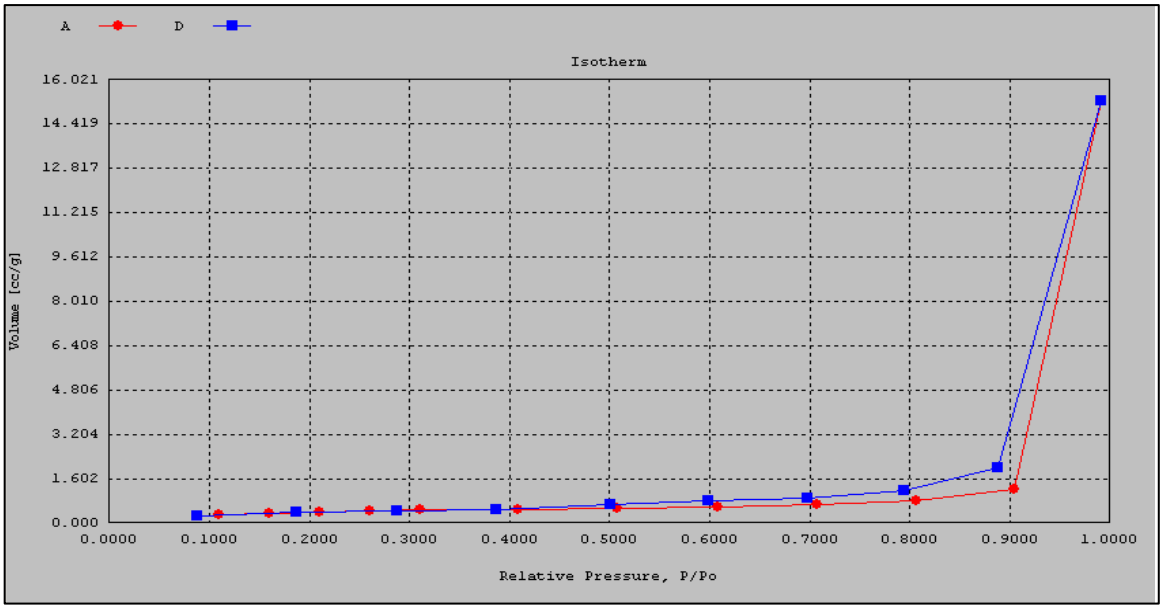

Figure 3-5 Typical N_2 adsorption-desorption isotherms of large macroporous materials

Since pores which would not be filled below a P/P_o of 1 had a negligible contribution to the total pore volume, the average pore size can be estimated from the pore volume. The distribution of pore volume with respect to pore size was known as a pore size distribution. It was generally accepted that the desorption isotherm was more appropriate than the adsorption isotherm for evaluating the pore size distribution of a solid material. The desorption branch of the isotherm exhibited a lower relative pressure (P/P_o) resulting in a lower free energy state, and therefore the desorption isotherm was closer to the true thermodynamic stability (Gregg & Sing, 1982).

Thermo-Scientific Surfer offers the capability of using either branch of the isotherm for the pore size distribution calculation. Mesopore size calculations were executed by assuming cylindrical pore geometry using the Kelvin equation (Gregg & Sing, 1982):

$$r_k = \frac{-2V_m\gamma}{RT\ln(P/P_o)} \tag{3.10}$$

where

γ = the surface tension of N_2 at its boiling point (8.85 ergs.cm^2 at 77.4 K)

V_m = the molar volume of liquid N_2 (34.7 cm^3/mol)

R = gas constant (8.314 E^7 ergs/K.mol)

T = N_2 boiling point (77.4 K)

P/P_o = relative pressure of N_2

r_k = the Kelvin radius of the pore

Using the appropriate constants for N_2, above equation reduces to:

$$r_k = \frac{4.15}{\log(P/P_o)} \tag{3.11}$$

The Kelvin radius is the radius of the pore in which condensation happens at P/P_o. However, r_k does not represent the actual pore radius because some adsorption had taken place prior to condensation on the walls of the pore. In addition, during desorption, an adsorbed layer remained on the walls when evaporation occurs.

Therefore, the actual pore radius (r_P) is given by:

$$r_p = r_k + t \tag{3.12}$$

wheret is the thickness of the adsorbed layer. The t-value was estimated by a method proposed by de Boer et al., (1966) as:

$$t = \left[\frac{13.99}{\log(P/P_o) + 0.034}\right]^{1/2} \tag{3.13}$$

Thermo-Scientific Surfer computed the pore size distribution using the methods proposed by Barrett, Joyner, and Halenda (BJH) (Barrette et al., 1951) and by Dollimore and Heal (DH) (Dollimore & Heal, 1964). However, the BJH method is the most widely used for the computation of the pore size distribution (Sing & Rouquerol, 1997). The BJH procedures are based on the emptying of the pores by a step-wise reduction of P/P_o, and the derived pore size distribution is normally expressed in the graphical form ($\delta V_P / \delta r_P$) versus r_P or d_P.

3.4.4 Thermogravimetric Analysis (TGA)

Thermogravimetric Analysis (TGA) is a technique in which the mass of a substance is monitored as a function of temperature or time as the sample specimen is subjected to a controlled temperature program in a controlled atmosphere. In short, TGA is that upon heating a material, its weight increase or decrease.

The fundamentals principles are:

- Changes in the mass of a sample are studied while the sample is subjected to a controlled temperature programme.
- The temperature programme is most often a linear increase in temperature, but, isothermal studies can also be carried out, when the changes in sample mass with time are followed.
- TGA is inherently quantitative, and therefore an extremely powerful thermal technique, but gives no direct chemical information.

Table 3.3 shows the process that lead to weight gain or loss in TGA experiments.

Table 3-3 Process that lead to weight gain or loss in TGA experiments

Process	Weight Gain	Weight Loss
Ad- or absorption	✓	
Desorption, drying		✓
Dehydration, desolvation		✓
Sublimation		✓
Vaporization		✓
Decomposition		✓
Solid-solid reactions (some)		✓
Solid-gas reactions	✓	✓
Magnetic transitions	✓	✓

Figure 3.6 shows the instrumentation flow diagram of TGA. Temperature programmer is the typical operating range for the furnace which is ambient to 1773 K, with heating rates up to 473 K/min. The inner of the furnace consists a sample holder or pan to hold the sample, the furnace's atmosphere can be reactive or inert. The TGA

was connected to the computer which acts as the controller and also the results showed in the computer in form of thermogram. Thermogram is a graph of mass versus temperature (Figure 3.7). With the drawing of tangent on the curve, the onset and offset points can be determined (Figure 3.8). Figure 3.9 shows the typical curve that can be obtained from thermogram.

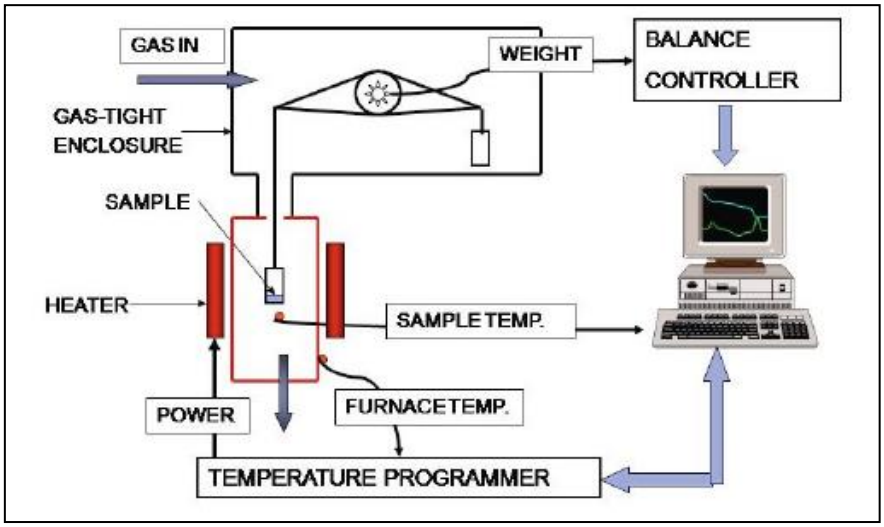

Figure 3-6 Instrumentation flow diagram of TGA

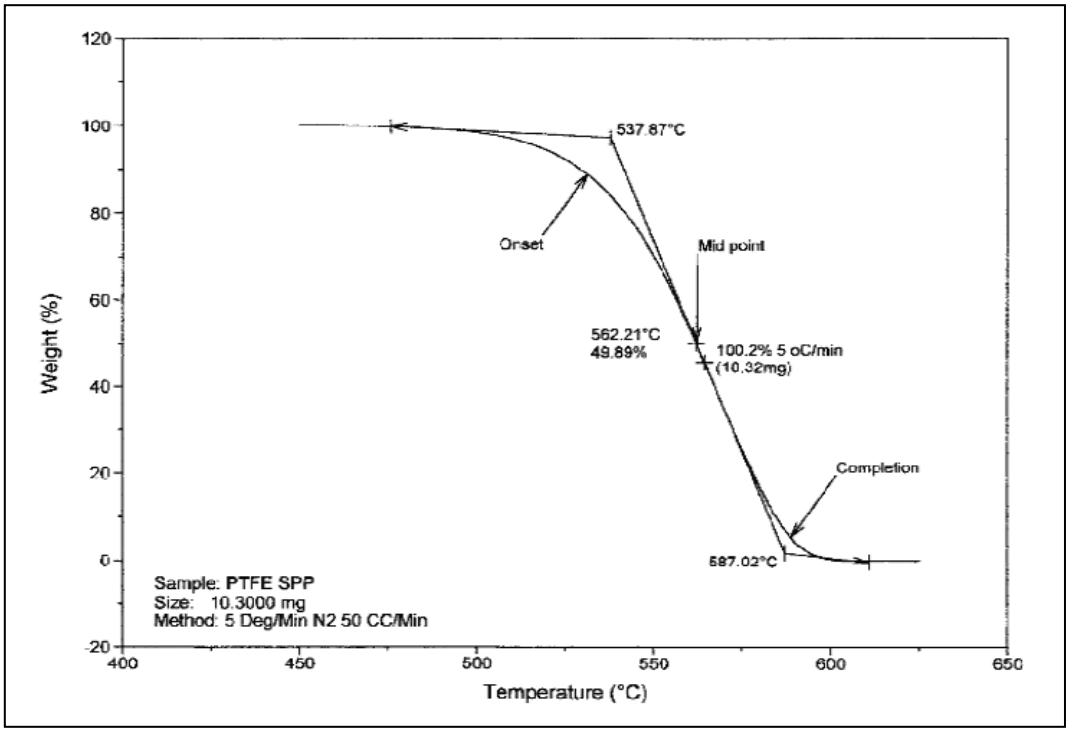

Figure 3-7 Thermogram

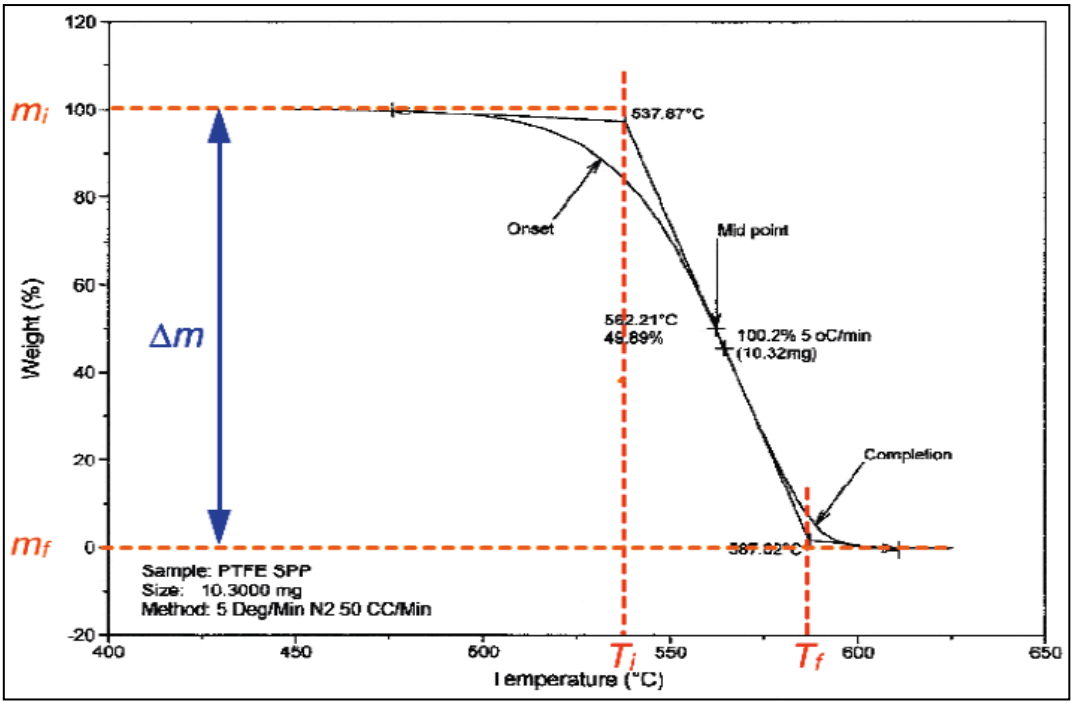

Figure 3-8 Tangent curve to find onset and offset points

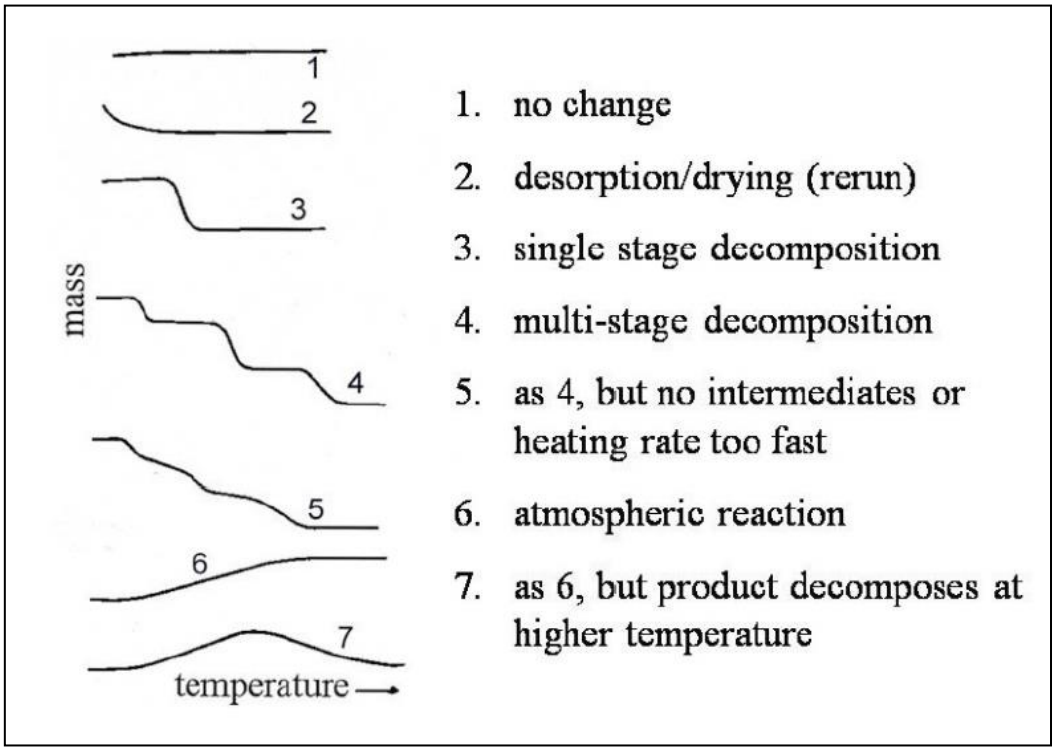

Figure 3-9 Typical TG curves

3.4.5 Gas Pycnometer

The volume and density of powders, porous and irregularly shaped solids can be obtained rapidly and accurately by using gaseous pycnometer. The air was employed for inert low-surface materials on which negligible adsorption of gas occurs; while helium, an inert gas was employed for the fine powders or porous materials, and the activated samples with high surface area (Edward, 1969).

According to Tamari et al. (2004), there are three types of gas pycnometer, which are constant volume, variable volume and comparative. Figure 3.10 shows a constant volume helium gas displacement Pycnometer type 1305 Micromeritics. A constant-volume gas pycnometer was composed of a sample chamber with a screw cap, a tank and an absolute pressure transducer. The chamber and tank were connected pneumatically through a tube with coupling valve, the tank also connected to the pressure transducer so that the helium gas supply through the tube with a main coupling valve. The powder was put inside the chamber and weighted, then insert into the gas pycnometer to analyze the volume and the density. The test was set as five cycles in order to get a more accurate result.

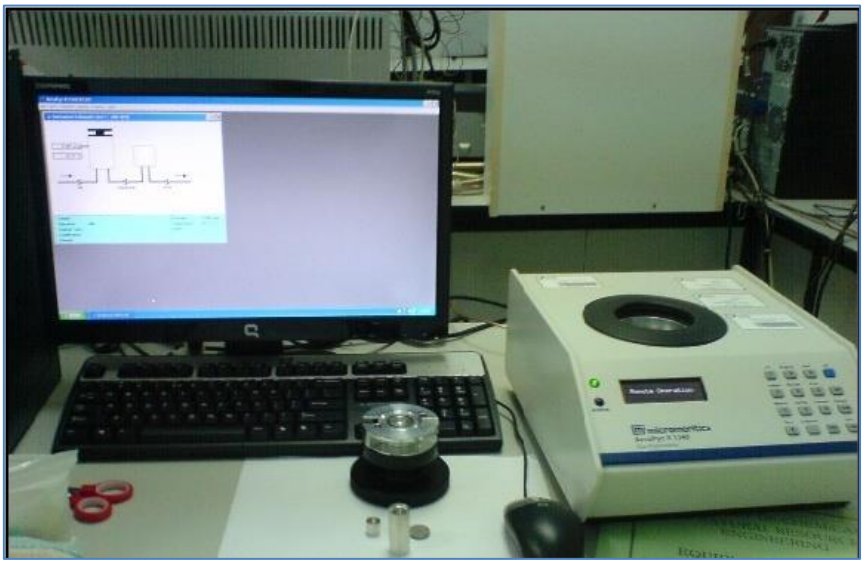

Figure 3-10 Helium gas displacement Pycnometer type 1305 Micromeritics

3. 5 Photoreaction

3.5.1 Photodecomposition of Methylene Blue

The reactions were performed at the atmospheric pressure and room temperature. standard calibration curves for MB would be obtained via UV-Vis spectrophotometer. Subsequently, aqueous slurry was obtained by adding 0.25 g of photocatalyst to 300 ml MB aqueous solution at 10 ppm. Irradiation was performed with a 1000-W high pressure UV-lamp. The aqueous slurry was rigorously stirred for 30 min prior to irradiation to attain equilibrated-adsorption state. During the photoreaction, at 15 min intervals, the suspension was withdrawn and centrifuged to separate the photocatalyst particles followed by UV-Vis measurement at absorbance peak of 664 nm. The actual concentration of each sample was obtained by referring back to the calibration curve obtained in prior.The photoreaction (cf. Figure 3.11) testings were conducted in the following sequence:

1. Catalyst screening via photoreaction over 2, 5, 10, 15, 20 and 25 wt% Cu/TiO_2.
2. The best conversion of MB achieved by the prepared photocatalyst was duly indentified from Step (1). Subsequently, the reactions were conducted to investigate the effects of different loading viz. 0.06g, 0.15 g and 0.30 g over the best photocatalyst.
3. The best conversion of photocatalyst was chosen from Step (1), then the reactions were performance with different concentrations, which were 10ppm, 15ppm, 20ppm, 25ppm and 30ppm.

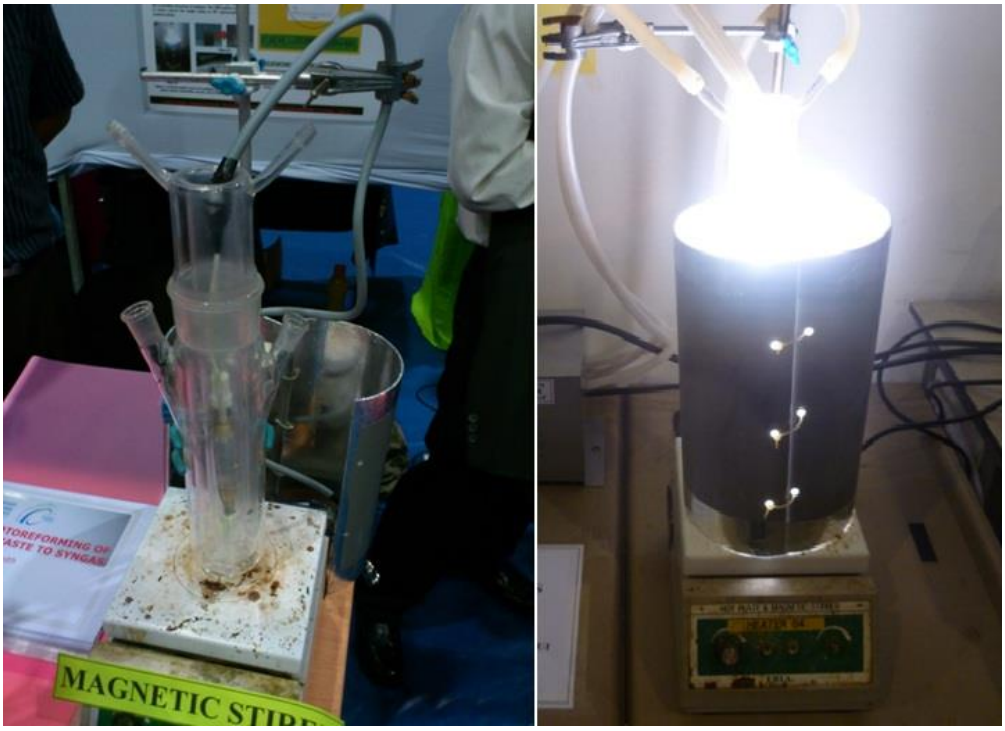

Figure 3-11 Photoreaction of methylene blue solution

3.5.2 Photo-splitting Water

There are several types of apparatus for water splitting. The photocatalytic material was evaluated for hydrogen production in 500ml a gas-closed circulation system. The temperature was maintained at 298 K via water-circulation cooling system. For each runs, 0.5 g of each photocatalysts was suspended in 500 ml of pure water. The suspended photocatalysts were bubbled with N_2 gas to de-aerate for 30 min. The effluent gas produced through photocatalytic reaction was analyzed by gas chromatography (GC) using TCD detector.

CHAPTER 4

RESULTS AND DISCUSSION

4. 1 Introduction

In this chapter, physicochemical properties of the photocatalysts were characterized via several well-established techniques viz. XRD, XRF, BET and TGA. Subsequently, photodegradation of methylene blue solution were tested by photocatalysts prepared followed by photoreaction of water-splitting. Besides that, this chapter also include Langmuir-Hinshelwood Modeling and correlations between the photocatalytic activity and the physicochemical properties .

4. 2 Characterization of Catalysts

4.2.1 Liquid N_2 physisorption (BET)

The adsorption-desorption isotherms for the prepared catalysts are shown in Figure 4.1. The surface area, pore volume and pore diameter were determined based on these isotherms.

N_2 physisorpion isotherns were determined at liquid nitrogen temperature (77 K) using a Thermo-Scientific Surfer. The specific surface areas of calcined Cu/TiO_2 photocatalyst ware calculated from the N_2 adsorption data according to the Brunauer-Emmett-Teller (BET) method using P/P_o values in the range 0.05-0.2. Figure 4.1 shows typical adsorption/desorption isotherms of all the photocatalysts. All samples had similar N_2 physisorption isotherms that could be classified as Type II accordingly to IUPAC convention foe adsorption isotherms. According to Rouquoel (2013), the characteristic of this type of isotherm is symptomatic of type II isotherm which represents unrestricted monolayer-multilayer adsorption, which the intermediate flat

region often taken to indicate the stage at which monolayer coverage is complete and multilayer adsorption about to begin.

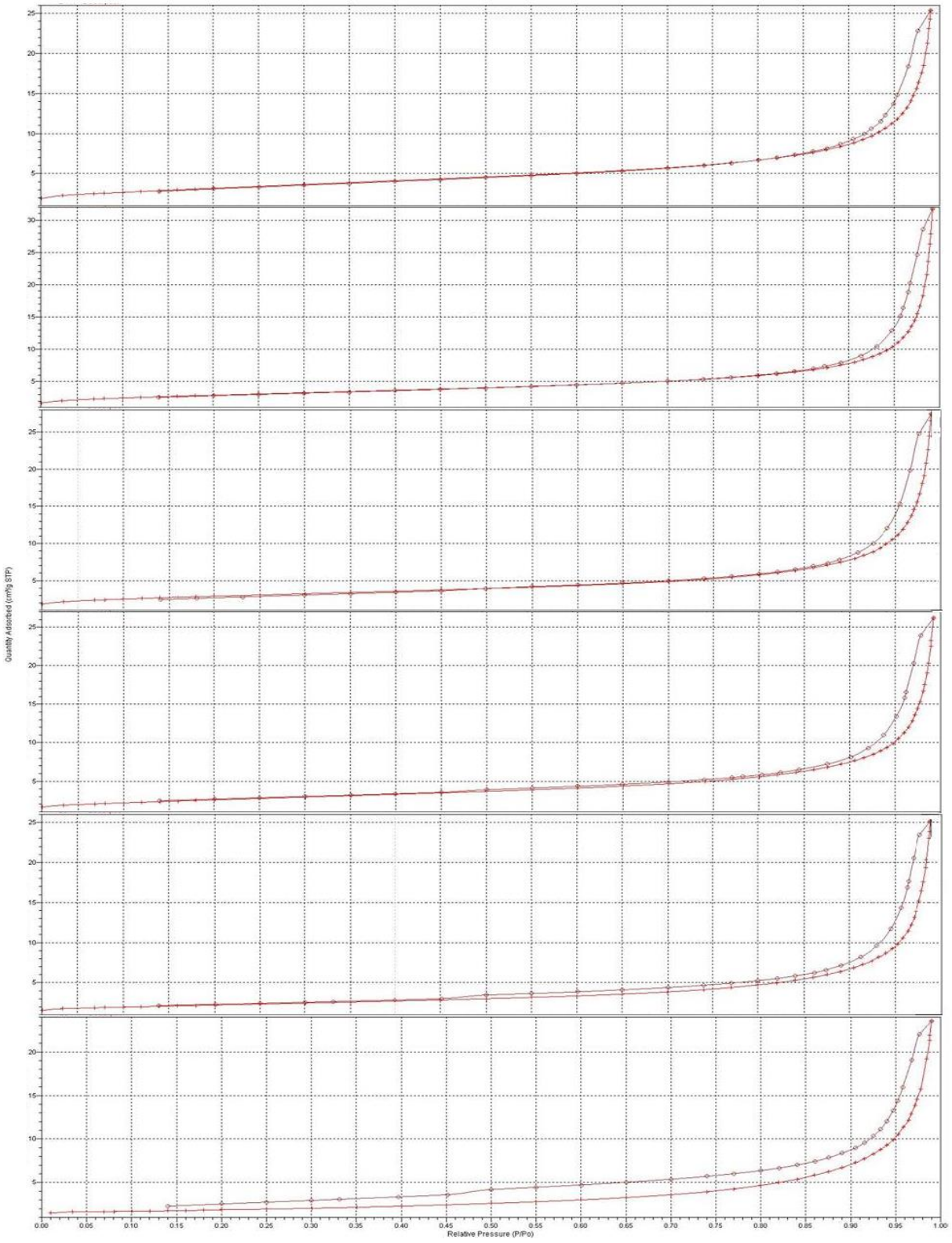

Figure 4-1 The isotherms for 2wt%, 5wt%, 10wt%, 15wt%, 20wt%, and 25wt% of Cu/TiO2 (from top to bottom)

The BET specific surface area of the catalysts obtained from liquid N_2 physisorption is shown in Table 4.1. The BET surface areas of the photocatalysts generally decreased as the CuO loading increased. The highest measured surface area was 11.42 m^2/g for 2 wt% Cu/TiO_2 This can be explained by the crystallite formed upon the impregnation of Cu metal that has blocked the pores of TiO_2 support; hence a decrease in BET specific surface area.

Table 4-1 The BET specific surface area for different loadings of Cu/TiO_2.

Wt% of Cu/TiO_2	**BET specific surface area (m^2/g)**
0	12.92
2	11.42
5	10.23
10	9.98
15	9.17
20	7.49
25	6.20

The volume of the pores and pore diameter of prepared photocatalysts were shown in Table 4.2. BJH cumulative pore volumes and BJH average pore diameters for all Cu/TiO_2 samples were in the range 0.0367-0.0400 cm^3g^{-1} and 13.9-23.4 nm, respectively. As for pore volumes, there were not much difference between the adsorption and desorption volume for each of the catalysts. The 5wt%Cu/TiO_2 seems to have largest adsorption and desorption volume, which are 0.049 and 0.0496 cm^3/g respectively. Unlike pore volume, the difference between adsorption pore diameter and desorption pore diameter is quite significant. Generally, the adsorption pore diameter is larger than desorption pore diameter. According to Table 4.2, 20wt% Cu/TiO_2 seems to have the largest pore diameter at 23.38 nm while 2wt%Cu/TiO_2 have the smallest pore diameter was 3.91 nm. In terms of desorption pore diameter, the prepared photocatalysts show the hyperbolic trend. The porous structure of the photocatalysts was consistent with density measurements. Since the pore diameters were fallen in the range between 2 to 50 nm, so all prepared catalysts can be considered as mesoporous catalysts.

Table 4-2 Pore volume and pore diameter of Cu/TiO_2

Cu/TiO_2 (wt %)	Adsorption		Desorption	
	Pore volume (cm^3/g)	Pore diameter (nm)	Pore volume (cm^3/g)	Pore diameter (nm)
2	0.0400	13.9	0.0399	13.8
5	0.0491	20.7	0.0496	19.8
10	0.0420	19.7	0.0429	17.5
15	0.0411	17.9	0.0410	17.7
20	0.0387	23.4	0.0392	19.8
25	0.0367	23.4	0.0368	13.8

4.2.2 XRF Analysis

XRF (X-ray fluorescence) is an x-ray instrument used for routine, relatively non-destructive chemical analyses of rocks, minerals, sediments and fluids. It works on wavelength-dispersive spectroscopic principles that are similar to an electron microprobe (EPMA). XRF is used to determine the actual average composition of Cu/TiO_2 in current study. The results obtained are summarized in Table 4.3.

Table 4-3 Results obtained from XRF test.

Catalyst (wt%)	TiO_2 (wt%)	Cu (wt%)
2	92.79	2.45
5	88.78	5.65
10	83.02	11.29
15	76.77	17.97
20	70.23	22.88
25	62.86	27.77

XRF analysis confirmed that the CuO content in the Cu/TiO_2 photocatalysts were near identical to the nominal loadings. The deviation which was based on copper-deposited percentage ranged from 11% to 22%. The catalyst that showed the highest deviation was 2wt%Cu/TiO_2 which has recorded 22% deviation error whilst 25wt%Cu/TiO_2 has the least deviation from the desired loading which was only 11%.

4.2.3 XRD Diffraction Pattern

The solid phase identification of Cu–TiO_2 was performed using XRD techniques**.** XRD is a non-destructive analytical technique which is widely used for the identification of structure, crystalline phases, and also sizes of crystallites of natural or synthetic materials.

Figure 4.2 shows the whole set results that obtained from 2θ =3° to 80°.According to Slamet et al. (2005), the peaks on 2θ = 25.34° and 2θ = 27.42° correspond to the main peak of anatase and rutile, respectively. It can be seen that for all copper dopping TiO_2 samples, only the characteristic peaks corresponding to P25 (TiO_2) were found which consisted of 79% anatase and 21% rutile. From the relative intensity of the anatase and rutile reflections, the anatase: rutile weight ratio in the P25 TiO_2 support was estimated to be 6:1, in good agreement with the manufacturer's specifications. CuO diffraction peak appeared near 2θ = 35.6°. Besides that, a distinguishable peak appeared near 2θ = 12.9° for all the catalysts were found except for 2wt% Cu/TiO_2. The peak intensities increased for higher copper loading; hence this peak should be copper's peak. The disapperance of this peak for 2wt%Cu/TiO_2 indicated that the deposited copper value was too low.

From Figure 4.2, the peak for CuO which was near 2θ = 35.6° can barely be seen for 2wt% and 5 wt% of Cu/TiO_2. This may be attributed to the copper content was small. Furthermore, the ionic radius of Cu^+ (0.096nm) was larger than that of Ti^{4+} (0.068 nm). It was difficult for doped copper ions to enter into the TiO_2 lattice, hence copper species only stay on the surface of TiO_2 or in the interstice of TiO_2 (Foster et al., 1995). However, small peaks were observed at near 2θ = 36.7° which can be assigned to CuO species.

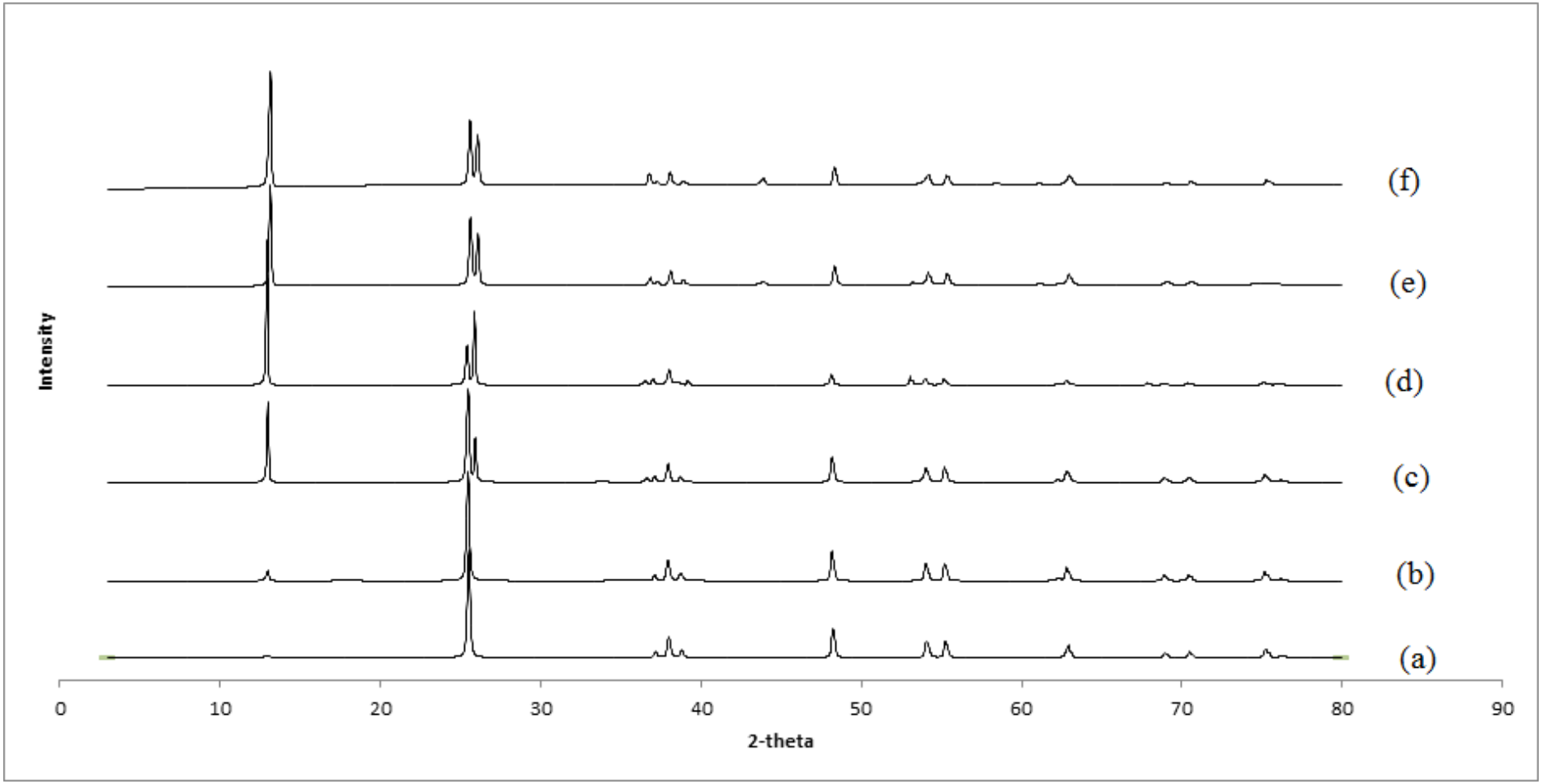

Figure 4-2 XRD patterns of copper-titinia catalysts: (a) 2wt% Cu/ TiO_2 (b) 5wt% Cu/ TiO_2 (c) 10wt% Cu/ TiO_2 (d) 15wt% Cu/ TiO_2 (e) 20wt% Cu/ TiO_2 and (f) 25wt% Cu/TiO.

As calculated from the Scherrer equation (Equation 3.10), the crystalline size of CuO were tabulated in the Table 4.4. The crystalline size of anatase was relatively uniform, ranging from 41.8 to 49.1 nm, whereas the copper clusters grew up with the increase in Cu loading.

Table 4-4 Crystalline size of CuO for each catalyst.

Wt% of Cu	Crystalline size (nm)
2	44.8
5	43.1
10	41.8
15	49.1
20	44.3
25	44.9

4.2.4 Density of Catalysts

The density of synthesized catalysts was obtained from gas pycnometer unit (Pycnometer type 1305 Micrommeritics). The results were repeated for five cycles for each catalysts and then averaged to ensure the accuracy. Table 4.5 shows a typical measurements.

Table 4-5 The density of 2wt% Cu/ TiO_2.

Cycle	Volume (cm^3)	Density (g/cm^3)
1	0.6390	2.78
2	0.6412	2.77
3	0.6436	2.76
4	0.6454	2.75
5	0.6454	2.75

From Table 4.5, the density of 2wt% Cu/ TiO_2 was calculated based on the average of five measurements which was 2.76 g/cm^3. The results for other loadings of photocatalysts are tabulated in Table 4.6.

Table 4-6 Density of Cu/TiO_2 photocatalyst

Wt%Cu/ TiO_2	**Density (g/cm^3)**
2	2.76
5	3.28
10	3.21
15	3.24
20	3.17
25	3.11

According to (William & David, 2008), density of a mixture can be calculated in terms of mass fraction as in the Equation (4.1).

$$\frac{1}{\rho_{Cu/TiO_2}} = \frac{X_{Cu}}{\rho_{Cu}} + \frac{X_{TiO_2}}{\rho_{TiO_2}} \tag{4.1}$$

where

ρ_i = density (g/cm^3)

X_i = weight fraction

The theoretical density of Cu/TiO_2 was calculated and the results from the calculation are summarized in Table 4.7.

Table 4-7 Theoretical density of Cu/TiO_2

Wt% of Cu/ TiO_2	**Weight fraction of TiO_2 (w_{TiO2})**	**Density (g/cm^3)**
2	0.98	4.37
5	0.95	4.44
10	0.90	4.56
15	0.85	4.69
20	0.80	4.82
25	0.75	4.97

The actual density and theoretical density from Tables 4.6 and 4.7 are plotted in Figure 4.3 for comparison study.

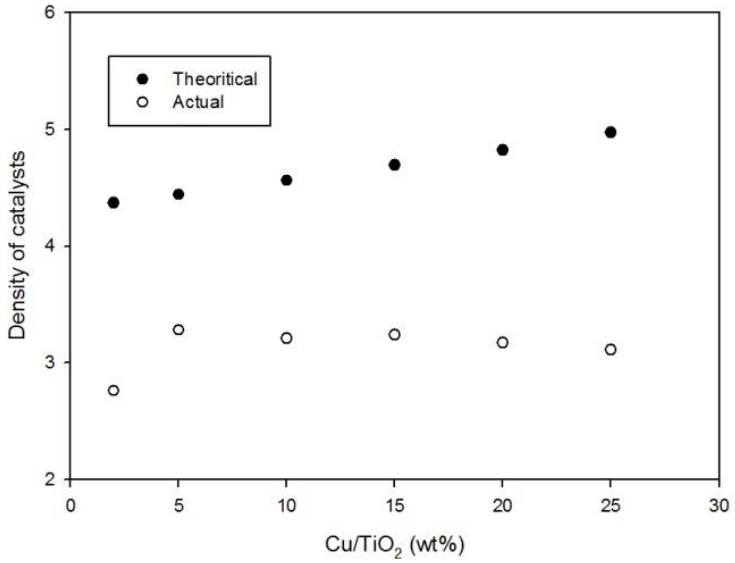

Figure 4-3 Densities of theoretical calculation and actual measurements of Cu/TiO_2.

In Figure 4.3, the theoretical density are apparently diverged from the actual measured density. In addition, both showed contrasting trend. Theoretically, the density of the catalyst should increase gradually with the increment of Cu content. The measured density has showed contrasting trend. The discrepancy might due to the porous structure of catalysts after calcination process.

4.2.5 TGA

The TGA of copper-doped on TiO_2 catalyst samples showed the weight lost pattern of the material prepared freshly by wet impregnation method (Figure 4.4). The thermogram for 20wt% Cu/TiO_2 showed the decomposition steps – from 298 until 523 K and another from 523 to 573 K. These can be attributed to moisture loss and decomposition of copper nitrate salt, $Cu(NO_3)_2$, respectively.The decomposition of copper nitrate can be represented by Equation (4.2).

$$Cu(NO_3)_2 \rightarrow CuO(s) + 2NO_2(g) + O_2(g) \qquad (4.2)$$

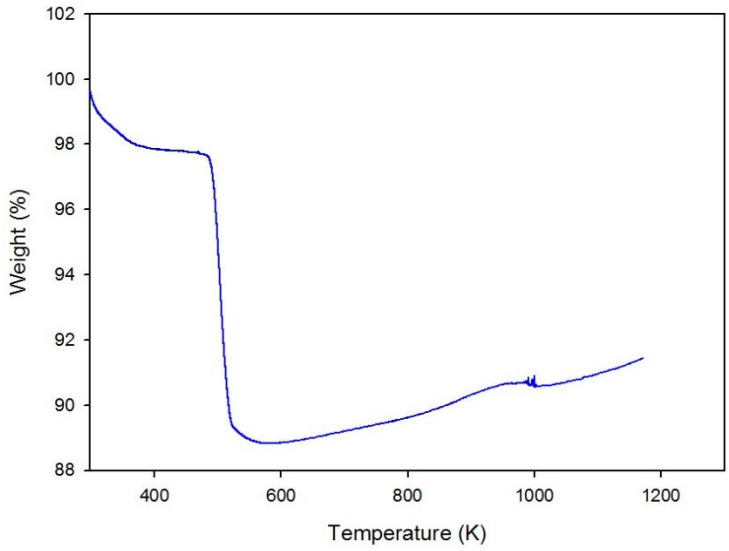

Figure 4-4 The weight loss profile of the 20wt% Cu/TiO_2.

The derivative weight profile for mass reduction from T= 450 to 550 K were amplified and plotted in Figure 4.5. No peak was observed for 2wt% Cu/TiO_2 which indicates low content of Cu; hence low copper oxide content which leads to insignificant decomposition. On the other hand, the peak for others prepared catalysts occurred within this temperature range. Significantly, the maximum peak temperatures seem to be invariant with the Cu loading. The intensity of the peaks increased with the wt% of Cu, which indicating higher content of copper nitrate present in the particular catalyst.

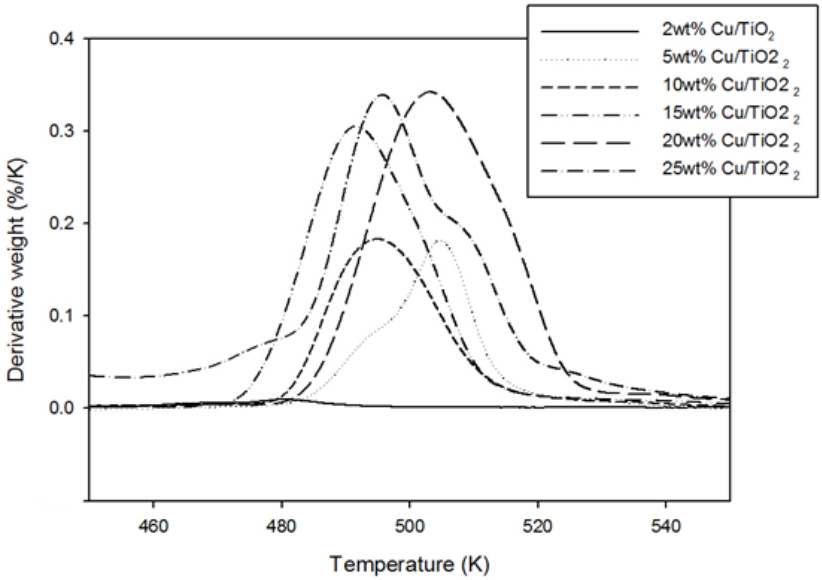

Figure 4-5 Derivative weight profile of catalysts prepared from T=450 to 550 K

4. 3 Dark Adsorption Study

Methylene blue (MB) adsorption is studied by equilibrating various concentration of the MB solution with the powder photocatalysts in the dark for time periods tranging from a few minutes (~ 30min) to several hours depending the kinetics of the adsorptiom process. The supernatant solutions was then sampled out to test the amount of MB adsorbed on the TiO2 surface.According to Rajeshwar et al,.(2008) , dark adsortion data are processed in the form of a plot of concentration adsorbed (N_{ads}) versus equilibrium concentration (C_{eq}) according to the Langmuir adsorption isotherm:

$$N_{ads} = \frac{N_s K_L C_{eq}}{1 + K_L C_{eq}} \tag{4.2}$$

In equation 4.2 , N_s is the total number of accessible adsorption sites and K_L is the adsorption constant (in M^{-1}).However , in this case the adsorption study seems no significant effect in the first hours. So, the N_{ads} is so small until insignificant that can be ignored.

4. 4 Photoreaction Study

4.4.1 Photodegradation of Methylene Blue

The photoreactivity of prepared catalysts were tested with photodegration of methyl blue. Methylene blue is a heterocyclic aromatic organic compound with the molecular formula $C_{16}H_{18}N_3SCl$. Significantly, the method to utilize MB dye solution as a standard test for photo-catalytic activity has been widely adopted and sanctioned by the International Organization for Standardization (ISO). During the sample analysis, the concentration of methylene blue solution can be obtained accurately by UV-Vis Spectrophotometer. Moreover, MB solution is most suitable as a tester among all the organic dyes for photo-activity determination due to its highly coloured nature, good chemical stability as well as inexpensive.

Prior to reaction, standard calibration curves for MB would be obtained via UV-Vis spectrophotometer. Subsequently, aqueous slurry was obtained by adding 0.25 g of photocatalyst to 300 ml MB aqueous solution at 10 ppm. Irradiation was performed with a 1000-W high pressure UV-lamp. The aqueous slurry was rigorously stirred for 30 min prior to irradiation to attain equilibrated-adsorption state. During the photoreaction, at 15 min intervals, the suspension was withdrawn and centrifuged to separate the photocatalyst particles followed by UV-Vis measurement at absorbance peak of 664 nm. The actual concentration of each sample was obtained by referring back to the calibration curve obtained in prior. Figure 4.6 shows a typical calibration curve obtained during the measurement.

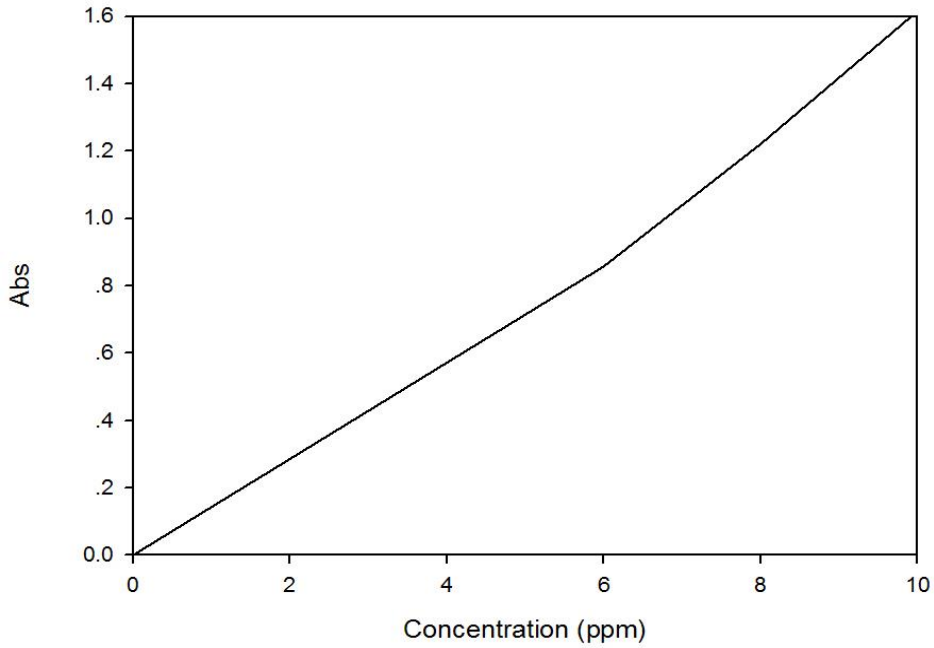

Figure 4-6 A typical calibration curve for methylene blue

The results obtained from photoreaction of methylene blue with different catalysts are shown in Table 4.8. From the results, the reactivity of the all the prepared photocatalysts are obviously showing a transient concentration reduction.

Table 4-8 The results of methylene blue after 1 h photoreaction.

Time	Conc. (ppm)					
	2wt%	5wt%	10wt%	15wt%	20wt%	25wt%
0	11.42	10.87	10.16	11.43	9.90	10.43
15	10.97	9.13	8.42	10.83	9.13	9.55
30	9.75	8.87	7.35	9.14	9.00	8.80
45	8.61	8.33	6.58	8.55	7.81	8.73
60	8.48	6.57	5.76	6.39	6.49	7.48

Since the initial concentration varied slightly for different experiment sets, the normalized transient concentration was plotted and shown in Figure 4.7 for comparison purpose. The conversion of MB photodegradation was obtained by using Equation (4.3):

$$\text{Degradation conversion, } \mathrm{X}(\%) = \frac{C_{Ao} - C_A}{C_{Ao}} \times 100 \qquad (4.3)$$

where by C_{Ao} represents concentration of MB before photoreaction begins and C_A is the concentration of MB after 1 h of photoreaction. These calculated conversions are listed in Table 4.9.

Table 4-9 The conversion of MB for various catalysts after 1 h of photoreaction.

Cu (wt%)	Conversion, X (%)
2	25.74
5	39.57
10	43.32
15	44.09
20	34.45
25	28.28

Based on the obtained result, 15wt% of Cu/TiO_2 shows the best degradation rate by decomposing 44.0% of the MB. Significantly, the efficiency has decreased in the sequence of 15, 20 and 25wt%Cu/TiO_2.

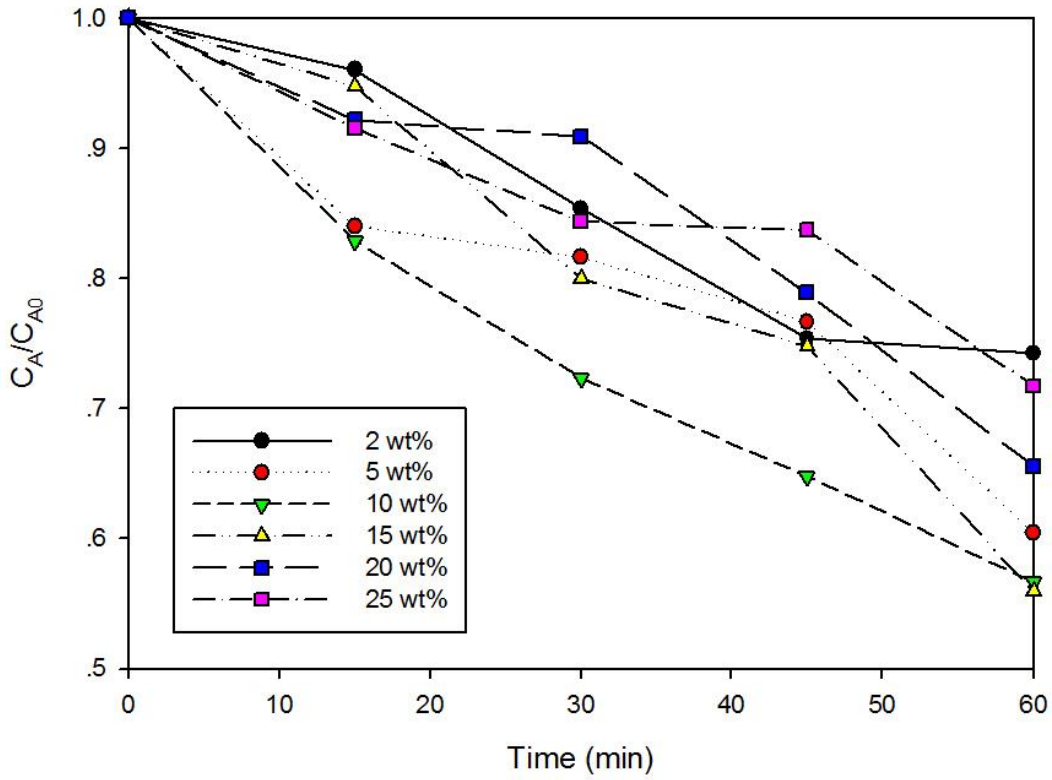

Figure 4-7 Normalized concentration for photoreaction of various Cu-loadings.

It can be observed from Figure 4.7 that the 15wt% Cu/TiO_2 was having the highest conversion (44.0%) as aforementioned. For loadings lower than 15wt%Cu, the photocatalytic activity increased with Cu deposition on TiO_2. Nonetheless, the conversion decreased at Cu content exceeding 15wt%. Most likely, since the Ti-O-Cu bond formed on the surfaceof TiO_2, metal ions are the acceptors of electrons, and they can trap the electrons in TiO_2 conduction band. Hence the electrons would have accumulate on the Cu-TiO_2 particles while the holes oxidize OH^-, H_2O, or the organics, avoiding the electron-hole recombination. As a general trend, the lower the electron-hole recombination rate, the higher the photocatalytic activity of the samples. Moreover, the electrons trapped in Cu-TiO_2 site are subsequently transferred to the surrounding adsorbed O_2. It is generally suggested that the electron transfer to oxygen might be rate-limiting step in photocatalysis. Li et al. (2004) supposed that the Cu can accelerate this step. However, excess Cu depositing on TiO_2 may have screened the photocatalyst from the UV source.

Besides that, the increase of Cu content could increase the shading effects based on XRD analysis. However, its shading effect could still be covered by its high ability to trap electrons for the below 15wt% loading. According to Slamet et al. (2005), the absorption spectra pattern of low Cu-deposited catalysts was not far different from TiO_2 and only shifted to the visible region. It can be presumed, as reported by Anpo et al. (2003) that in the current work, the implanted metal ions do not work as electron-hole recombination centers but only work to modify the electronic properties of the catalysts. The band gap of copper-loaded catalysts were smaller than TiO_2, so the photon energy needed to excite electron and hole would not be too high.

4.4.2 Langmuir-Hinshelwood Model

It is well known that photocatalytic oxidation of organic pollutants in the aqueous suspension follows Langmuir-Hinshelwood model since it is a heterogeneous system. Therefore, this kind of reaction can be represented as follows:

$$-\frac{dC}{dt} = k_r \frac{K_a C}{1 + K_a C} \tag{4.4}$$

where

$-\frac{dC}{dt}$ = degradation rate of Methylene Blue (mg L^{-1} min^{-1})

k_r = reaction rate constant (ppm min g)$^{-1}$

C = concentration of Methylene Blue solution (ppm or mg L^{-1})

K_a = adsorption coefficient of reactant

When the concentration of *C* is very small as portrayed in the current work, the product of K_aC is negligible with respect to the unity so that the Equation (4.4)

can be further simplified into a first-order kinetics and mathematically-manipulated to yield:

$$-In(\frac{C}{C_0}) = kt \tag{4.5}$$

where k is the apparent pseudo first-order reaction rate constant. Figure 4.8 shows a linear correlation between $\ln(C_o/C)$ and t for methylene blue photocatalytic degradation over various photocatalysts, and their corresponding first-order kinetics constant are shown in Table 4.10.

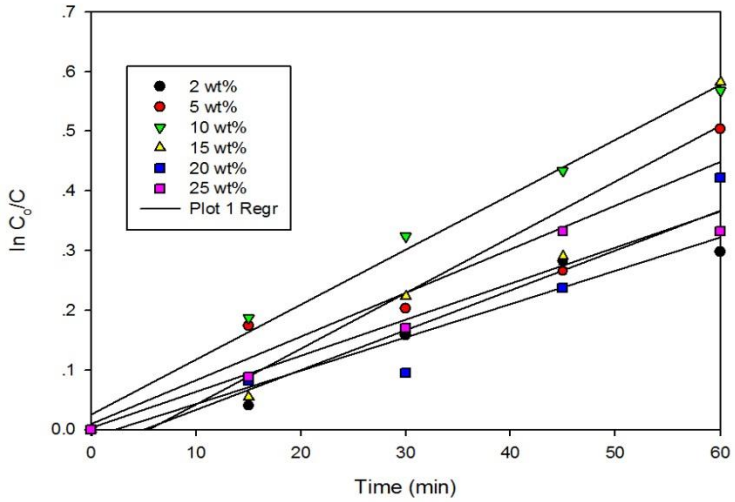

Figure 4-8 Effect of the copper-deposited amount on the photocatalytic activity of TiO_2.

Table 4-10 First-order kinetics constant of TiO_2 deposited with different Cu contents.

Cu (wt%)	**First-order kinetics constant k (min^{-1})×10^{-3}**
2	4.96
5	8.40
10	9.46
15	9.70
20	7.04
25	5.54

Based on Table 4.10, these obtained *k*-values are reasonably shows a trend with optimum at 15wt% of Cu, which is consistent with the pore diameter discussed earlier that lead to higher conversion. The *k*-values show an increasing trend with the increased copper- deposited content until the optimum value at 15wt% of copper that is 9.70×10^{-3} min^{-1}. After that, the *k*-values decreasing gradually followed by 20wt% and 25wt% of Cu/TiO_2.

The Langmuir- Hinshelwood model for MB was further proved by a rigorous error analysis. Figure 4.9 shows a parity plot between estimated value and actual value.

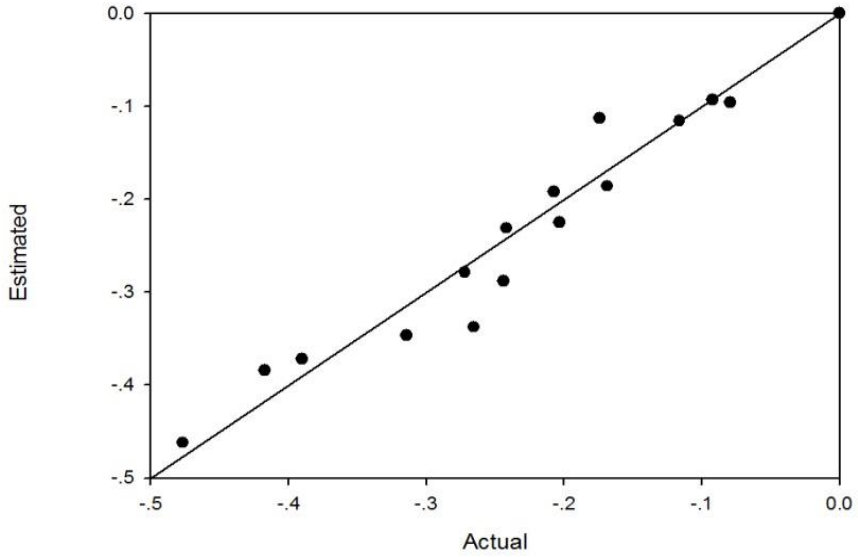

Figure 4-9 Comparison between estimated value and actual value.

Additionally, as the residual plot depicted in Figure 4.10 shows a random distribution of experimental data with no apparent skewness, it can be concluded that the first-order model can indeed adequately described the kinetic behaviour of MB photodegradation.

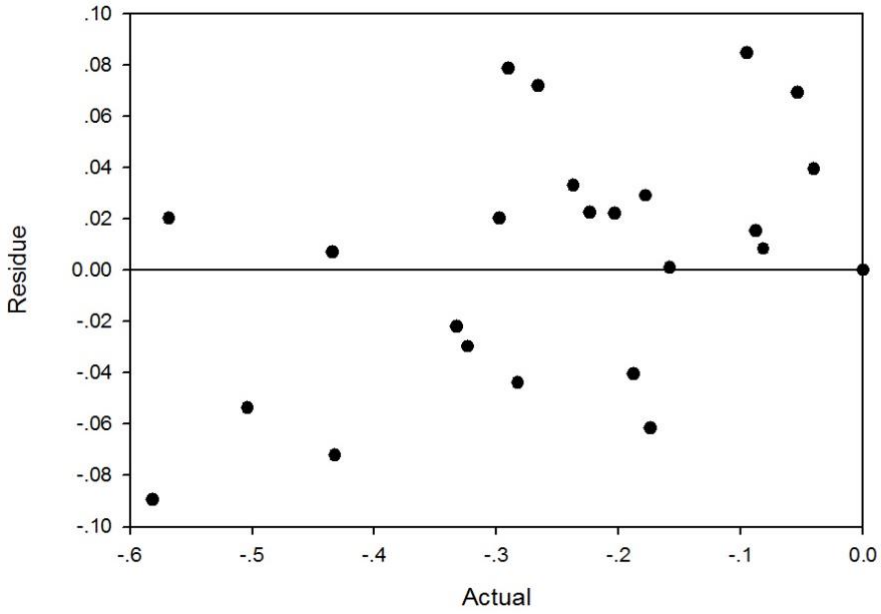

Figure 4-10 Residual plot for degradation of MB.

4.4.3 Catalyst Loading Studies

Four sets of photoreaction were conducted with catalyst loading of 0.2 g/L, 0.5 g/L, 0.83 g/L and 1.0 g/L to determine the optimum catalyst loading for MB photo-degradation.15wt% Cu/TiO2 was chosen as previously proven as the optimum performer. The outcomes of the experiments are presented in Table 4.11.

Table 4-11 Weight loading results and conversion for 15wt% Cu/TiO_2

Time (min)	15wt% Cu/TiO_2			
	0.2 g/L	0.50 g/L	0.83 g/L	1.0 g/L
0	1.0000	1.0000	1.0000	1.0000
15	0.9606	0.9120	0.9235	0.8904
30	0.8538	0.8451	0.8126	0.7858
45	0.7539	0.7620	0.7830	0.7305
60	0.7426	0.6769	0.6587	0.6209

Based on the results tabulated, the optimum catalyst loading is 1.0 g/L. About 38% of the MB was degradated within 1 h. Generally, higher catalyst loading indicates higher efficiency. The degradation efficiency of MB was in tandem with the amount of copper deposit. As a conclusion, the catalyst loading has affected the

performance of the catalyst. For 15wt% of Cu/TiO_2, the optimum catalyst loading was 1.0 g/L.

4.4.4 Concentration Effect Studies

The 15wt% Cu/TiO_2 was still chosen as the photocatalyst to perform the photoreaction of MB solution for the concentration effect studies. The photoreaction conducted with the various concentration of MB solution ranging from 10 to 30 ppm over 15wt% Cu/TiO_2. Table 4.12 shows conversion based on the concentration variation.

Table 4-12 The conversion of 15wt% Cu/TiO_2 based on different concentration.

Concentration (ppm)	Conversion, X (%)
10	34.13
15	23.28
20	25.56
25	33.17
30	23.59

As shown in Table 4.12, the conversions have generally increased when the MB concentration was increased. This result is in line with the previous work by Slamet et al. (2011). They have that reported that higher MB concentration yielded higher conversion. However, the conversion has decreased at 30 ppm MB solution. This may be attributed by the insufficient loading of photocatalyst.

4.4.5 Water Photo-splitting

As for the photoreaction of water-splitting, the production of H_2 was investigated. The set-up used is as shown in Figure 4.11.

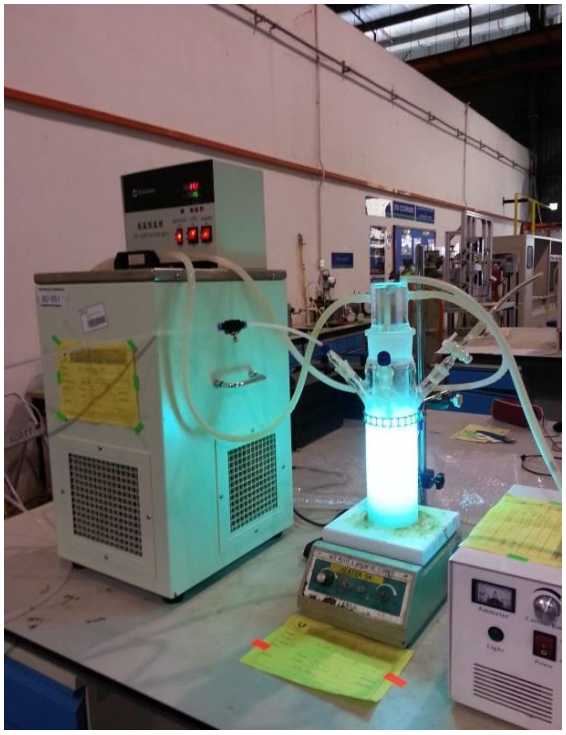

Figure 4-11 Photoreaction setup.

The photocatalytic material was evaluated for hydrogen production in 500ml a gas-closed circulation system. The temperature was maintained at 298 K via water-circulation cooling system. For each runs, 0.5 g of each photocatalysts was suspended in 500 ml of pure water. The suspended photocatalysts were bubbled with N_2 gas to de-aerate for 30 min. The effluent gas produced through photocatalytic reaction was analyzed by gas chromatography (GC) using TCD detector. The photocatalytic activity of hydrogen production from pure water as a function of the Cu content is shown in the Figure 4.12. The calculation of hydrogen evolution rates with its dependency on copper loadings are summarized in Table 4.13.

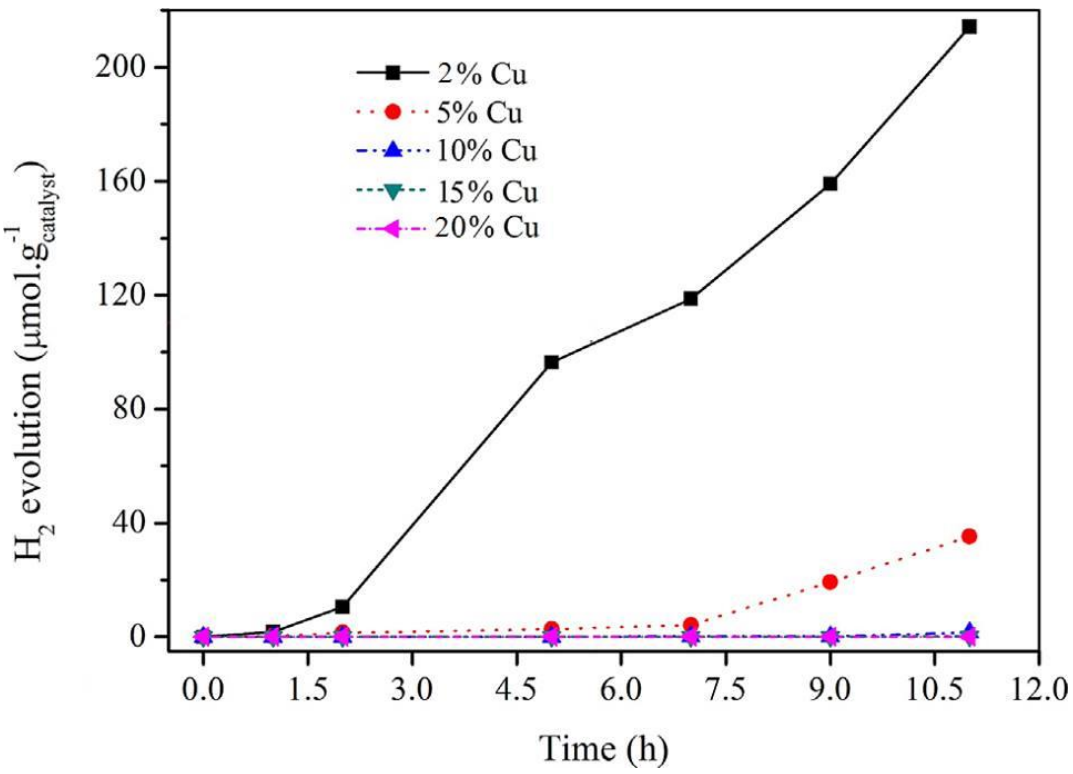

Figure 4-12 Photocatalytic hydrogen production from pure water under UV light.

Table 4-13 Hydrogen production rate of various photocatalysts.

Sample **Wt% of Cu**	***Hydrogen production rate** **(µmol $h^{-1}g^{-1}$)**
2	42.89
5	8.00
10	1.36
15	0.08
20	0.03

****Collected after 5 h of water photo-splitting***

In pure water system, the photocatalytic performance of Cu/TiO_2 photocatalysts in various copper loading revealed that hydrogen generation activity was disadvantageous of high copper loading, displaying an inferior activity as can be seen in the Figure 4.12. It can be observed that all the photocatalysts rarely generated hydrogen in the 1st h of reaction. Significantly, this delay could be due to the stabilization in the solution. Moreover, the rate of reaction progressively declined to zero at copper content of 10wt%. This phenomena is probably due to the fact that the

excess electrons in CuO could transfer to the valance band and induce electron-hole recombination in TiO_2, resulting in the suppression of hydrogen evolution rate activity. This result indicated that the optimal Cu loading on TiO_2 photocatalysts for hydrogen production from pure water splitting was 2wt%. This was due to the fact that the concentration could effectively balance an increase in trapping sites leading to longer lifetime for interfacial charge transfer (Xu et al., 2011). Other possible reason may be that the higher Cu loading has initiated the isolated CuO and CuO bulk transfer than the interface, blocking the sensitization of TiO_2.

CHAPTER 5

CONCLUSIONS AND RECOMMENDATIONS

5. 1 Conclusions

In this thesis, the roles of Cu/TiO_2 photocatalysts in the of methylene Blue photodecomposition and water photo-splitting were studied. From the liquid N_2 physisorption analysis, the catalysts were found to be porous, which is consistent with the discrepancy in the density comparison. The BET specific surface area of these photocatalysts generally decreased with the increased Cu loading due to formation of CuO crystallite that has blocked pores of TiO_2 support. Moreover, BJH cumulative pore volumes and BJH average pore diameters for all Cu/TiO_2 samples were in the range 0.0367 to 0.0400 cm^3g^{-1} and 13.9 to 23.4 nm respectively. All the prepared catalysts can be considered as mesoporous catalysts since the pore diameters were in the range of 2 to 50 nm. Following the XRF analysis, it can be concluded that the CuO content in the Cu/TiO_2 photocatalysts were near identical to the nominal loadings with mild deviation from 11 to 22%. In terms of crystallography study, peaks synonymous with CuO species were recorded at 2θ =35.6° for all Cu/TiO_2 with exception to 2 and 5wt%Cu/TiO_2. Besides that, Cu species was discovered at 2θ = 12.9° except for 2wt% Cu/TiO_2 which indicated that the content of copper was probably insignificant. Gas pycnometer measurements gave actual density of synthesized catalysts that ranged from 2.76 to 3.28g/cm^3, which were much lower

than theoretical density calculations (4.37 to 4.97 g/cm^3). This can be attributed to the porous structure of the catalyst. From TGA analysis obtained from temperature-programmed calcination, a peak was observed at around 500 K for all the catalysts except 2wt% of Cu/TiO_2. The observed peak represents the thermal decomposition of copper nitrate to CuO. Significantly, for 2wt% Cu/TiO_2, the aforementioned decomposition may not be visible from the non-isothermal heating probably due to the low copper nitrate composition. This was also consistent with XRD's findings.

The Cu/TiO_2-assisted photodegradation of 10 ppm aqueous Methylene Blue (MB) solution, a common industrial dye organic contaminant, was examined at 0.83 g/L catalyst loading. The photoreaction was carried out under 1000-watt UV irridiation for 1 h. UV-VIS spectrophotometer was employed to measure the transient MB concentration. Based on the screening results, 15wt% Cu/TiO_2 photocatalyst yielded the highest conversion at 44%. Significantly, the decomposition of MB solution was found to follow a first-order kinetics derivable from Langmuir-Hinshelwood model. Moreover, 15wt% Cu/TiO_2 also possessed the highest specific reaction constant at 0.009690 min^{-1}. Significantly, the obtained results can be explained by Ti-O-Cu bond formed on the surface of TiO_2, metal ions are the acceptors of electrons, and they can trap the electrons in TiO_2 conduction band. Hence the electrons do accumulate on the Cu-TiO_2 particles while the holes oxidize OH^-, H_2O, or the organics, avoiding the electron-hole recombination

Besides that, the catalyst loading studies were also determined by running photoreaction with different loadings of 15wt%Cu/TiO_2. An optimum point was discovered at 1.0 g/L of MB. As a conclusion, higher catalyst loading yielded higher conversion. Subsequently, the concentration effect studies were conducted. the conversion increased as the MB concentration increased from 15 to 25 ppm. This results may be attributed by higher concentration yield higher conversion.

In addition, water photo-splitting for the production of H_2 was also investigated over the same types of catalyst. The photocatalytic performance of Cu/TiO_2 photocatalyst in various copper loadings has revealed that hydrogen generation activity was disadvantageous of high copper loading as it displayed an inferior activity.

As a conclusion, the current research has shown that the role of Cu/TiO_2 plays the different role in the methylene blue decomposing and water photo-catalytic. It shows that photocatalysts will have different effect for different photoreaction studies

5. 2 Recommendations

Based on the findings and observations of this research projects, the following suggestions are proposed for future studies. Firstly, during photocatalysts preparation, suitable methods and parameters must be employed to inprove the reactivity of catalysts. For current study, the catalysts were prepared by using wet impregnation method and air-calcined at 673 K for 30 min. Further study may be required to find the suitable methods and paramenters for better catalysts. Moreover, the photocatalysts should be sieved to maintain the particle size once after calcined. Besides, the operating temperature has to be maintained throughout the experiment for more accurate results. UV light will emit high amount of heat energy causing the operating temperature to increase with irradiation time. Proper cooling steps must be taken to maintain the temperature. In addition, the results for each samples should be repeated to ensure accuracy during the analysis of UV-Vis. Finally, the experiments for water photo-splitting for the production of H_2 gas should be directly connected to gas chromatography for analysis since the production of H_2 is too small.

REFERENCES

Abe R., Higashi M., Sayama K., Abe Y. and Sugihara H. (2006). *J. Phys. Chem. B,* 110, 2219.

Al-Rasheed, R. A. (2005). Water treatment by heterogeneous photocatalysis an overview. Saudi Arabia: Saline Water Desalination Research Institute.

Anderson, J.R. & Pratt, K.C.(1985). *Introduction to characterization and testing of catalyst.* Sydney: Academic Press.

Augustynski (1993). *J. Electrochim. Acta*. 38, 43.

Azaroff, L.V. (1968). *Elements of x-Ray crystallography*. New York: McGraw Hill Book Company.

Barbara. L.D. & Christine. M.C. (2012). X-ray powder dirraction (XRD).

Barrett, E.P., Joyner, L.G., & Halenda, P.P. (1951). The determination of pore volume and area distributions in porous substances. I. Computations from nitrogen isotherms. *J Amer Chem Soc*, 73, 373-380.

Bergeret, G. & Gallezot, P. (1997). Particle size and dispersion measurements, In: Ertl,G., nőzinger, H. & Weitkamp, J(Eds.). *Handbook of Heterogeneous Catalysis*. Weinheim.

Bergeret, G. & Gallezot, P. (1973). *Particle size and dispersion measurements*, in *Handbook of heterogeneous catalysis*. VCH Verlagsgesellschaft mbH: Weinheim.

Beck, D. D.; White, J. M, J. *Phys, Chem*, 1984, 88,174.

Beck, D. D.; White, J.M.; Ratcliffe, C. T. *J. Phys. Chem.* 1986,90, 3132.

Brunauer, S., Emmett, P.H., & Teller E. (1938). Adsorption of gases in multimolecularlayers. *J Amer Chem Soc*, 60, 309-319.

Bustillo, F. J.; Roman, E.; de Segovia, J.L. *Vacuum* 1989, 39, 659; 1990, 41, 19.

Castellote M. and Bengtsson N. (2011). Chapter 2: Principles of TiO_2 Photocatalysis. *Application of Titanium Dioxide Photocatalysis to Construction Materials.* (Eds.) Y. Ohama and D. Van Gemert. XII, 48 p. 28 illus., Hardcover, Springer. ISBN: 978-94-007-1296-6.

Ceram Research Limited. (2000). Titanium Dioxide - Titania (TiO_2). Retrieved from http://www.azom.com/properties.aspx?ArticleID=1179 on 5th March 2013.

Chen, X. & Mao, S.S. 92007). Titanium dioxide nanomaterials: synthesis, properties, modifications,and applications, *Chem. Rev.,* 107, 2891–2959.

Cullity, B.D. (2001). *Elements of x-ray diffraction.* London: Prentice-Hall International.

D. Brown, A. mark, S.DC. De Vito , Crit. Rev. Environ. Technol. 23 (1993) 249.

De_Boer, J.H., Lippens, B. C., Linsen, B. G., Broekhoff, J. C. P., van den Heuvel, A.,& Osinga, Th J. (1966). Thet-curve of multimolecular N2-adsorption. *J Colloid Interf Sci*, 21(4), 405-414.

Dholam R., Patel N. & Miotello A. (2011). *Int. J. Hydrogen Energy,* 36, 6519.

Dollimore, D., & Heal, G.R. (1964). An improved method for the calculation of pore-size distribution from adsorption data. *J Appl Chem*, 14, 109-114.

Domen K., Kudo A., Shinozaki A., Tanaka A., Maruya K. and Onishi T. (1986). *J. Chem.* Soc., *Chem. Commun*., 356.

Duonghong, D.; Borgarello, E. and Gratzel, M. (1981). *J. Am. Chem. Soc.*, 103, 4685.

Edward. Y.H.K. (1969). Air and helium pycnometer. *Powder Technol*(3), 3, 179-180.

Fujishima A. & Honda K. (1972). *Nature,* 238, 37.

Gopel, W.; Rocker, G.; Feierabend, R. *Phys, Rev*. B 1983, 28,3427.

Gregg, S.J., and Sing, K. S. W. (1982). *Adsorption, Surface Area, and Porosity*. 2 nd ed. London: Academic Press.

H. Zollinger, Colour Chemistry, VCH, Weinheim, 1991.

Henrich, V. E.; Dresselhaus, G.; Aeiger, H. J. *Solid State Commun*. 1977,24,623

Hernández-Alonso, M. D., Hungría, A. B., Martínez-Arias, A., Fernández-García, M., Coronado, J.M., Conesa, J. C., & Soria, J. (2004). EPR study of the photoassisted formation of radicals on CeO_2 nanoparticles employed for toluene photooxidation. *Appl Catal B-Environ*, 50(3), 167-175.

Ho G.W., Chua K.J. & Siow D.R. (2011). *Chem. Eng. J.*, 181–182, 661.

Hu, K.S., Xiao, X., Cao, X.F., Hao, R., Zuo, X.X., Zhang, X.J. & Nan, J.M. (2011). Adsorptive separation and photocatalytic degradation of methylene blue dye on titanate nanotube powders prepared by hydrothermal process using metal Ti particles as a precursor, *J. Hazard. Mater*, 192, 514-520.

Hugenschmidt, M . B.' Gamble, L.; Campbell, C. T. *Surf. Sci.* 1994,302,329.

Iwaki, T. *J. Chem. Soc., Faraday Trans.* 1 1983,79, 137.

Iwase A., Kato H. and Kudo A. (2006). *Catal. Lett,* 108, 7.

J. Li, L. Liu, Y. Yu, Y. Tang, H. Li, F.Du, Electrochem. Commun. 6(2004) 940-943

Jaeger, C.D. and Bard, A.J. (1979). *J. Phys. Chem. Soc.*, 99, 1789.

James. M. (2012). Overview of X-ray fluorescence.

Jenkins. R., Gould. R.W., & Gedeke. D. (2000). Application of X-ray spectrometry. *Appl Spectrosc Rev*, 35(1&2), 129-150.

K. Rajeshwar. J. Ibanez. Environmental Electrochemistry,Academic Press. San Diego, 1997.

K. Sopajaree, .A. Qasim, S.Basak, K.Rajeshwar,J. Appl. Electrochem. 29 (1999) 533.

Kato H. and Kudo A. (2003). *Catal. Today*, 78, 561.

Kato H., Asakura K. and Kudo A. (2003). *J. Am. Chem. Soc.,* 125, 3082.

Kato H. and Kudo A. (1999*). Chem. Lett.,* 28, 1207.

Kim H.G., Hwang D.W., Kim J., Kim Y.G. and Lee J.S. (1999). *Chem. Commun.*, 1077.

Kim J., Hwang D.W., Kim H.G., Bae S.W., Lee J.S., Li W. and Oh S.W. (2005). *Top. Catal*., 35, 295.

Kudo A., Kato H. and Nakagawa S. (2000). *J. Phys. Chem. B,* 104, 571.

Kudo A. and Misaki Y. (2008). Heterogeneous photocatalyst materials for water splitting. *The Chemical Society Reviews: 2009 Renewable Energy Issue,* 38, 252.

Kurtz, R. L .; Stockbauer, R.: Madey, T. E.; Roman, E.; de Segovia, J. L. *Surf Sci*. 1989,218,178.

Langmuir, I. (1916). The constitution and fundamental properties of solids and liquids. *J Amer Chem Soc*, 38, 2221-2267.

Liao C.H., Huang C.W. and Wu J.C.S. (2012). *Catalysts,* 2, 490.

Liao, S., Donggen, H., Yu, D., Su., & Yuan, G. (2004). Preparation and characterization of ZnO/TiO_2, $SO_4^{2-}/ZnO/TiO_2$photocatalyst and their photocatalysis. *J Photoch Photobio A*, 168(1-2), 7-13.

Liebhiafsky, H.A., Peiffer, H.G.,Winslow, E.H., & Zemany, P.D. (1972). *X-ray electrons and analytical chemistry*. New York: Wiley-Interscience, John Wiley & Sons Inc. Slamet

Liu G., Zhao L., Ma L. and Guo L. (2008). *Catal. Commun.*, 9, 126.

Liu, W., Zeng, F., Jiang, H., Zhang, X., & Li, W. (2012). Composite Fe_2O_3 and ZrO_2/Al_2O_3 photocatalyst: Preparation, characterization, and studies on the photocatalytic activity and chemical stability. *Chem Eng J*, 180, 9-18.

Lo, W. J.; Chng, Y. W.: Somorjai, G. A. *Surf. Sci*. 1978, 71, 199.

Lu, G.; Linsebigler, A.; Yates, J.T., Jr. *J. Phys. Chem*. 1994, 88, 11733

Lu, G.; Linsebigler, A.; Yates, J. T. Jr. *J. Chem. Phys.* 1995, 102, 3005.

M. Anpo, M. Takeuchi, J. Catal. 216 (2003) 505

Melo. M.O., & Silva. L.A. (2011). Visible light-induced hydrogen production from glycerol aqueous solution on hybrid Pt-Cds-TiO_2 photocatalysts. *J Photoch PhotobioA*, 226, 36-41.

Meng, Z. & Juan, Z. (2008).Wastewater treatment by photocatalytic oxidation of Nano-ZnO. *Global Environmental Policy in Japan*, 12, 1-9.

Michler, G.H. (2004). *Electron microscopy of polymers.* Berlin Heidelberg: Springer.

Midilli, A.Ay, M.Dincer, I. Rosen, M.A. (2005). *Renew. Sustain. Energy Rev. 2005*, 9, 255.

Miseki Y., Kato H. and Kudo A. (2005). *Chem. Lett.*, 34, 54.

Miseki Y., Kato H. and Kudo A. (2006). *Chem. Lett.*, 35, 1052.

Pan, J, M.; Maschhoff, B.L,; Diebold, U.: Madey, T. E. J. *Vac. Sci. Technol*. A 1992, 10, 2470

Qian, J., Chen, F., Wang, F., Zhao, X., & Chen, Z. (2012). Daylight photocatalysis performance of biomorphic CeO_2 hollow fibers prepared with lens cleaning paper as biotemplate. *Mater Res Bull*, 47(8), 1845-1848.

Rouquerol, J., Rouquerol, F., Llewellyn, P., Maurin, G., & Sing, K. S. W. (2013). Adsorption by Powders and Porous Solids:Principles, Methodology and Applications. UK: Academic Press.

Reddy V.R., Hwang D.W. and Lee J.S. (2003). *Catal. Lett.*, 90, 39.

Sayama K., Arakawa H. and Domen K. (1996). *Catal. Today*, 28, 175.

Sato, S.; White, J. M. *J, Am. Chem, Soc*, 1980, 102, 7206; *J. Phys. Chem*. 1981, 85, 592

Shackley. M.S. (n.d.). An introduction to X-ray fluorescence: Analysis in archaeology.

Sing, K S. W., Everett, D. H., Haul, R. A. W., Moscou, L., Pierotti, R. A., Rouquerol, J., and Siemieniewska, T. (1985). Reporting Physisorption Data for Gas Solid Systems with Special Reference to the Determination of Surface-Area and Porosity (Recommendations 1984). *Pure Appl Chem*, 57(4), 603-619.

Sing, K. S. W. & Rouquerol, J. (1997). *Surface Area and Porosity*, in *Handbook of*

heterogeneous catalysis, VCH Verlagsgesellschaft mbH: Weinheim.

Slamet, Anny., & Stiadi. (2011). Photocatalytic hydrogen generation from glycerol and water using Ptloaded N-doped TiO_2 Nanotube, *International Journal of Engineering & Technology,* 11(3), 91-95.

Slamet, H.W.Nasution, E. Purama, S.Kosela, J. Gulazuardi, Catal. Commun. 6 (2005) 313.

Slamet, Nasution, H. W., Purnama, E., Kosela, S., & Gunlazuardi, J. (2006). Photocatalytic reduction of CO2 on copper-doped Titania catalysts prepared by improved-impregnation method. *Catalysis Communications*, 6, 313-319.

Solomon S., Plattner, G.K., Knutti, R., Friedlingstein, P. (2009). *Proc. Natl. Acad. Sc. USA*, 106, 1704.

Takata T., Furumi Y., Shinohara K., Tanaka A., Hara M., Kondo J.N. and Domen K. (1997). *Chem. Mater.*, 9, 1063.

Tamari. S. & Aguilar. C.A. (2004). Optimum design of gas pycnometer for determining the volume of solid particles, Proceedings, CENAM Symposium, Centre for Metrology of Mexico

Tang. Y.C., Huang. X.H., Yu. H.Q., & Tang. L.H. (2012). Nitrogen-doped TiO_2 photocatalyst prepared by mechanochemical method: Doping mechanisms and visible photoactiviity of pollutant degration. *Int J Photoenergy*, 2012, 1-10.

Tian, L., Zhao, Y., He, S., Wei, M., & Duan, X. (2012). Immobilized Cu–Cr layered double hydroxide films with visible-light responsive photocatalysis for organic pollutants. *Chem Eng J*, 184, 261-267.

William. D.C., & David. G.R. (2008). Fundamentals of materials science and engineering: An intergrated approach.

Xia, H., Zhuang, H., Zhang, T., & Xiao, D. (2008). Visible-light-activated nanocomposite photocatalyst of Fe_2O_3/SnO_2. *Mater Lett,* 62(6-7), 1126-1128.

Xu, S., Ng, J., Du, A.J., Liu, J. & Sun, D.D. (2011). Highly efficient TiO_2 nanotube photocatalyst for simultaneous hydrogen production and copper removal from water. *Int J Hydrogen Energy,* 36:6538e45.

Yamaguti K. and Sato S. (1985). *J. Chem. Soc*., *Faraday Trans*. 1, 81, 1237.

Yanagisawa, Y.; Ota, Y, *Surf. Sci. Lett.* 1991, 254, L433.

Yang H., Chen Y. and Guo L. (2010). *Catal Commun.*, 11, 1099.

Yao W. and Ye J. (2007). *Chem. Phys. Lett.*, 435, 96.

Yoong. L.S., Chong. F.K., & Dutta. B.K. (2009). Development of copper-doped TiO_2 photocatalyst for hydrogen production under visible light. *Energy*, 34, 1652-1661.

Zhang, Q., Cheng, X., Zheng, C., Feng, X., Qiu, G., Tan, W., & Liu, F. (2011). Roles of manganese oxides in degradation of phenol under UV-Vis irradiation: Adsorption, oxidation, and photocatalysis. *J. Environ. Sci.,* 23(11), 1904-1910.

Zhang, X. & Lei, L. (2008). Preparation of photocatalytic Fe_2O_3–TiO_2 coatings in one step by metal organic chemical vapor deposition. *Appl Surf Sci*, 254(8), 2406-2412.

Zschack (1991). *In the Structure of Surfaces III.* Tong, S.Y.; Van Hove, M.A.; Takayanagi, K. and Xie, X.D., Eds.; Springer Series In Surface Science, Vol. 24; Springer-Verlag Berlin: Heidelberg, p. 646.

APPENDICES

Appendix A

Wet Impregnation Method

The calculation of mass of $Cu(NO_3)_2.3H_2O$ needed:

2 wt% Cu/TiO_2 preparation calculation:	
Molecular weight of Cu	63.5
Molecular weight of $Cu(NO_3)_2.3H_2O$	241.5
Photocatalyst produced	40 g
Mass of Cu	$40 \times 0.02 = 0.8\text{g}$
Mass of $Cu(NO_3)_2.3H_2O$	$\frac{241.5}{63.5} \times 0.8 = 3.0438\text{g}$

Photocatalyst preparation:

Cu/TiO_2 (wt%)	$Cu(NO_3)_2.3H_2O$ (g)
2	3.0438
5	7.6063
10	15.2126
15	22.8189
20	30.4252
25	38.0315

Appendix B

Gas pycnometer

Gas pycnometer: 2 wt% Cu/TiO_2

Combined Report

Summary Report

Sample Volume
Average: 0.6429 cm³
Standard Deviation: 0.0025 cm³

Sample Density
Average: 2.7646 g/cm³
Standard Deviation: 0.0107 g/cm³

Tabular 1

Cycle#	P1 Pressure (psig)	P2 Pressure (psig)	Volume (cm³)	Density (g/cm³)	Total Pore Volume (cm³/g)
1	19.527	10.704	0.6390	2.7816	0.6405
2	19.528	10.703	0.6412	2.7718	0.6392
3	19.521	10.699	0.6436	2.7617	0.6379
4	19.517	10.696	0.6454	2.7541	0.6369
5	19.528	10.702	0.6454	2.7538	0.6369

Summary Data	Average	Standard Deviation
Volume:	0.6429 cm³	0.0025 cm³
Density:	2.7646 g/cm³	0.0107 g/cm³

6202- Total solids concentration is invalid; liquid density is greater-than or equal to solids density.

Gas pycnometer: 5 wt% Cu/TiO_2

Combined Report

Summary Report

Sample Volume
Average: 1.2330 cm³
Standard Deviation: 0.0007 cm³

Sample Density
Average: 3.2899 g/cm³
Standard Deviation: 0.0020 g/cm³

Tabular 1

Cycle#	P1 Pressure (psig)	P2 Pressure (psig)	Volume (cm³)	Density (g/cm³)	Total Pore Volume (cm³/g)
1	19.540	10.443	1.2339	3.2876	0.6958
2	19.562	10.455	1.2323	3.2919	0.6962
3	19.540	10.444	1.2322	3.2921	0.6962
4	19.544	10.445	1.2329	3.2903	0.6961
5	19.549	10.448	1.2338	3.2877	0.6958

Summary Data	Average	Standard Deviation
Volume:	1.2330 cm³	0.0007 cm³
Density:	3.2899 g/cm³	0.0020 g/cm³

6202- Total solids concentration is invalid; liquid density is greater-than or equal to solids density.

Gas pycnometer: 10 wt% Cu/TiO_2

Combined Report

Summary Report

Sample Volume
Average: 1.2884 cm³
Standard Deviation: 0.0004 cm³

Sample Density
Average: 3.2105 g/cm³
Standard Deviation: 0.0010 g/cm³

Tabular 1

Cycle#	P1 Pressure (psig)	P2 Pressure (psig)	Volume (cm³)	Density (g/cm³)	Total Pore Volume (cm³/g)
1	19.563	10.430	1.2877	3.2121	0.6887
2	19.558	10.427	1.2886	3.2099	0.6885
3	19.542	10.419	1.2881	3.2111	0.6886
4	19.545	10.420	1.2886	3.2100	0.6885
5	19.552	10.424	1.2888	3.2094	0.6884

Summary Data	Average	Standard Deviation
Volume:	1.2884 cm³	0.0004 cm³
Density:	3.2105 g/cm³	0.0010 g/cm³

6202- Total solids concentration is invalid; liquid density is greater-than or equal to solids density.

Gas pycnometer: 15 wt% Cu/TiO_2

Combined Report

Summary Report

Sample Volume
Average: 1.4709 cm³
Standard Deviation: 0.0013 cm³

Sample Density
Average: 3.2455 g/cm³
Standard Deviation: 0.0028 g/cm³

Tabular 1

Cycle#	P1 Pressure (psig)	P2 Pressure (psig)	Volume (cm³)	Density (g/cm³)	Total Pore Volume (cm³/g)
1	19.554	10.339	1.4702	3.2469	0.6920
2	19.569	10.347	1.4700	3.2474	0.6921
3	19.549	10.337	1.4707	3.2457	0.6919
4	19.569	10.347	1.4700	3.2472	0.6920
5	19.566	10.344	1.4733	3.2400	0.6914

Summary Data	Average	Standard Deviation
Volume:	1.4709 cm³	0.0013 cm³
Density:	3.2455 g/cm³	0.0028 g/cm³

6202- Total solids concentration is invalid; liquid density is greater-than or equal to solids density.

Gas pycnometer: 20 wt% Cu/TiO_2

Combined Report

Summary Report

Sample Volume
Average: 1.5339 cm³
Standard Deviation: 0.0005 cm³

Sample Density
Average: 3.1703 g/cm³
Standard Deviation: 0.0011 g/cm³

Tabular 1

Cycle#	P1 Pressure (psig)	P2 Pressure (psig)	Volume (cm³)	Density (g/cm³)	Total Pore Volume (cm³/g)
1	19.565	10.315	1.5336	3.1711	0.6846
2	19.545	10.304	1.5348	3.1686	0.6844
3	19.541	10.302	1.5334	3.1715	0.6847
4	19.549	10.306	1.5342	3.1698	0.6845
5	19.564	10.314	1.5337	3.1709	0.6846

Summary Data	Average	Standard Deviation
Volume:	1.5339 cm³	0.0005 cm³
Density:	3.1703 g/cm³	0.0011 g/cm³

6202- Total solids concentration is invalid; liquid density is greater-than or equal to solids density.

Gas pycnometer: 25 wt% Cu/TiO_2

Combined Report

Summary Report

Sample Volume
Average: 1.6891 cm³
Standard Deviation: 0.0004 cm³

Sample Density
Average: 3.1129 g/cm³
Standard Deviation: 0.0008 g/cm³

Tabular 1

Cycle#	P1 Pressure (psig)	P2 Pressure (psig)	Volume (cm³)	Density (g/cm³)	Total Pore Volume (cm³/g)
1	19.545	10.229	1.6892	3.1127	0.6787
2	19.552	10.233	1.6897	3.1119	0.6787
3	19.560	10.237	1.6890	3.1132	0.6788
4	19.558	10.236	1.6884	3.1143	0.6789
5	19.549	10.231	1.6894	3.1123	0.6787

Summary Data	Average	Standard Deviation
Volume:	1.6891 cm³	0.0004 cm³
Density:	3.1129 g/cm³	0.0008 g/cm³

6202- Total solids concentration is invalid; liquid density is greater-than or equal to solids density.

X-ray Fluorescence (XRF)

CENLAB/F/007

Universiti Malaysia PAHANG

CENTRAL LABORATORY
Universiti Malaysia Pahang, Lebuhraya Tun Razak,
26300 Kuantan, Pahang Darul Makmur.
Tel: 09-5493344/8097 Fax: 09-5493353
E-mail: ucl@ump.edu.my

CERTIFICATE OF ANALYSIS (COA)

To :	ANG CHUN HOW	Attn :	
Address :	FKKSA, UMP		
c.c. :		Page :	5 pages
Fax No :	Tel No : 016-5901865		Sample Lab No: 2013/228

Sample description : Six samples in powdered form

Sample marking : Cu/TiO2

Date of sample received : 09/05/2013

Date reported : 13/05/2013

RESULTS:

Sample 1: 2wt %

No	Parameter	Results	Unit	Test Method
1.	Titanium Oxide (TiO2)	92.79	%	Quantexpress (Best Detection)
2.	Copper Oxide (CuO)	2.45	%	Quantexpress (Best Detection)
3.	Phosphorus Pentoxide (P2O5)	0.43	%	Quantexpress (Best Detection)
4.	Silicon Dioxide (SiO2)	0.25	%	Quantexpress (Best Detection)
5.	Aluminium Oxide (Al2O3)	0.20	%	Quantexpress (Best Detection)
6.	Potassium Oxide (K2O)	0.06	%	Quantexpress (Best Detection)
7.	Neobium Oxide (Nb2O5)	0.03	%	Quantexpress (Best Detection)
8.	Sulphur Trioxide (SO3)	0.03	%	Quantexpress (Best Detection)
9.	Zirconium Oxide (ZrO2)	0.02	%	Quantexpress (Best Detection)
10.	Iron Oxide (Fe2O3)	0.01	%	Quantexpress (Best Detection)

11.	Calcium Oxide (CaO)	95	ppm	Quantexpress (Best Detection)
12.	Nickel Oxide (NiO)	35	ppm	Quantexpress (Best Detection)

Sample 2: 5wt %

No	Parameter	Results	Unit	Test Method
1.	Titanium Oxide (TiO2)	88.78	%	Quantexpress (Best Detection)
2.	Copper Oxide (CuO)	5.65	%	Quantexpress (Best Detection)
3.	Phosphorus Pentoxide (P2O5)	0.44	%	Quantexpress (Best Detection)
4.	Silicon Dioxide (SiO2)	0.24	%	Quantexpress (Best Detection)
5.	Aluminium Oxide (Al2O3)	0.21	%	Quantexpress (Best Detection)
6.	Potassium Oxide (K2O)	0.05	%	Quantexpress (Best Detection)
7.	Neobium Oxide (Nb2O5)	0.03	%	Quantexpress (Best Detection)
8.	Sulphur Trioxide (SO3)	0.02	%	Quantexpress (Best Detection)
9.	Zirconium Oxide (ZrO2)	0.02	%	Quantexpress (Best Detection)
10.	Chlorine (Cl)	0.01	%	Quantexpress (Best Detection)
11.	Calcium Oxide (CaO)	93	ppm	Quantexpress (Best Detection)
12.	Iron Oxide (Fe2O3)	77	ppm	Quantexpress (Best Detection)
13.	Zinc Oxide (ZnO)	72	ppm	Quantexpress (Best Detection)
14.	Nickel Oxide (NiO)	38	ppm	Quantexpress (Best Detection)

Sample 3: 10wt %

No	Parameter	Results	Unit	Test Method
1.	Titanium Oxide (TiO2)	83.02	%	Quantexpress (Best Detection)
2.	Copper Oxide (CuO)	11.29	%	Quantexpress (Best Detection)
3.	Phosphorus Pentoxide (P2O5)	0.39	%	Quantexpress (Best Detection)

4.	Silicon Dioxide (SiO2)	0.21	%	Quantexpress (Best Detection)
5.	Aluminium Oxide (Al2O3)	0.20	%	Quantexpress (Best Detection)
6.	Potassium Oxide (K2O)	0.05	%	Quantexpress (Best Detection)
7.	Neobium Oxide (Nb2O5)	0.03	%	Quantexpress (Best Detection)
8.	Sulphur Trioxide (SO3)	0.02	%	Quantexpress (Best Detection)
9.	Zirconium Oxide (ZrO2)	0.01	%	Quantexpress (Best Detection)
10.	Chlorine (Cl)	0.01	%	Quantexpress (Best Detection)
11.	Iron Oxide (Fe2O3)	0.01	%	Quantexpress (Best Detection)
12.	Calcium Oxide (CaO)	85	ppm	Quantexpress (Best Detection)
13.	Nickel Oxide (NiO)	45	ppm	Quantexpress (Best Detection)
14.	Molibdenum Trioxide (MoO3)	33	ppm	Quantexpress (Best Detection)
15.	Hafnium Oxide (HfO2)	14	ppm	Quantexpress (Best Detection)

Sample 4: 15wt %

No	Parameter	Results	Unit	Test Method
1.	Titanium Oxide (TiO2)	76.77	%	Quantexpress (Best Detection)
2.	Copper Oxide (CuO)	17.97	%	Quantexpress (Best Detection)
3.	Phosphorus Pentoxide (P2O5)	0.35	%	Quantexpress (Best Detection)
4.	Silicon Dioxide (SiO2)	0.21	%	Quantexpress (Best Detection)
5.	Aluminium Oxide (Al2O3)	0.17	%	Quantexpress (Best Detection)
6.	Potassium Oxide (K2O)	0.05	%	Quantexpress (Best Detection)
7.	Neobium Oxide (Nb2O5)	0.03	%	Quantexpress (Best Detection)
8.	Zinc Oxide (ZnO)	0.02	%	Quantexpress (Best Detection)
9.	Zirconium Oxide (ZrO2)	0.02	%	Quantexpress (Best Detection)
10.	Sulphur Trioxide (SO3)	0.02	%	Quantexpress (Best Detection)

11.	Calcium Oxide (CaO)	0.01	%	Quantexpress (Best Detection)
12.	Chlorine (Cl)	0.01	%	Quantexpress (Best Detection)
13.	Iron Oxide (Fe2O3)	87	ppm	Quantexpress (Best Detection)

Sample 5: 20wt %

No	Parameter	Results	Unit	Test Method
1.	Titanium Oxide (TiO2)	70.23	%	Quantexpress (Best Detection)
2.	Copper Oxide (CuO)	22.88	%	Quantexpress (Best Detection)
3.	Phosphorus Pentoxide (P2O5)	0.31	%	Quantexpress (Best Detection)
4.	Silicon Dioxide (SiO2)	0.20	%	Quantexpress (Best Detection)
5.	Aluminium Oxide (Al2O3)	0.17	%	Quantexpress (Best Detection)
6.	Potassium Oxide (K2O)	0.04	%	Quantexpress (Best Detection)
7.	Neobium Oxide (Nb2O5)	0.03	%	Quantexpress (Best Detection)
8.	Chlorine (Cl)	0.02	%	Quantexpress (Best Detection)
9.	Sulphur Trioxide (SO3)	0.02	%	Quantexpress (Best Detection)
10.	Zirconium Oxide (ZrO2)	0.01	%	Quantexpress (Best Detection)
11.	Iron Oxide (Fe2O3)	88	ppm	Quantexpress (Best Detection)
12.	Nickel Oxide (NiO)	60	ppm	Quantexpress (Best Detection)
13.	Calcium Oxide (CaO)	55	ppm	Quantexpress (Best Detection)

Sample 6: 25wt %

No	Parameter	Results	Unit	Test Method
1.	Titanium Oxide (TiO2)	62.86	%	Quantexpress (Best Detection)
2.	Copper Oxide (CuO)	27.77	%	Quantexpress (Best Detection)
3.	Phosphorus Pentoxide (P2O5)	0.27	%	Quantexpress (Best Detection)

4.	Silicon Dioxide (SiO2)	0.15	%	Quantexpress (Best Detection)
5.	Aluminium Oxide (Al2O3)	0.14	%	Quantexpress (Best Detection)
6.	Potassium Oxide (K2O)	0.04	%	Quantexpress (Best Detection)
7.	Iron Oxide (Fe2O3)	0.03	%	Quantexpress (Best Detection)
8.	Neobium Oxide (Nb2O5)	0.02	%	Quantexpress (Best Detection)
9.	Sulphur Trioxide (SO3)	0.02	%	Quantexpress (Best Detection)
10.	Calcium Oxide (CaO)	0.02	%	Quantexpress (Best Detection)
11.	Chlorine (Cl)	0.01	%	Quantexpress (Best Detection)
12.	Zirconium Oxide (ZrO2)	0.01	%	Quantexpress (Best Detection)
13.	Chromium Oxide (Cr2O3)	0.01	%	Quantexpress (Best Detection)
14.	Nickel Oxide (NiO)	80	ppm	Quantexpress (Best Detection)

The above analysis is based on the sample submitted by the customer.

.....

SYAHIDAH ALWI
LAB ANALYST
MATERIAL DEPARTMENT
CENTRAL LABORATORY

X-ray Diffraction (XRD)

XRD: 2 wt% Cu/TiO_2

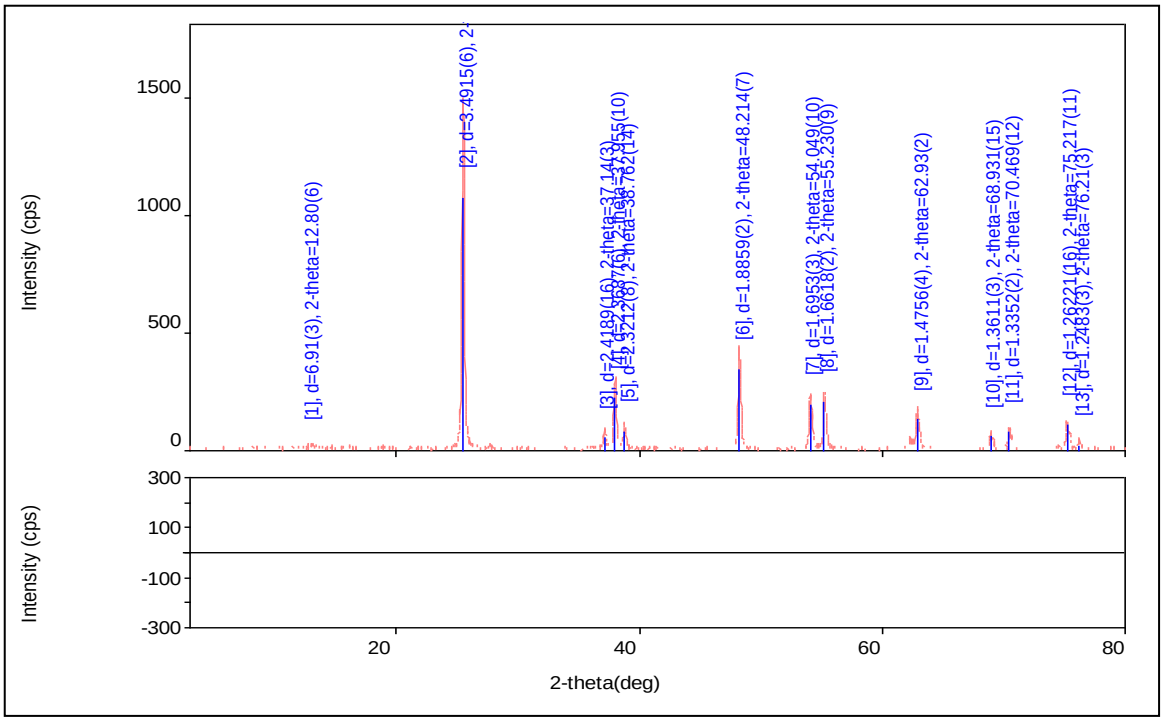

XRD: 5 wt% Cu/TiO_2

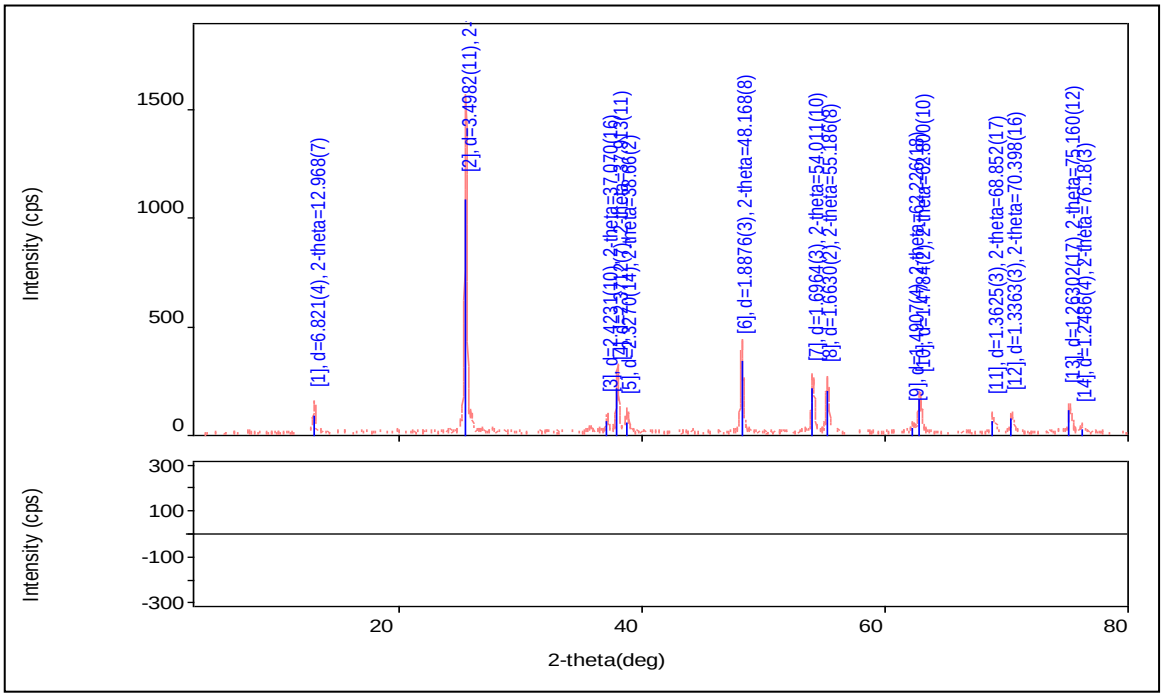

XRD: 10 wt% Cu/TiO_2

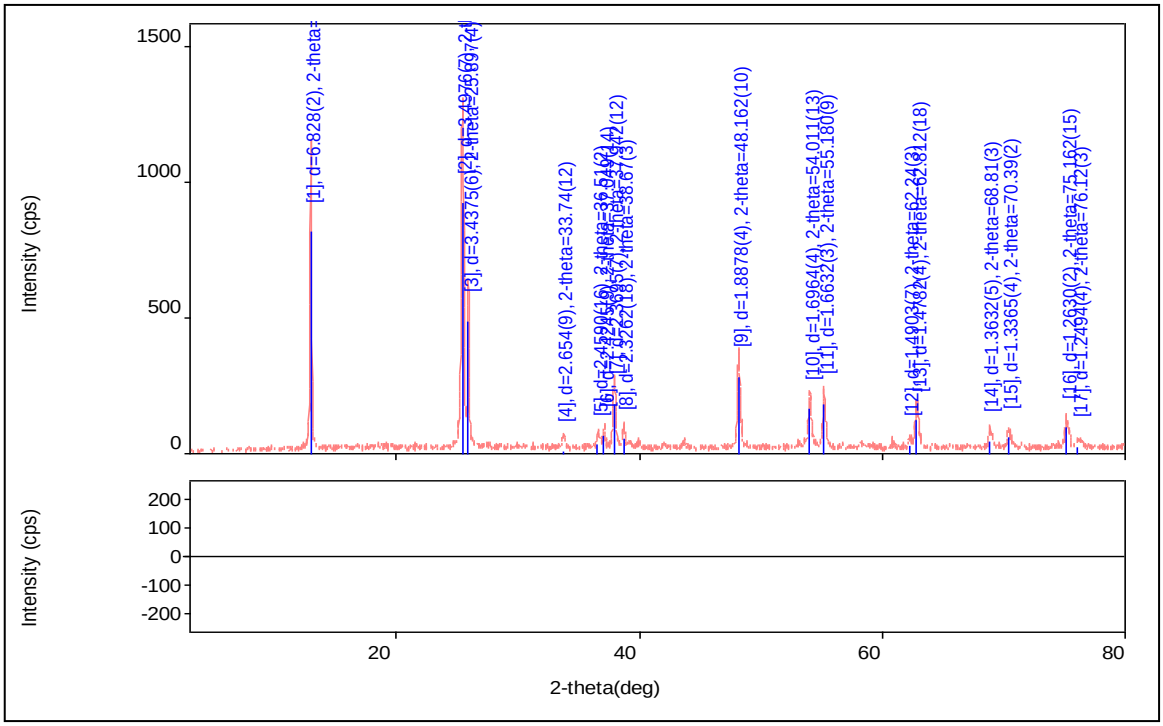

XRD: 15 wt% Cu/TiO_2

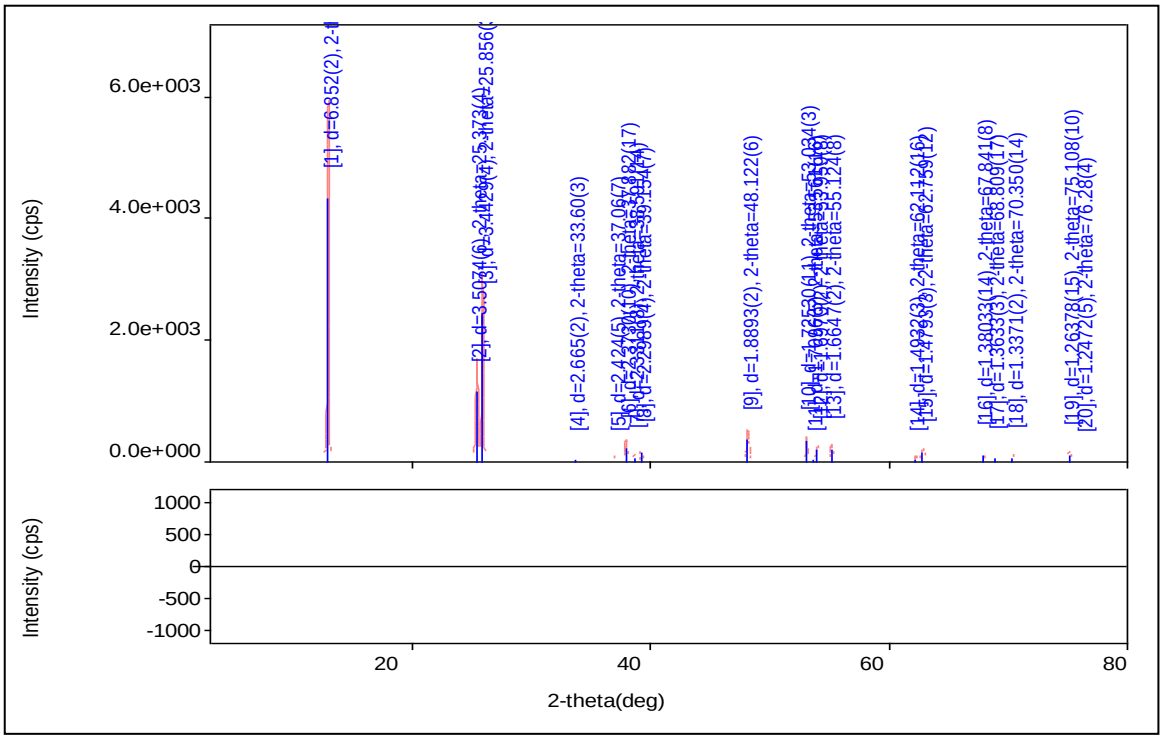

XRD: 20 wt% Cu/TiO_2

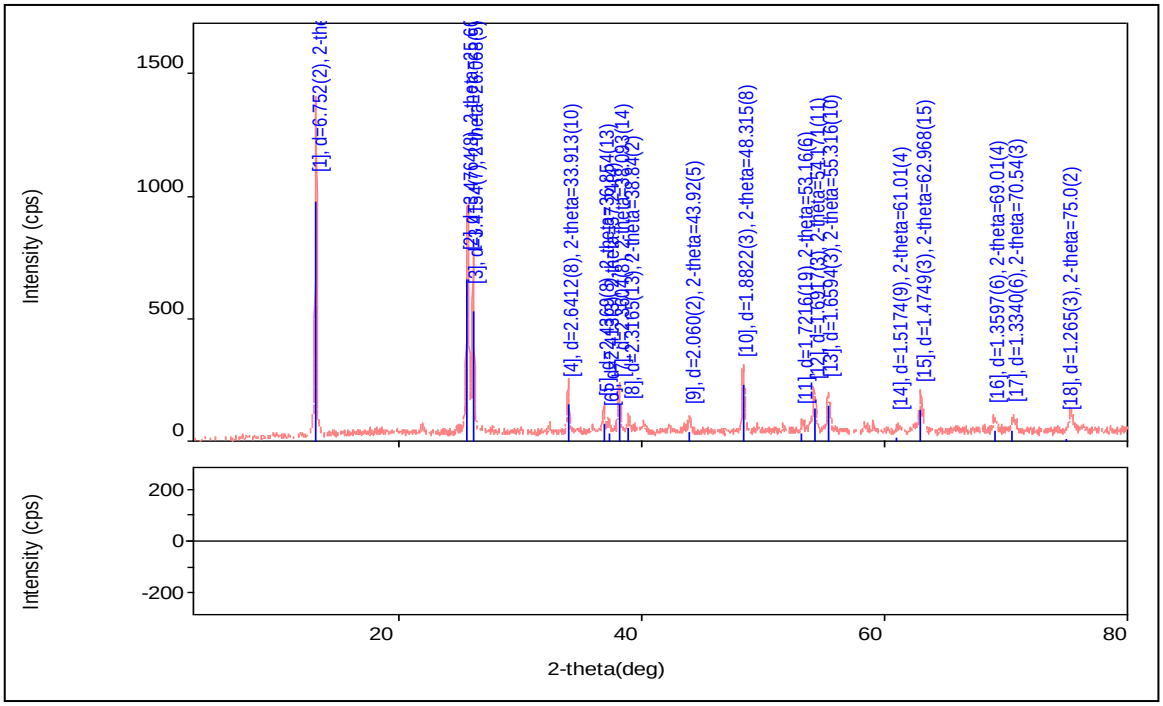

XRD: 25 wt% Cu/TiO_2

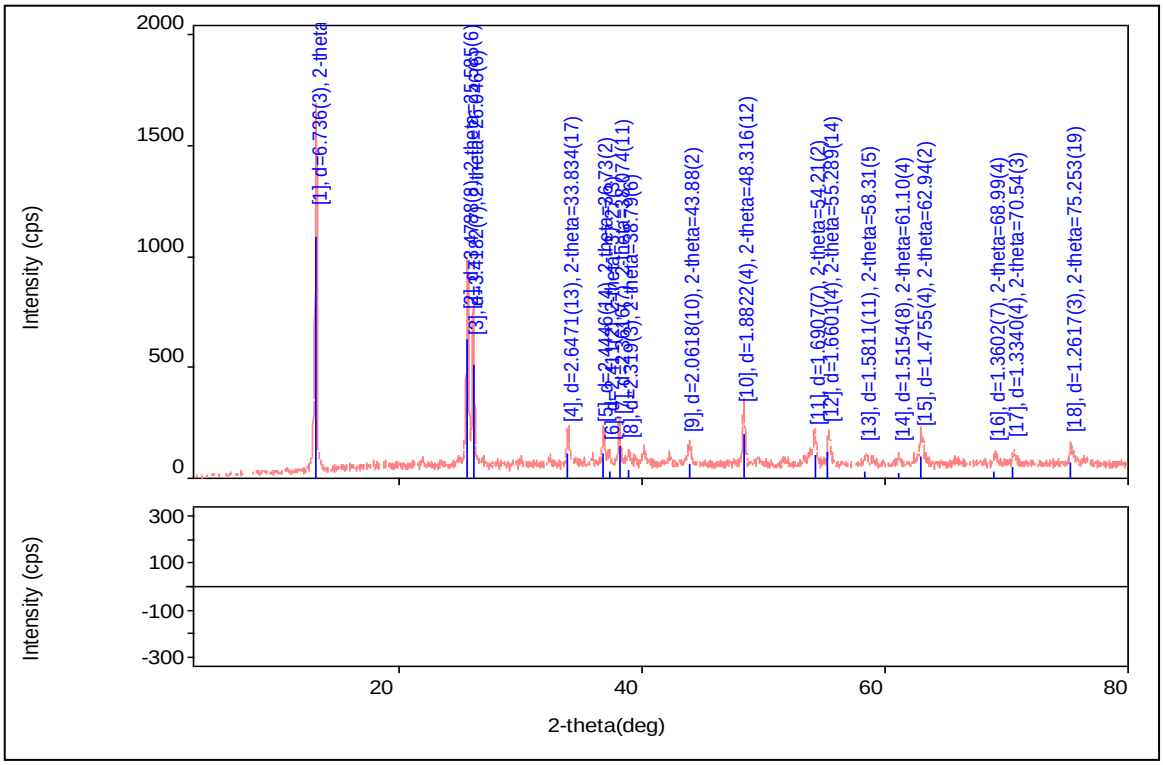

Liquid N_2 Physisorption (BET)

BET : 2 wt% Cu/TiO_2

```
      File:    C:\2020\DATA\000-538.SMP

          Started:    9/17/2013 8:23:17AM       Analysis Adsorptive:    N2
        Completed:    9/17/2013 11:54:42AM      Analysis Bath Temp.:    -195.846 癈
      Report Time:    10/2/2013 10:58:58AM       Thermal Correction:    No
      Sample Mass:    0.2865 g                      Warm Free Space:    28.1666 cm?Measured
  Cold Free Space:    84.8257 cm?           Equilibration Interval:    5 s
Low Pressure Dose:    None                         Automatic Degas:    Yes



Summary Report

                          Surface Area

Single point surface area at P/Po = 0.300213493:    11.1192 m?g

                               BET Surface Area:    11.4195 m?g

                          Langmuir Surface Area:    18.3229 m?g

                          t-Plot Micropore Area:    0.0176 m?g

                  t-Plot External Surface Area:    11.4019 m?g

BJH Adsorption cumulative surface area of pores
       between 17.000 ?and 3000.000 ?diameter:    11.505 m?g

BJH Desorption cumulative surface area of pores
       between 17.000 ?and 3000.000 ?diameter:    11.5080 m?g


                             Pore Volume

 Single point adsorption total pore volume of pores
less than 1277.952 ?diameter at P/Po = 0.984617196:    0.030971 cm?g

 Single point desorption total pore volume of pores
 less than 832.371 ?diameter at P/Po = 0.976178183:    0.035258 cm?g

                          t-Plot micropore volume:    -0.000087 cm?g

          BJH Adsorption cumulative volume of pores
           between 17.000 ?and 3000.000 ?diameter:    0.040005 cm?g

          BJH Desorption cumulative volume of pores
           between 17.000 ?and 3000.000 ?diameter:    0.039855 cm?g
```

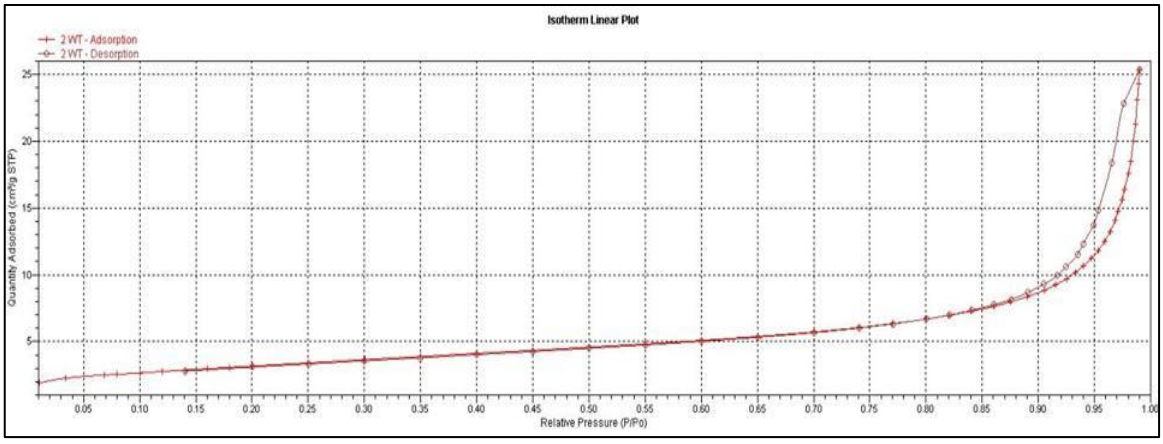

BET : 5 wt% Cu/TiO_2

File: C:\2020\DATA\000-539.SMP

Started:	9/17/2013 12:03:51PM	Analysis Adsorptive:	N2
Completed:	9/17/2013 4:03:35PM	Analysis Bath Temp.:	-195.881 癈
Report Time:	10/2/2013 10:58:59AM	Thermal Correction:	No
Sample Mass:	0.4063 g	Warm Free Space:	27.9343 cm?Measured
Cold Free Space:	84.4128 cm?	Equilibration Interval:	5 s
Low Pressure Dose:	None	Automatic Degas:	Yes

Summary Report

Surface Area

Single point surface area at P/Po = 0.300423352:	9.9969 m?g
BET Surface Area:	10.2263 m?g
Langmuir Surface Area:	16.2439 m?g
t-Plot Micropore Area:	0.6832 m?g
t-Plot External Surface Area:	9.5431 m?g
BJH Adsorption cumulative surface area of pores between 17.000 ?and 3000.000 ?diameter:	9.486 m?g
BJH Desorption cumulative surface area of pores between 17.000 ?and 3000.000 ?diameter:	10.0041 m?g

Pore Volume

Single point adsorption total pore volume of pores less than 1359.291 ?diameter at P/Po = 0.985553513:	0.033312 cm?g
Single point desorption total pore volume of pores less than 1088.591 ?diameter at P/Po = 0.981886893:	0.044166 cm?g
t-Plot micropore volume:	0.000310 cm?g
BJH Adsorption cumulative volume of pores between 17.000 ?and 3000.000 ?diameter:	0.049071 cm?g
BJH Desorption cumulative volume of pores between 17.000 ?and 3000.000 ?diameter:	0.049593 cm?g

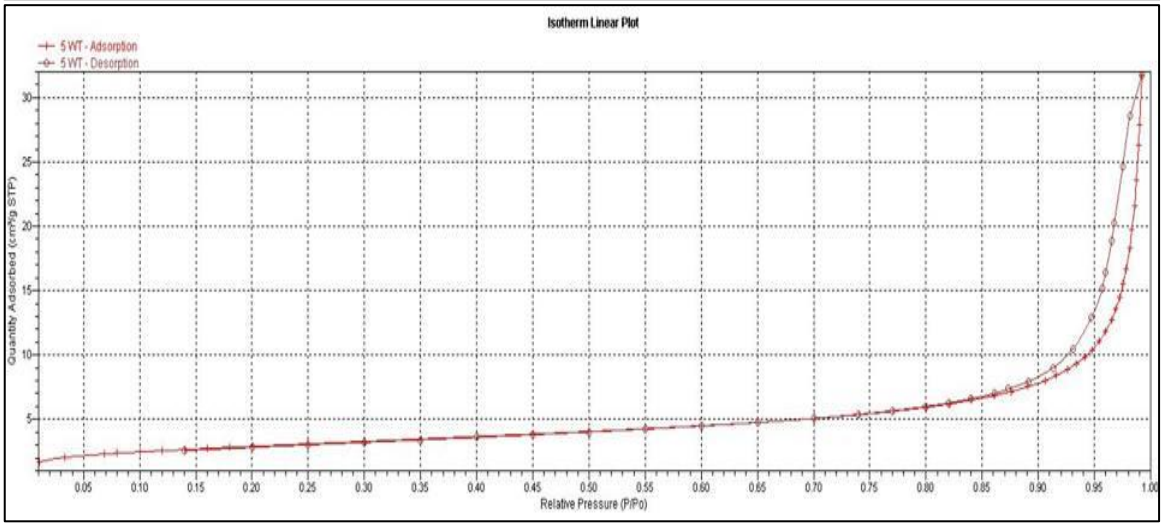

BET : 10 wt% Cu/TiO_2

```
      File:    C:\2020\DATA\000-540.SMP

          Started:    9/17/2013 4:15:46PM        Analysis Adsorptive:    N2
        Completed:    9/17/2013 8:00:20PM        Analysis Bath Temp.:    -195.887 ?
      Report Time:    10/2/2013 10:59:00AM        Thermal Correction:    No
      Sample Mass:    0.3014 g                       Warm Free Space:    27.4472 cm?Measured
  Cold Free Space:    82.1303 cm?             Equilibration Interval:    5 s
Low Pressure Dose:    None                           Automatic Degas:    Yes



Summary Report

                          Surface Area

Single point surface area at P/Po = 0.300218685:    9.8304 m?g

                               BET Surface Area:    9.9834 m?g

                          Langmuir Surface Area:    15.6981 m?g

                          t-Plot Micropore Area:    1.4277 m?g

                  t-Plot External Surface Area:    8.5557 m?g

BJH Adsorption cumulative surface area of pores
       between 17.000 ?and 3000.000 ?diameter:    8.550 m?g

BJH Desorption cumulative surface area of pores
       between 17.000 ?and 3000.000 ?diameter:    9.8064 m?g


                           Pore Volume

 Single point adsorption total pore volume of pores
less than 1203.227 ?diameter at P/Po = 0.983643846:    0.032267 cm?g

 Single point desorption total pore volume of pores
less than 822.714 ?diameter at P/Po = 0.975892260:    0.038329 cm?g

                          t-Plot micropore volume:    0.000719 cm?g

          BJH Adsorption cumulative volume of pores
           between 17.000 ?and 3000.000 ?diameter:    0.042037 cm?g

          BJH Desorption cumulative volume of pores
           between 17.000 ?and 3000.000 ?diameter:    0.042894 cm?g
```

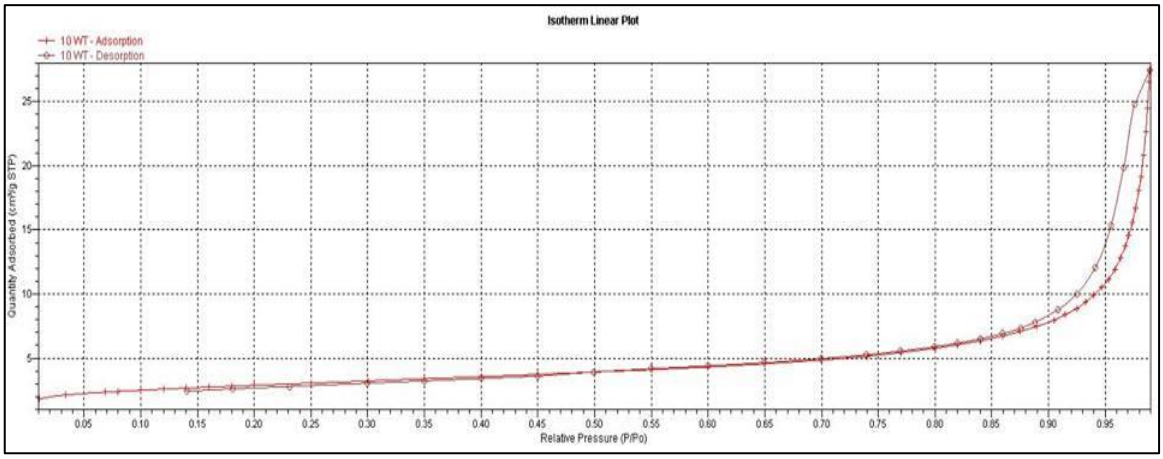

BET : 15 wt% Cu/TiO_2

```
      File:    C:\2020\DATA\000-541.SMP

          Started:    9/18/2013 8:30:48AM       Analysis Adsorptive:    N2
        Completed:    9/18/2013 12:40:23PM      Analysis Bath Temp.:    -195.860 癈
      Report Time:    10/2/2013 10:59:02AM       Thermal Correction:    No
      Sample Mass:    0.3944 g                      Warm Free Space:    27.1891 cm?Measured
  Cold Free Space:    81.9268 cm?           Equilibration Interval:    5 s
Low Pressure Dose:    None                         Automatic Degas:    Yes



Summary Report

                          Surface Area

Single point surface area at P/Po = 0.300359587:    8.9474 m?g

                              BET Surface Area:    9.1699 m?g

                          Langmuir Surface Area:   14.6168 m?g

                          t-Plot Micropore Area:   0.4122 m?g

                  t-Plot External Surface Area:    8.7577 m?g

BJH Adsorption cumulative surface area of pores
       between 17.000 ?and 3000.000 ?diameter:    9.166 m?g

BJH Desorption cumulative surface area of pores
       between 17.000 ?and 3000.000 ?diameter:    9.2837 m?g


                          Pore Volume

 Single point adsorption total pore volume of pores
less than 1328.824 ?diameter at P/Po = 0.985216398:    0.029548 cm?g

 Single point desorption total pore volume of pores
 less than 910.128 ?diameter at P/Po = 0.978255755:    0.037015 cm?g

                          t-Plot micropore volume:     0.000162 cm?g

          BJH Adsorption cumulative volume of pores
           between 17.000 ?and 3000.000 ?diameter:    0.041079 cm?g

          BJH Desorption cumulative volume of pores
           between 17.000 ?and 3000.000 ?diameter:    0.040976 cm?g
```

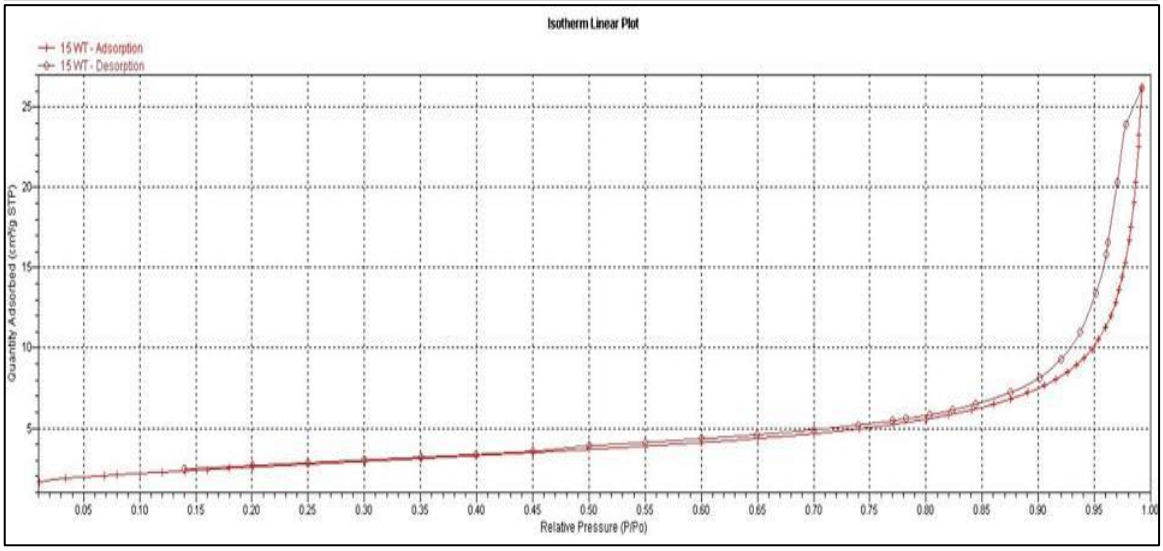

BET : 20 wt% Cu/TiO_2

```
      File:    C:\2020\DATA\000-542.SMP

          Started:    9/18/2013 4:22:32PM        Analysis Adsorptive:    N2
        Completed:    9/18/2013 9:04:29PM        Analysis Bath Temp.:    -195.889 ?
      Report Time:    10/2/2013 10:59:03AM        Thermal Correction:    No
      Sample Mass:    0.5808 g                       Warm Free Space:    27.6163 cm?Measured
  Cold Free Space:    82.6957 cm?             Equilibration Interval:    5 s
Low Pressure Dose:    None                           Automatic Degas:    Yes



Summary Report

                          Surface Area

 Single point surface area at P/Po = 0.300273675:    7.4365 m?g

                              BET Surface Area:    7.4933 m?g

                          Langmuir Surface Area:    11.6530 m?g

                          t-Plot Micropore Area:    1.8032 m?g

                  t-Plot External Surface Area:    5.6901 m?g

 BJH Adsorption cumulative surface area of pores
       between 17.000 ?and 3000.000 ?diameter:    6.611 m?g

 BJH Desorption cumulative surface area of pores
       between 17.000 ?and 3000.000 ?diameter:    7.9384 m?g


                           Pore Volume

  Single point adsorption total pore volume of pores
 less than 1244.384 ?diameter at P/Po = 0.984194604:    0.029929 cm?g

  Single point desorption total pore volume of pores
  less than 881.368 ?diameter at P/Po = 0.977530715:    0.036251 cm?g

                         t-Plot micropore volume:    0.000927 cm?g

           BJH Adsorption cumulative volume of pores
            between 17.000 ?and 3000.000 ?diameter:    0.038661 cm?g

           BJH Desorption cumulative volume of pores
            between 17.000 ?and 3000.000 ?diameter:    0.039213 cm?g
```

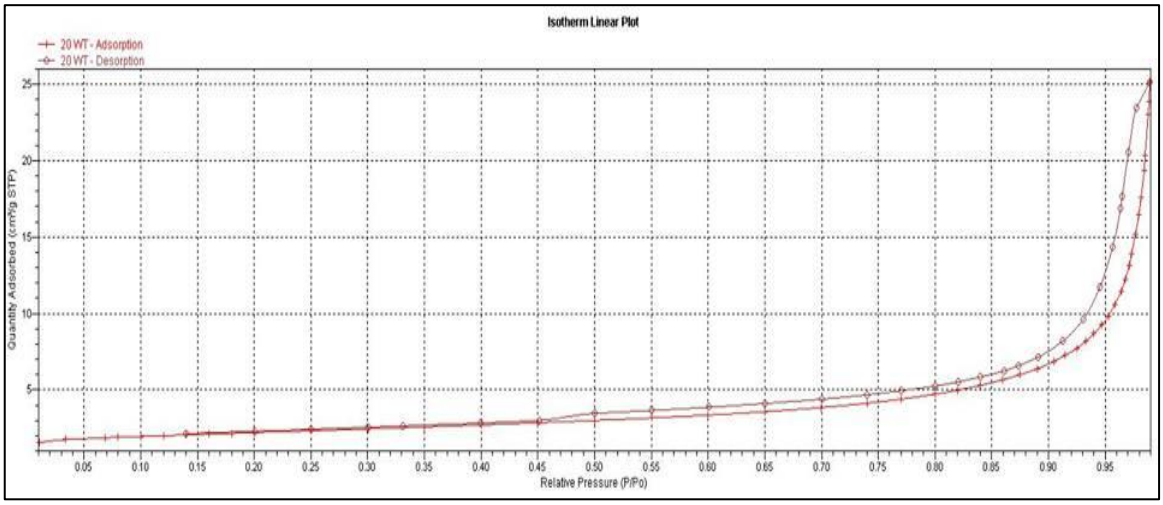

BET : 25 wt% Cu/TiO_2

File: C:\2020\DATA\000-543.SMP

Started:	9/21/2013 1:49:16PM	Analysis Adsorptive:	N2
Completed:	9/21/2013 6:34:09PM	Analysis Bath Temp.:	-195.887 ?
Report Time:	10/2/2013 10:59:04AM	Thermal Correction:	No
Sample Mass:	0.5178 g	Warm Free Space:	26.9389 cm?Measured
Cold Free Space:	76.2218 cm?	Equilibration Interval:	5 s
Low Pressure Dose:	None	Automatic Degas:	Yes

Summary Report

Surface Area

Single point surface area at P/Po = 0.300239258:	6.2407 m?g
BET Surface Area:	6.2037 m?g
Langmuir Surface Area:	9.5231 m?g
t-Plot Micropore Area:	2.4950 m?g
t-Plot External Surface Area:	3.7088 m?g
BJH Adsorption cumulative surface area of pores between 17.000 ?and 3000.000 ?diameter:	6.273 m?g
BJH Desorption cumulative surface area of pores between 17.000 ?and 3000.000 ?diameter:	10.6872 m?g

Pore Volume

Single point adsorption total pore volume of pores less than 1275.730 ?diameter at P/Po = 0.984589921:	0.029647 cm?g
Single point desorption total pore volume of pores less than 843.658 ?diameter at P/Po = 0.976503907:	0.034104 cm?g
t-Plot micropore volume:	0.001265 cm?g
BJH Adsorption cumulative volume of pores between 17.000 ?and 3000.000 ?diameter:	0.036669 cm?g
BJH Desorption cumulative volume of pores between 17.000 ?and 3000.000 ?diameter:	0.036841 cm?g

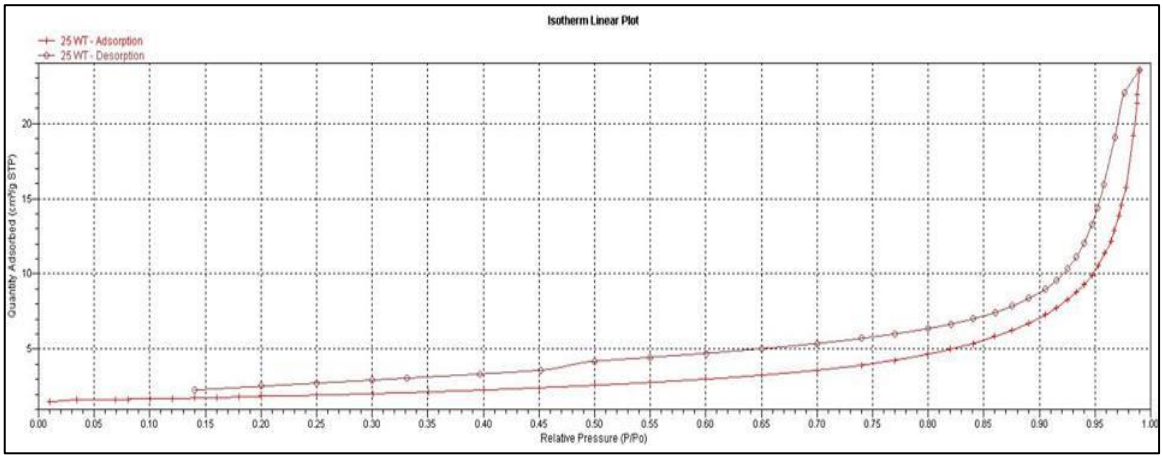

Thermogravimetric Analysis (TGA)

TGA: 2 wt% Cu/TiO_2

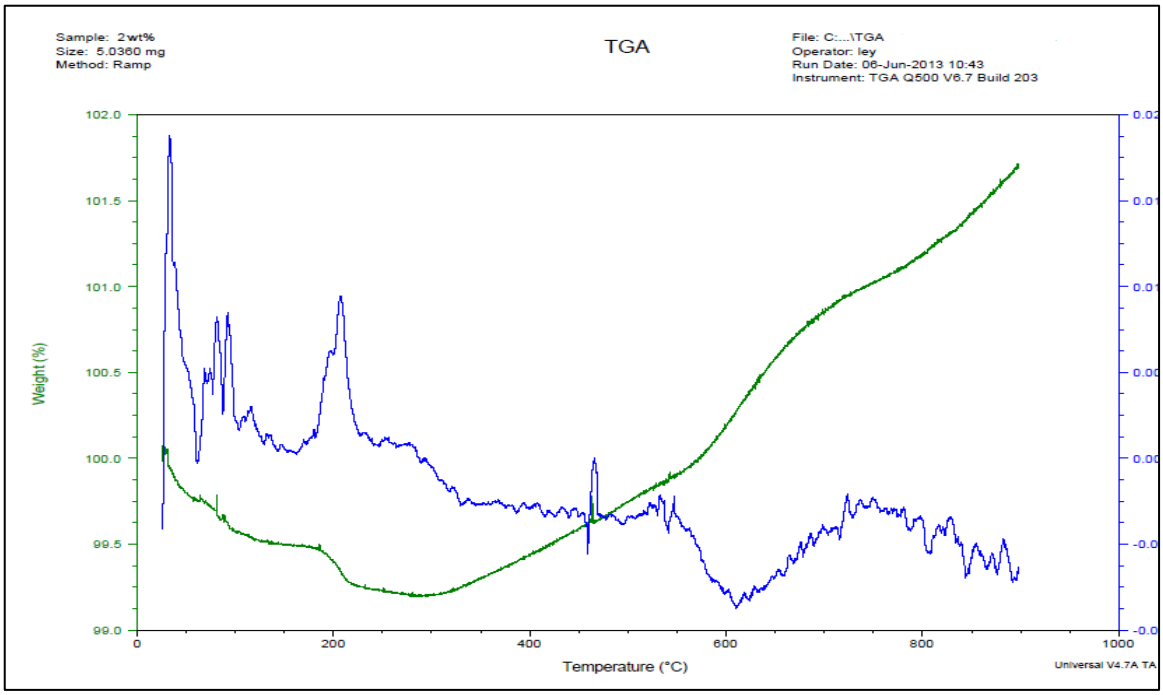

TGA: 5 wt% Cu/TiO_2

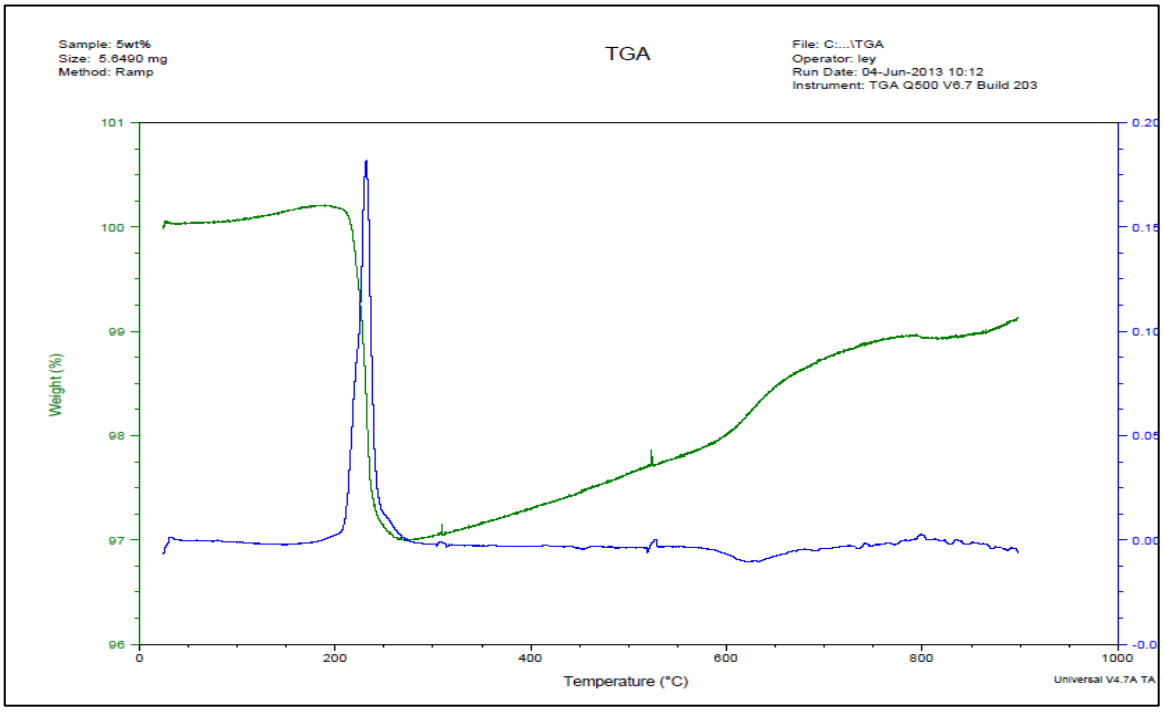

TGA: 10 wt% Cu/TiO_2

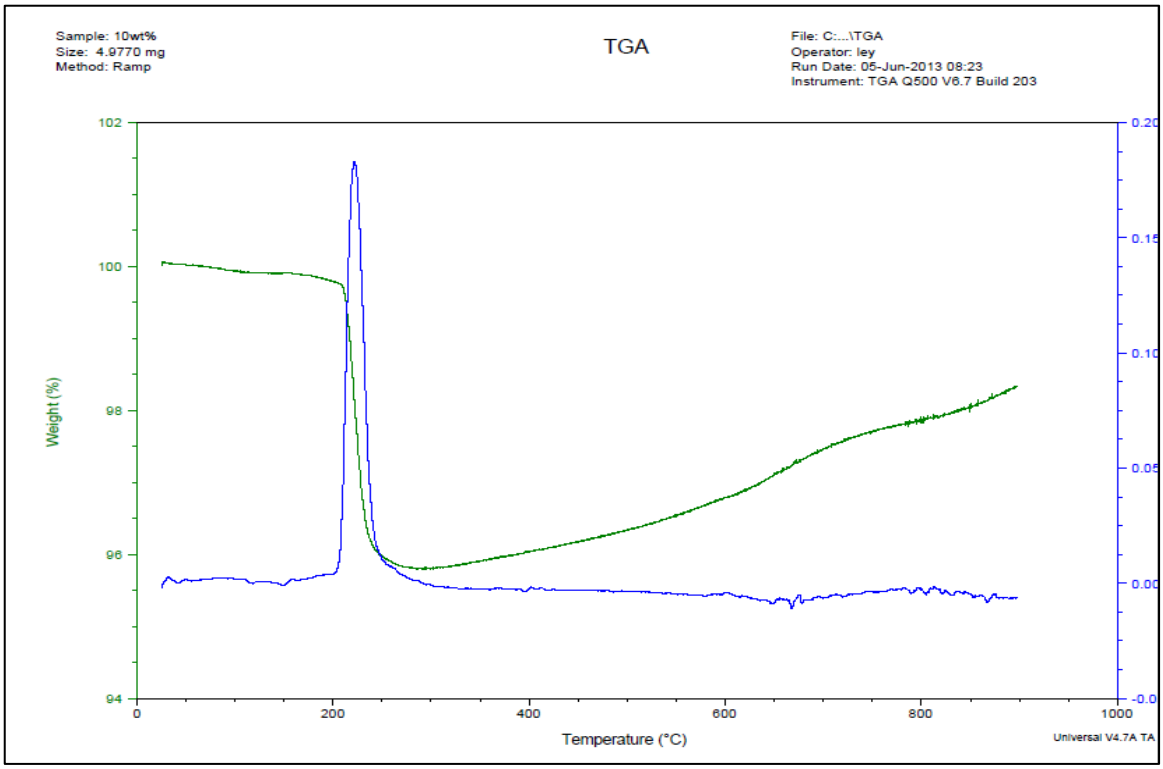

TGA: 15 wt% Cu/TiO_2

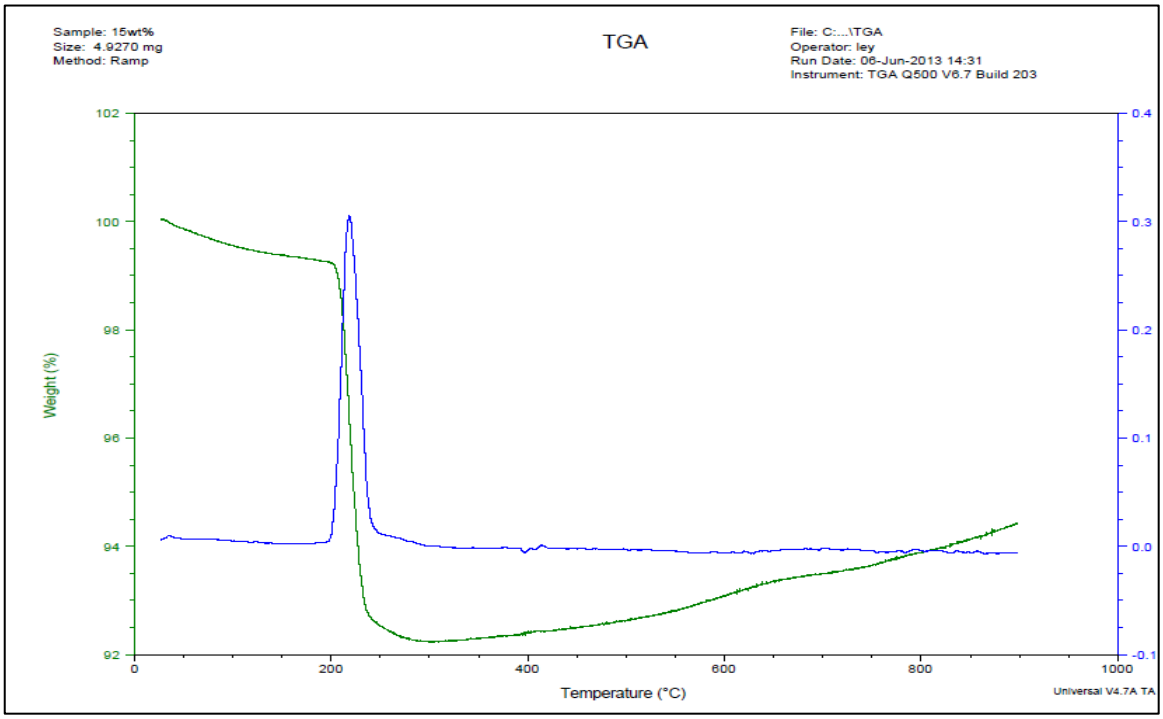

TGA: 20 wt% Cu/TiO_2

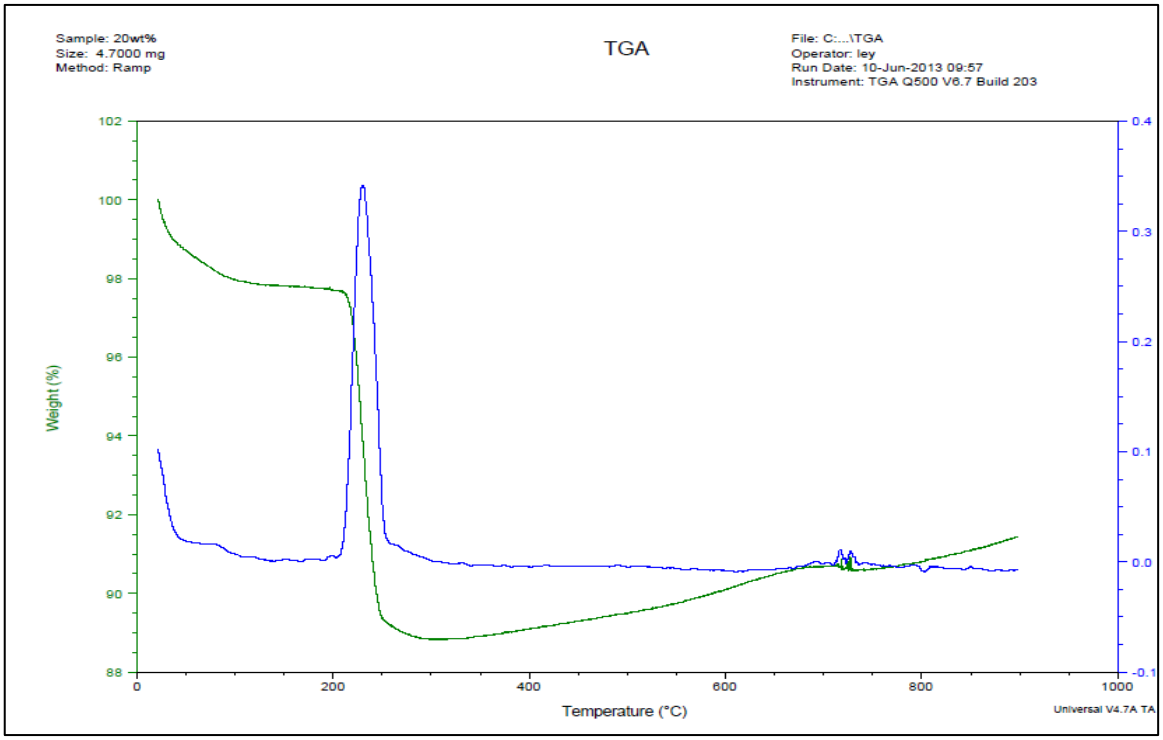

TGA: 25 wt% Cu/TiO_2